Effects of branching on conformation, crystallization, and self-assembly of polymers

Thesis by

Joey D. Kim

In Partial Fulfillment of the Requirements for

the degree of

Doctor of Philosophy

CALIFORNIA INSTITUTE OF TECHNOLOGY

Pasadena, California

2019

(Defended April 10, 2019)

Joey D. Kim
ORCID: 0000-0002-3359-4875

ACKNOWLEDGEMENTS

I would like to thank Jesus Christ, my Savior and Lord.

ABSTRACT

The central feature of bottlebrush polymers is the stiffening of the main-chain (MC) due to side-chain side-chain (SC-SC) repulsion, amplified by densely grafting long SCs, particularly in good solvent conditions. The expectation of stiffening has led most prior studies to refer to bottlebrush polymers as "worm-like," "cylindrical" or a "self-avoiding walk (SAW) of superblobs". However, there is no direct evidence of stiffening of the main-chain and measurements of the overall segment distribution of the whole molecule have failed to discriminate between competing models. Here, we provide a set of measurements of the main-chain conformation (neutron scattering in a solvent that is contrast matched to the side chains) together with the overall conformation of the bottlebrush as a whole (light, X-ray, and neutron scattering) under conditions that highlight SC-SC repulsion: the side-chains are relatively long compared to prior literature, the concentration of bottlebrushes is low, and the solvent quality is good. Surprisingly, the main-chain has a conformation that does not conform to any prior models: all three main-chain lengths examined showed a window of length scales in which the scattering power increased less than linearly with length scale. In particular, the MC conformation is not worm-like. Direct observation of the main-chain conformation and the overall conformation discriminates among models more powerfully than the overall conformation alone. Inspired by the Paturej-Rubinstein tension blob model, we examined a conceptual model in which tension of the MC accumulates with distance from the ends of the MC and found that it can capture the salient features of both the MC- and whole bottlebrush scattering more gradually than previous theoretical models predicted. The conceptual model also explains our observation of a substantial increase in anisometry with increasing MC length, opposite to a worm-like chain. The results indicate that synthetically accessible bottlebrushes are not fractals; they cannot have self-similar (fractal) conformation because each increase in main-chain length accesses greater side-chain crowding than any of its shorter siblings. We expanded the work to understand the behavior in θ conditions and shorter side-chains expected to have reduced tension as well as the behavior at different concentrations.

In addition, we characterized the interplay of self-assembly and polymer crystallization through analysis of three representative bottlebrush copolymer systems. Our results revealed a surprising number of unexpected behaviors ranging from unexpected morphologies, control of thermal properties even to complete suppression of phase transitions, and control of the orientation of crystal stem with respect to the morphological interface, which highlights the potential of the bottlebrush architecture.

TABLE OF CONTENTS

LIST OF FIGURES

LIST OF TABLES

Chapter 1

BOTTLEBRUSH POLYMERS – AN IDEAL BRANCHED STRUCTURE

1   Introduction

This thesis work focuses on three topics: the effects of branching on conformation (Chapters 2 & 3), self-assembly (Chapter 4), and crystallization (Chapter 4) of polymers (Figure 1.1). But first, why study the effects of branching?
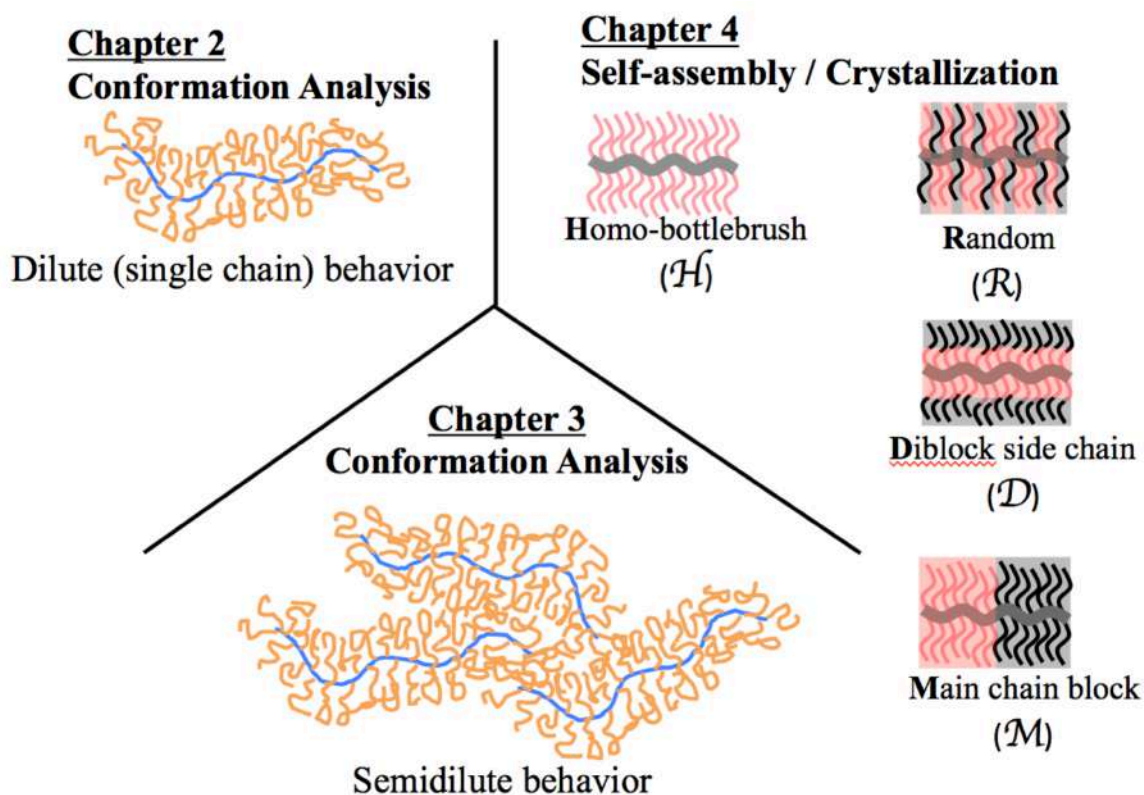
Figure 1.1. Thesis overview. Conformation analysis in dilute conditions are discussed in Chapter 2, conformation analysis in semi-dilute conditions are discussed in Chapter 3, and self-assembly and crystallization behavior of bottlebrush systems are discussed in Chapter 4.

1.1   Why study the effects of branching?

Archaeologists have categorized human history into time periods determined by the material that were prevalently used. Referred to as the Three-Age System of Archaeology[1]

(Figure 1.2A), three times periods were identified: Stone-Age (before 3300 B.C.E), Bronze-Age (3300-1200 B.C.E), and Iron-Age (1200 B.C.E to 500 B.C.E). A molecular look (Figure 1.2B) at these materials reveals a similarity in the size of the smallest building blocks with length scales on order of 0.1-1nm. For Stone-Age (silicon-oxide) is a tetrahedral structure formed by silicon-oxygen bonds of bond length l_{Si-O}=0.162nm. For Bronze-Age (copper-tin alloy) and Iron-Age (iron/steel) is a face-centered cubic and body-centered cubic lattice, respectively, with atomic radii of r_{Cu}=0.128nm, r_{Sn}=0.140nm, and r_{Fe}=0.126nm.
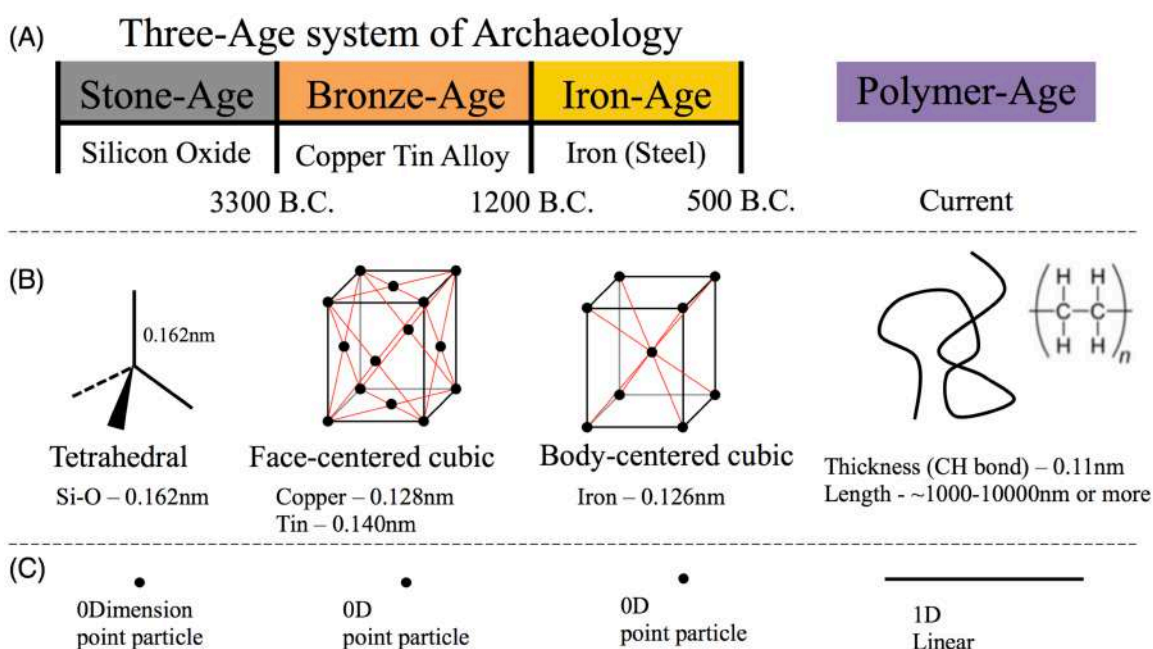
Figure 1.2. Comparing the prevalent materials in history. (A) A summary of the Three-Age system of Archaeology and the Polymer-Age. (B) The molecular building blocks of the corresponding Age of human history. Silicon-oxide represents the Stone-Age, Copper-Tin alloy represents the Bronze-Age, Iron (Steel) represents the Iron-Age, and polyethylene represents the Polymer-Age. (C) The relative size of the molecular building blocks of the Stone-Age, Bronze-Age, and Iron-Age, and Polymer-Age.

By applying the same categorization method, some have dubbed the post WWII period to be the Polymer-Age[2]. With the technological advancements available today, what are the reasons that polymers are chosen over the classical materials? A molecular look at polymers reveals a clear distinction in polymers relative to classical materials in the molecular size. Commonly used polymers can range from 1000-10000nm in length, four to five orders of magnitude larger than the size of classical materials, but in a single axis, as

the thickness (C-H bond) is roughly 0.11nm, which is on similar to the size of the classical materials.

In terms of relative size, the building blocks of classical materials are approximately 0-Dimensional, or point particles, whereas polymers would be approximately 1-Dimensional, or (curvi)linear, molecules (Figure 1.2C). It is the 1-Dimensionality of polymers that make its use so prevalent in the world today. To understand why, we will consider the ways in which materials move on the molecular level.
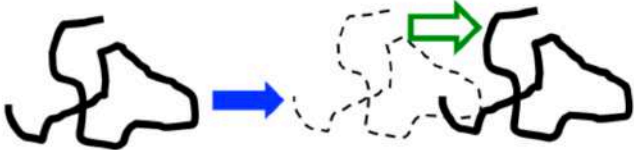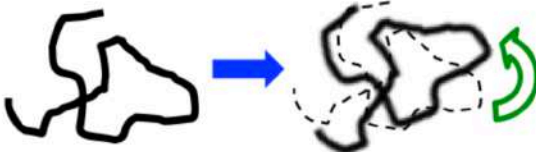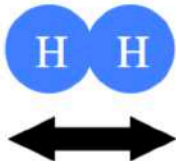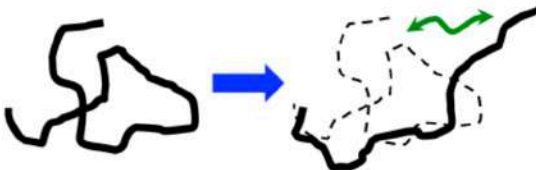
Figure 1.3. Schematic of degrees of freedom of movement. The degrees of freedom of movement of classical materials: translation, rotation, and vibration. Polymers have an additional degree of freedom of chain relaxation.

Classical materials have three degrees of freedom of movement: translation, rotation, and vibration (Figure 1.3). The 1-dimensionality of linear polymers enables an additional type of movement not available to the classical materials – conformation relaxation. This additional freedom enables behavior that cannot be observed in classical materials such as entanglements, creep/history, elasticity, and cross-linking which leads to desirable mechanical properties such as flexibility and high strength to weight ratio; some reasons for it being the choice material today, as opposed to the classical materials. Therefore, we see that as the dimensionality of the molecular units increased from 0D to 1D, significant advantages were obtained.
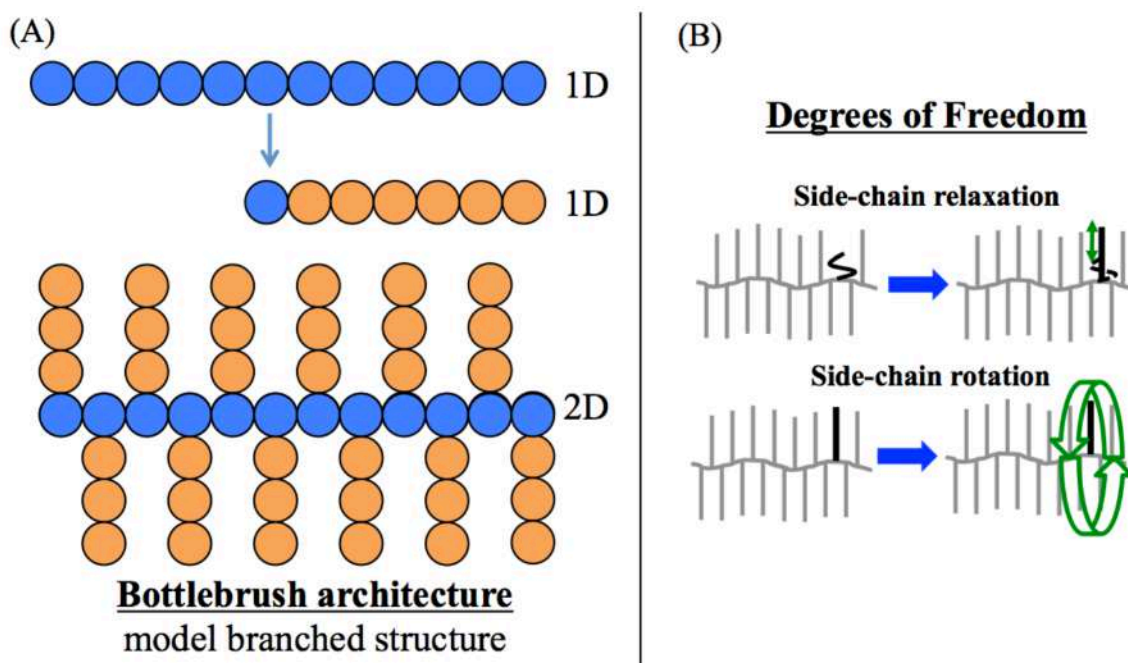
Figure 1.4. Bottlebrush polymers – a model branched structure. (A) Schematic representation a 2D structure achieved through branching – polymers branched from a polymer. The 2D structure is referred to as the bottlebrush architecture. (B) The degrees of freedom accessible to bottlebrush systems that are not accessible by classical materials nor 1D materials: side-chain relaxation and side-chain rotation.

But why stop at 1D? Can benefits of similar magnitude be obtained through increasing the dimensionality from 1D to 2D? This is where the effects of branching can be showcased. Polymers are made up of many units named monomers. If each monomer was itself a 1D polymer, the resulting structure a densely and periodically branched polymer (Figure 1.4A). By introducing branching into polymers, the second dimension can

be accessed in a system referred to as a bottlebrush architecture. Bottlebrush systems are a model branched structure with regularly spaced branching referred to as side-chains (in orange) from a primary main-chain (in blue). Therefore, understanding the interplay of individual polymeric units that make up the bottlebrush architecture reveals the effects of branching on various properties of polymers such as conformation, crystallization, and self-assembly.

The bottlebrush system has two additional degrees of freedom: side-chain rotation and side-chain relaxation (Figure 1.4B). In total, that is five degrees of freedom of movement: translation, rotation, (main-)chain relaxation, side-chain relaxation, and side-chain rotation. In contrast to 0D-1D transition, where only a single degree of freedom was introduced, two additional degrees of freedom are gained from the 1D-2D transition from linear to bottlebrush polymers, giving a positive outlook on the potential benefits that can be obtained with the 2D bottlebrush system.

1.2   Bottlebrush polymers – a model branched structure

Bottlebrush polymers are unique class of polymers consisting of many polymeric units hierarchically arranged into side-chains densely grafted to a main-chain. Neighboring side-chains (SC) repel each other, stretching the backbone along its contour. The degree of SC-SC repulsion can be controlled by architectural parameters, mainly graft spacing and SC length, in addition to the inherent chemical properties of the constituent polymers, *e.g.*, chain flexibility and polymer functional groups. The array of tunable parameters allows bottlebrushes to expand the envelope of accessible properties. Recently, bottlebrushes have been used in applications for super-soft elastomers[3,4], drug delivery[5], self-assembling materials[6–8], protective layers[9], photonics[10], lubricants[11], emulsifiers[12], and energy storage[13]. In addition, the regular spacing of side-chains in bottlebrushes provides a model architecture for studying the effects of branching relevant to biological functions rooted in branched architecture, *e.g.*, mucin[14], in which dense branching leads to formation of a regulatory layer, and aggrecans[15]; in which dense branching is essential to joint lubrication.

With many polymeric units interacting within a single bottlebrush, it is important to understand some basic concepts of linear polymers. We will discuss the polymer physics

concepts essential for understanding bottlebrush behavior – solvent quality, concentration regimes, and brush condition. A more rigorous overview of polymer physics can be found in the Appendix.

1.3 Crash course on linear polymers

1.3.1 *Solvent quality - not all random walks are the same*

Polymers are made of repeat unit known as monomers. In an ideal case, where we assume each monomer is a point particle with bond length, *b*, each monomer can be positioned at any point *b* distance from the prior monomer. With this statistic, the root-mean-square end-to-end distance is $<R_{ee}^2>^{1/2} \sim N^{1/2}$. This is known as a Gaussian chain. However, in reality, each monomer is not a point particle, but has volume. Therefore, in a solution, the polymer chains have a topological constraint, which prevents overlap/crossover of the chain. Instead of a random walk with ideal chain statistics, a self-avoiding walk (SAW) with scaling relationship $<R_{ee}^2>^{1/2} \sim N^{3/5}$ is observed. The solvents in which the polymers adopt a SAW are referred to as 'good solvents'. However, in a certain solvent condition, monomer-monomer interactions become increasing favorable such that the ideal chain statistics can be recovered. This solvent is referred to as the θ solvent.

Scattering experiments play a vital role in understanding the conformation of polymer systems as the internal structure is directly measured (Figure 1.5). Below the dotted line is the scattering profile of the internal structure and is unique for each selected system: collapsed structure, Gaussian/RW, SAW, and rod-like where the scattering slope is inversely related to the scaling exponent. Scattering results are vital in our findings of bottlebrush conformation discussed in Chapters 2 and 3.

	Collapsed (-)	Gaussian (θ)	SAW (+)	Rod
Schematic				
Scaling behavior	$R \sim N^{1/3}$	$R \sim N^{1/2}$	$R \sim N^{3/5}$	$R \sim N^{1}$
Scattering slope	$\lvert m \rvert = 3$	$\lvert m \rvert = 2$	$\lvert m \rvert = 5/3$	$\lvert m \rvert = 1$
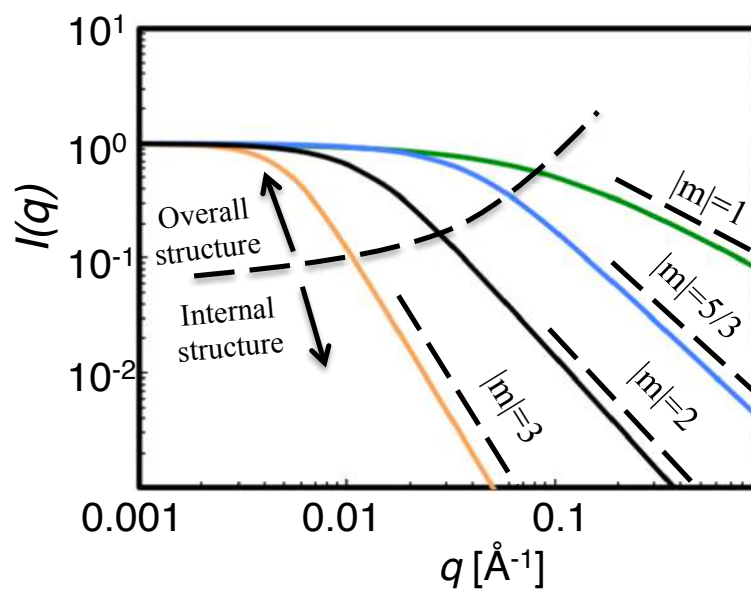
Figure 1.5. Limiting cases for linear behavior. A summary of some limiting cases for linear systems including collapsed, Gaussian, SAW, and rods. A hypothetical scattering profile for each limiting case is shown.

1.3.2 Semidilute regime and brush condition

The scattering patterns for the systems in Figure 1.5 are only valid for dilute conditions, in which the single chain behavior is considered without obstruction from intermolecular interactions. As the concentration is increased through increasing the number of chains in solution, the chains begin to overlap (Figure 1.6A-C), leading to intermolecular interactions causing deviating behavior from dilute conditions.
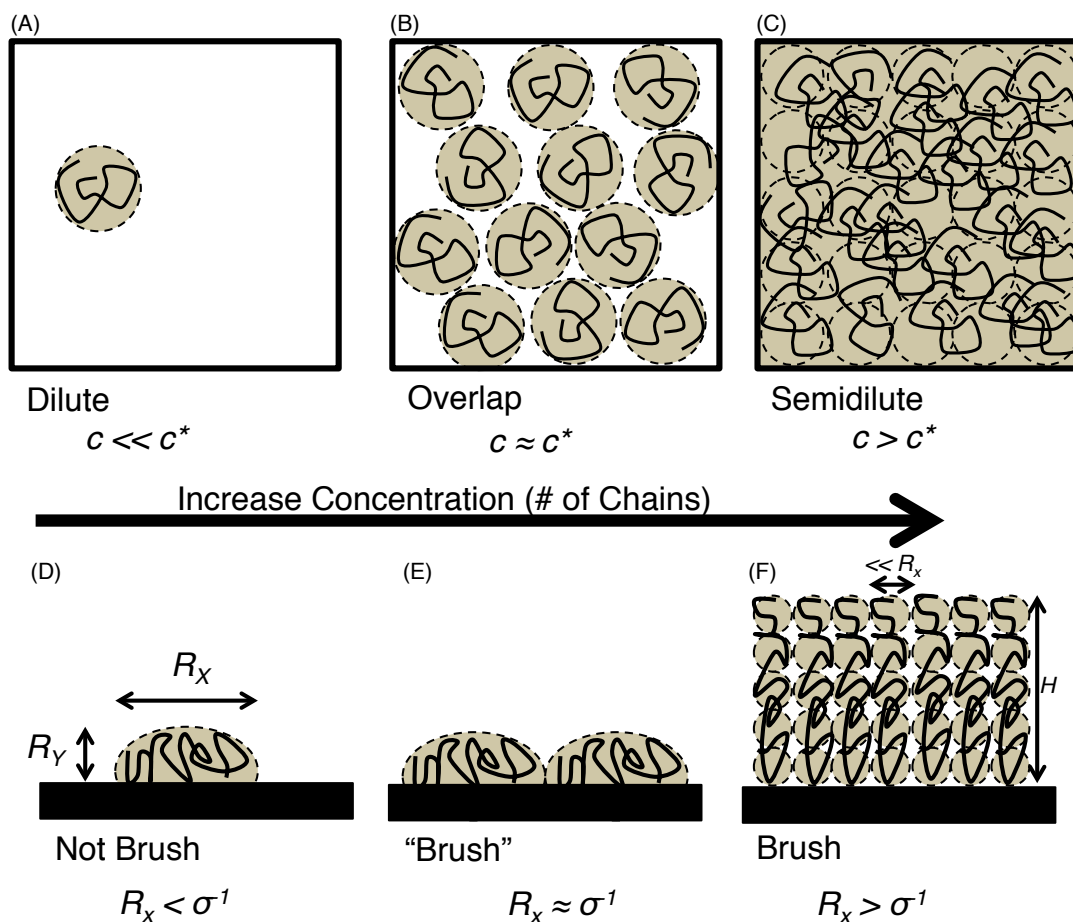
Figure 1.6. Concentration regimes and the brush condition. (A)-(C) shows the progression in increasing polymer concentration in solution with (A) representing dilute conditions, (B) representing polymers near the overlap concentration, and (C) representing semidilute conditions with chains overlapping. (D)-(F) shows the progression in increasing polymer concentration by increasing grafting density of polymers grafted onto a surface. (D) shows a lone polymer grafted with dimensions R_x and R_y, (E) shows the onset of a brush condition in which polymers are grafted at an average distance of R_x apart, and (F) shows the brush condition in which the dense grafting forces the height to extend to lengths greater than R_y.

A specific scenario to discuss is for a polymer grafted onto a surface (Figure 1.6D-F). Let us consider a polymer which, when grafted onto a surface, naturally forms a height of R_y and width R_x. As the concentration is increased by grafting polymers closer together, eventually, the polymers will be grafted at distances shorter than R_x, causing polymer chains to overlap (Figure 1.6F). The net result is lateral repulsion from neighboring chains and the polymer chain can no longer form a width of R_x along the direction of the plane. Instead, the polymer chain must stretch vertically and the new height, H, is much larger

than the original height of R_y that the polymer naturally wants to adopt. When the polymer extends vertically from the lateral repulsion of neighboring polymer chains is referred to the brush condition.

1.3.3   Connection to bottlebrush systems

Within a single bottlebrush molecule, all three polymer physics concepts discussed must be considered simultaneously: solvent quality, semidilute regime, and brush condition (the latter two are shown in Figure 1.7). With two independent components: side-chains and main-chain, each having three solvent qualities, a total of nine solvent qualities are possible for a bottlebrush system. The dense grafting of side-chains creates an inherent semidilute regime centralized around the main-chain regardless of the concentration of the overall solution. In addition, due to the grafting of the side-chains, the neighboring polymer chains repel each other causing the side-chains to stretch radially from the main-chain. However, the main-chain is also a flexible polymer so the main-chain will also extend, but by how much? Many attempts have been made to answer this question. Instead of developing a clear understanding of the interplay of physic within the bottlebrush architecture, the conformation of bottlebrush systems has been a topic a controversy. Here, we will give an overview of the bottlebrush architecture and summarize the controversy by considering the representative work in literature.
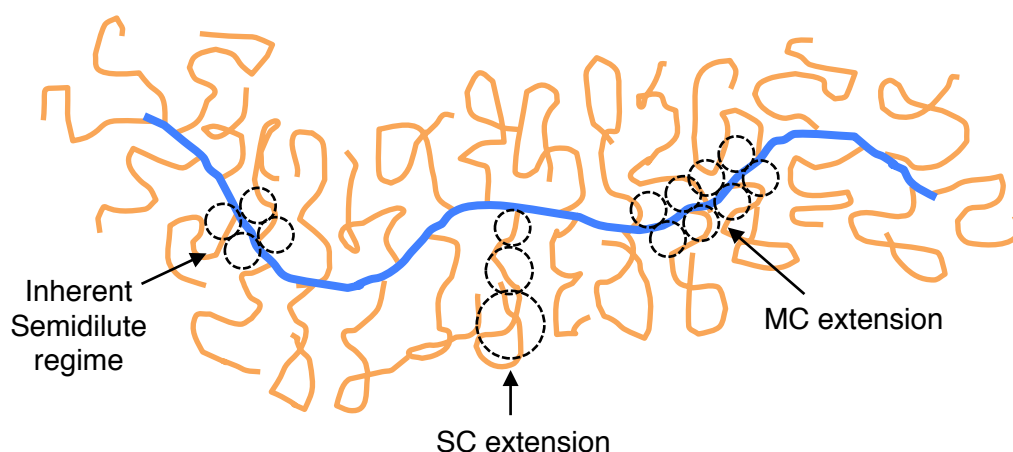
Figure 1.7. Interplay of polymer physics within a bottlebrush polymer. The dense grafting of polymers onto a main-chain results in an inherent semidilute regime centered around the main-chain. One consequence of the inherent semidilute regime is the extension of the side-chains (SC) and of the main-chain (MC).

1.4   Architecture and structure of bottlebrush polymers – An overview

The key feature of bottlebrush polymers (BBPs) is the extension of the main-chain (MC) from the excluded volume interaction of the side-chains (SCs).   The main-chain and the side-chains are all perturbed, but the high side-chain to main-chain ratio results in significant extension of the main-chain and slight extension of side-chains. The excluded volume interactions of the side-chains can be maximized by the following parameters and conditions of the bottlebrush polymers: long main-chain, long side-chains, dense grafting of the side-chains, and good solvent conditions. Although great efforts have gone into understanding the conformation of bottlebrush polymers, side-chains and the main-chain, experimental results probing the main-chain conformation without contribution from the side-chains are missing in the literature. Instead, the main-chain conformation has been inferred from data from the overall molecule. With theoretical approaches predicting a wide range of conformations, experimental observations are essential to discriminate among the existing models.

1.4.1   Multiple length scales in a single bottlebrush polymer

With many polymeric chains in the architectural make up of bottlebrush polymers, the R_{e-e} of the overall molecule is not well-defined and in light of the hierarchal structure, the conformation of the overall molecule cannot be fully described by the R_g. Instead, there are multiple length scales (Figure 1.8) that relate to the architectural parameters of bottlebrush polymers: side chain length (N_{sc}), backbone length (N_{MC}), and the grafting density (σ). The R_g is depicted by a dashed circle within the overall molecule. Bottlebrush polymers with backbone length of N_{MC} have a much larger R_g compared to linear polymer chains with the same length, but the R_g of bottlebrush polymers are much smaller compared to linear polymer chains with the same molecular weight. The new measurable length scale, the cross-sectional radius, R_{CS}, is correlated to the length of the side chains, N_{SC}. The grafting density σ relates the two hierarchal domains by controlling the crowding of the side chains in relation to the extension of the backbone. Bottlebrush polymers with identical N_{SC} and N_{MC} can have vastly different sizes R_{CS} and R_g, respectively. For

example, PS side chains with DP of 55 on a PMA backbone (grafting distance of 2.5 Å) has reported a R_{CS} value 5.2 nm[18] whereas PS side chains with DP of 54 on PNB backbone (grafting distance of roughly 6 Å) was reported to be 4.3 nm[19] and PNB backbone with DP of 550 (PS DP of 65) was shown to have an R_g of 26.4 nm whereas PNB backbone with DP of 570 (PS DP of 25) was shown to have an R_g of 20.6 nm.
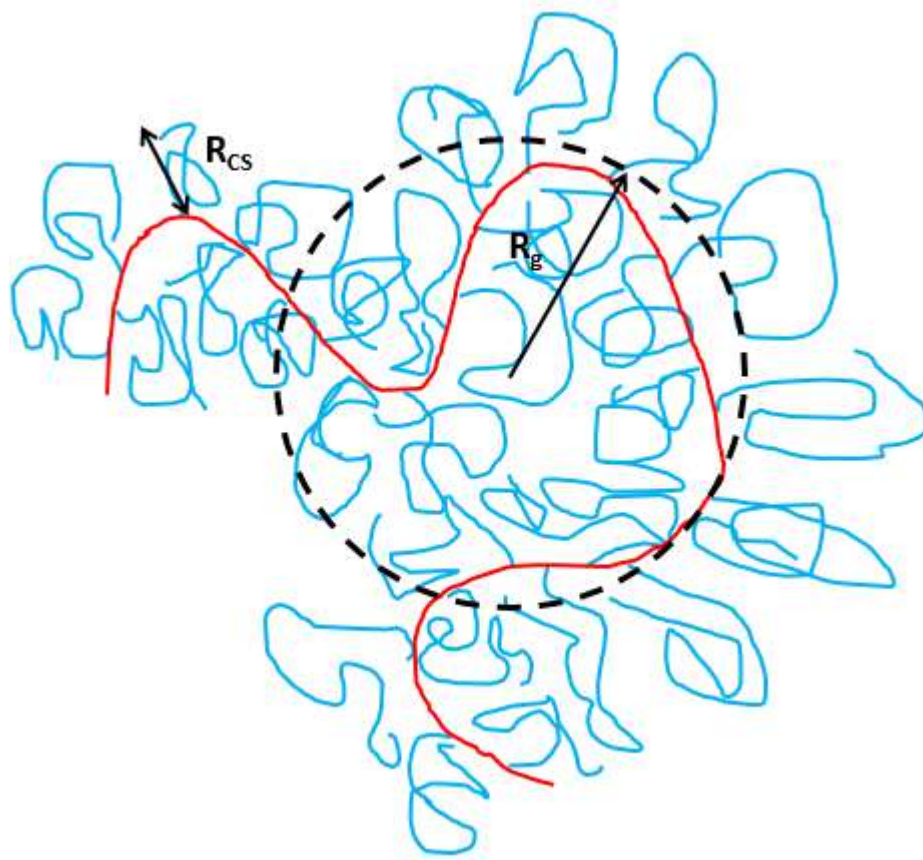
Figure 1.8 Length scales of bottlebrush polymers. A schematic showing the conformation of bottlebrush polymers and length scales measureable with scattering techniques for bottlebrush polymers: The cross sectional radius and radius of gyration. [Courtesy of Pirogovsky]

1.4.2 Inherent semidilute regime within a single bottlebrush polymer

Similar to brushes on a planar surface described by the Alexander-de Gennes model, the dense grafting of the side chains creates a local semidilute regime around a

backbone that causes the concentration blobs to have an extended conformation oriented radially from the backbone, different than that of the self-avoiding walk conformation observed for the semidilute conditions for linear polymers. However, the approximations used for the Alexander-de Gennes brush must be modified for bottlebrush polymers. First, the grafting points are restricted to a flexible polymer chain and the dense grafting criterion of $\sigma \gg N_{SC}^{-3/5}$ is more stringent than on a planar surface. Second, blobs are space-filling. With the concentration blobs extending radially, the amount of space the blobs must occupy increases with distance from the backbone. Therefore, the blobs increase with distance from the backbone. The exact behavior of the side chains is still a topic of debate. Lastly, the chemical nature of which the polymers are grafted to is different. Instead of a rigid surface, bottlebrush polymers are grafted onto a flexible chain that stiffens in response to the crowding effects of the side chains. Experimental measurements show that the Kuhn length of the backbone can increase by up to two orders of magnitude[16] but it is well noted in literature that the backbone tension across the backbone is not uniform[17] (Figure 1.9). The side chains grafted near the ends of the backbone, distances theorized to be approximately the length of the side chains, have radial and azimuthal freedom of movement whereas in the central portion of the backbone (expected for polymers with $N_{MC} > 2N_{SC}$) the side chains have primarily a radial freedom of movement. The radially restricted freedom of movement in the central region of the backbone results in a uniform mechanical tension on the backbone. An additional azimuthal freedom of movement at the ends allows chains to occupy additional space leading to less crowding of the side chains. The overall effect is a nonuniform distribution of mechanical tension on the backbone such that, approaching the ends, a decaying mechanical tension profile on the backbone is observed. When the backbone is not sufficiently long enough to have the central region, the decaying tension profile corresponding to the corona-ends dominates the backbone behavior. These molecules are better described as star polymers as opposed to bottlebrush polymers.
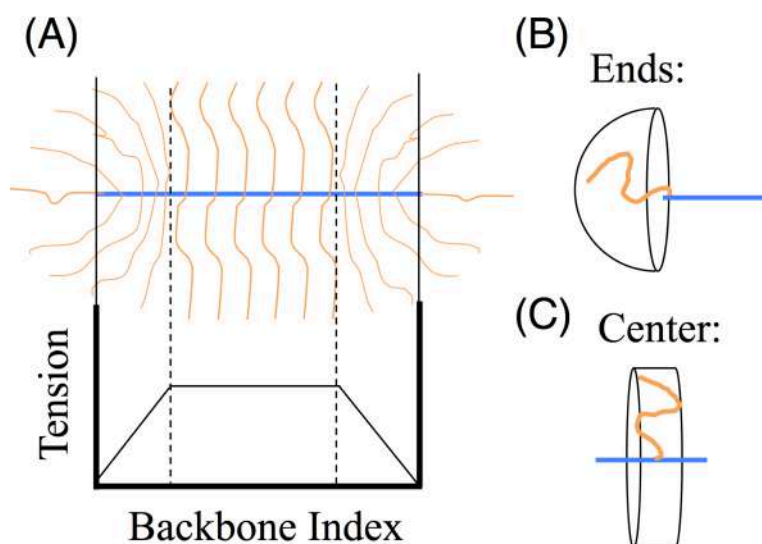
Figure 1.9 Tension profile in bottlebrush polymers. (A) Tension profile expected in a bottlebrush polymer. The nonuniformity of tension arises from the reduced side-chain interactions at the ends of the main-chain (B) where side-chains can extend in both radial and azimuthal directions where as side-chain interactions in the center of the main-chain (C) the side-chain can only extend in the radial direction increasing the side-chain interactions.

In contrast to linear chains where the concentration regimes and solvent quality can be assessed independently for isolated polymer chains, the local semidilute regime of bottlebrush polymers restricts the solvent quality and concentration arguments to be made simultaneously; that is, the length scale of thermal blob and concentration blob is always present. For good solvents, the side chains consist of the thermal blobs described by a self-avoiding walk inside concentration blobs that have an extended conformation due to the crowding as discussed above. To more precisely describe the behavior, Panyukov et al.[17] determined eight regimes for bottlebrush polymers with chemically identical backbone and side chains for varying solvent quality and distance between grafting points: (1) swollen brush and swollen backbone, (2) swollen brush and Gaussian backbone, (3) swollen brush and fully stretched backbone, (4) θ brush and Gaussian backbone, (5) θ brush and fully stretched backbone, (6) collapsed brush and weakly stretched spacer, (7) collapsed brush and fully stretched spacer, and (8) collapsed brush and unstretched spacer.

In the following section, we will review the current understanding of bottlebrush polymers in literature (theory, simulations, and experiments). In light of these reported

understandings, we present our scattering data from scattering contributions from the main-chain only; the side-chains have been contrast-matched to that of the solvent. We employ a thorough analysis without invoking theoretical models in attempts to fit our data and, instead, test the validity of the models ascribed in literature.

1.4.3   *Architectural Parameters and Behavioral Regimes*

Bottlebrush polymers are characterized by three key parameters: long side-chain length, $N_{SC} >> 1$, long main-chain length, $N_{MC} >> N_{SC}$, and dense grafting of side-chains, $\sigma^{-1} >> R_{SC}$, where N_{SC} is the SC length, N_{MC} is the MC length, and σ is the number of side-chains per unit distance. When any of these parameters fail to be met, the bottlebrush condition of side-chain repulsion induced stiffening of the main-chain is also not satisfied (Figure 1.10A). When the MC length becomes sufficiently short, the brush resembles star-like polymers. With short SC lengths, the molecule begins to resemble a linear polymer. Figure 1.10A is a representation for where the asymptotic limits would be with BBPs occupying the top-right corner of the parameter space.

Simulated and experimental molecules from literature are plotted in the parameter space (Figure 1.10B). The asymptotic regimes are labeled; however, as will be discussed in the literature analysis, the crossovers between the regimes have yet to be determined and are included only to serve as representations. Juxtaposed are the molecules that are studied in this thesis work (red), composed of molecules of long and short SCs and wide-spanning MC lengths relative to the molecules studied in literature.
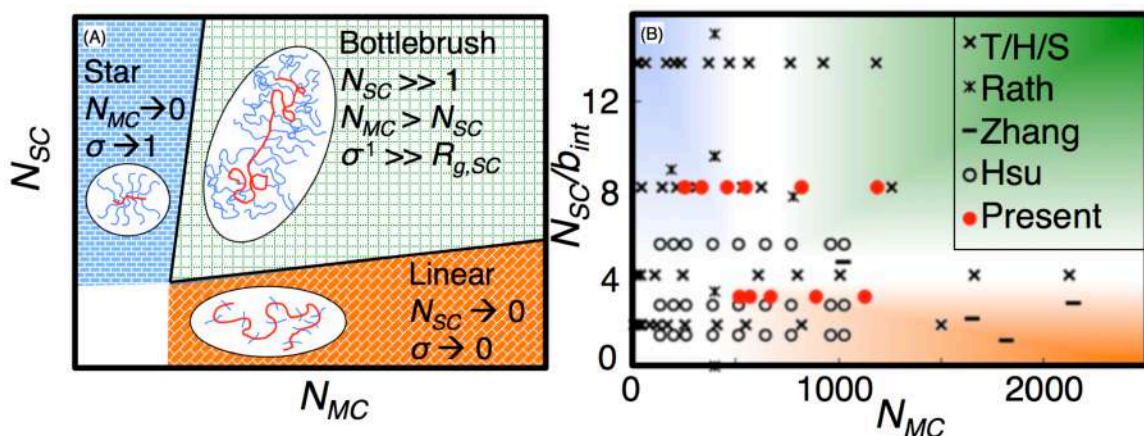
Figure 1.10. Bottlebrush polymer parameter space. (A) Parametric mapping of graft polymer regimes. (B) Molecules studied in this work overlaid with experimental and simulated molecules investigated in literature on the parameter map. T/H/S = Terao/Hokajo/Sugiyama, R = Rathgeber, Zhang = Zhang, and Hsu = Hsu.

1.4.4   Experimental Molecules – Deviation from Theoretical polymers

Here, we want to note that the graft spacing has been omitted in the representation of the parameter space due to the small graft spacing of experimental and simulated work and the condition that $R_{e-e,SC} > \sigma^{-1}$ is easily met as monomer lengths are on the Ångstrom length scale. However, early theoretical approaches had considered systems with large graft spacings. With many main-chain units in between graft points, the main-chain was predicted to be flexible. For polymers with grafting density ~1, side-chains are grafted on much smaller length scales than a persistence segment. Thus, the smallest length scale of synthetic molecules cannot be described as a Gaussian distribution, but a stiff persistent segment. The molecules commonly considered in theory and the molecules investigated in experiments are two different classes of molecules. This work begins to explore the consequent deviations arising from the absence of the thermal blob length scale between graft points in experimental molecules. Also, we want to emphasize a lack of MC length dependence on any of the parameters discussed. Our results show a significant dependence of the MC conformation on the MC length, not just the SC length.
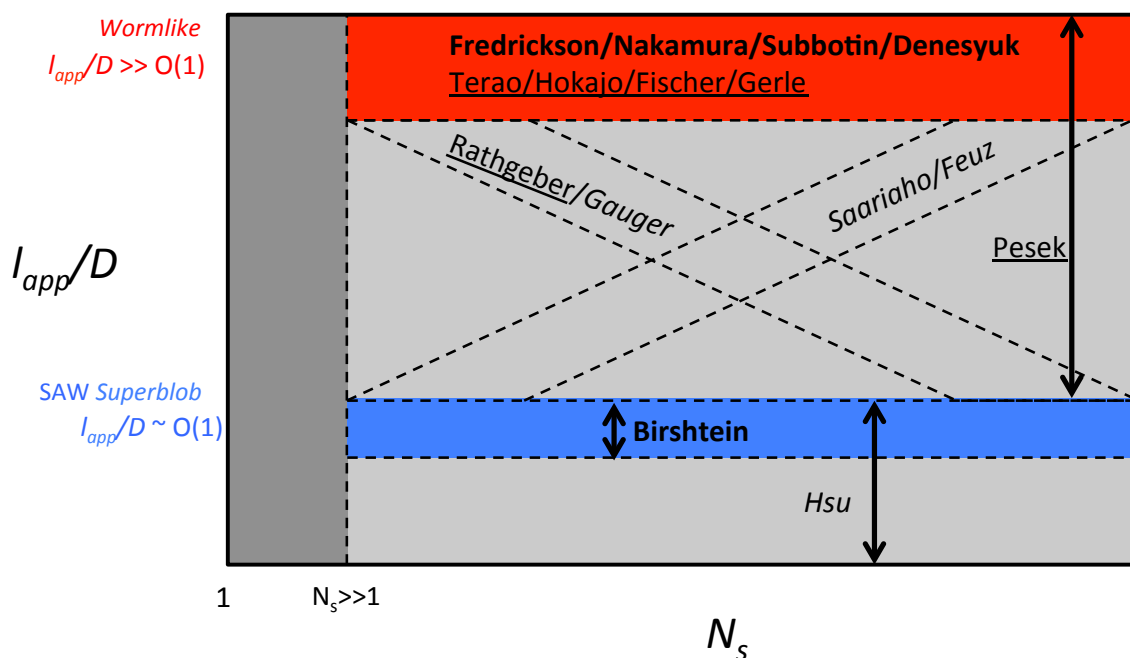
Figure 1.11 Summary of models in literature of BBP conformations. Theoretical approaches are in bold, simulations are italicized, and experiments are underlined. In red are those who predict a worm-like chain/cylinder with large apparent persistence length relative to the cross-sectional diameter, and in blue are those who predict a SAW of superblob with an apparent persistence length on order of the cross-sectional diameter.

1.5   Literature analysis of bottlebrush polymers

Having discussed the complexity arising from the bottlebrush architecture, we shift our focus to the models proposed in literature to describe the BBP conformation. Unless otherwise specified, the literature discussion will focus on good solvent conditions. With θ solvent work constituting a small fraction of the conformation analysis of BBPs in literature, we reserve discussing literature work on θ solvent conditions to Chapter 3, where θ solvent results are presented. For a more in-depth discussion of literature work, see Appendix B.

Most literature works ascribe to either the self-avoiding walk (SAW) of super blobs model, or the worm-like chain/cylinder (WLC) model, or show an architecture dependence between the two models (Figure 1.11 - theoretical work are in bold, experimental work are underlined, and simulation work are italicized). First proposed by Birshtein et al.[18], the

SAW of super blobs model predicts the persistence length, l_p, to be on the same order as the thickness of the chain, D, *i.e.*, $l_p/D\sim O(1)$. To come to this conclusion, they argued that the side-chains do not impose any free energy restrictions on bends larger than the thickness since the side-chains can rotate from the concave to the convex portion of the bend. Fredrickson[19] attempted to verify this claim by minimizing the free energy of bending a torus[20] (with bending radius larger than the thickness of the chain) with respect to the semidilute interaction taking into consideration the concentration profile that arises from the redistribution of the side-chains from the concave to convex portion of the bend. He came to the opposite conclusion of Birshtein showing that the $l_p/D>>O(1)$, consistent with nematic ordering of bottlebrush polymers observed by Cao and Smith[21] and pioneering theoretical work by Onsager[22]. Therefore, Fredrickson claimed that bottlebrushes behave as a wormlike chain/cylinder (WLC). From the defining characteristic, the SAW of super blobs and WLC are mutually exclusive models, and in literature, have become the opposing bounds of bottlebrush behavior.

Differing theoretical predictions do not necessarily lead to a controversy in literature since simulation and experimental efforts can clarify the disagreements in the theoretical models. However, for bottlebrush polymer conformation analysis, this was not the case. Instead of coming to a deeper understanding of the conformation of bottlebrush polymers, additional theoretical, simulation, and experimental efforts had deepened the controversy as both mutually exclusive models were verified: WLC[16,23–32] and SAW of super blobs[33–35]. In addition, the results showed reverse trends: with increasing side-chain length, (1) some works predict the behavior approaches WLC behavior[36,37], favoring the predictions by Fredrickson whereas (2) some works predict the behavior approaches a SAW of super blobs model[38–40], favoring predictions by Birshtein. In addition, the complexity of the conformation of bottlebrush problem was highlighted through additional different behavioral regimes at shorter side-chain and main-chain lengths[25,41,42]. Generally, theoretical approaches neglect end effects and only consider the central portion of the main-chain. Within the WLC framework[43], early experimental work by Terao et al.[30] showed end effects for synthetic molecules can be neglected for $N_{MC} \geq N_{SC}$, which has been

supported by a recent experimental work by Pesek et al.[42]. Only recently has this assumption been called into question by simulation and experimental work[33–35,44–46] showing that $N_{MC}>>N_{SC}$ to be in the main-chain length asymptotic limit of a bottlebrush polymer.

We want to emphasize that the abovementioned controversy in literature considers only the dilute conditions. An additional degree of complexity is introduced in the semidilute regime, as conformational diversity likely exists within each semidilute regime[40,47–50]. However, before discussing the conformation within each semidilute regime, the semidilute regimes have to be identified to assure the comparison of identical regimes. Unfortunately, the number of concentration regimes itself has been called into question as theoretical work by Borisov et al.[47] predict four whereas simulation work by Paturej and Kreer[48] show five concentration regimes. In addition, it is not only the number of regimes that is a topic of debate, but also the order in which specified semidilute regime occurs with increasing concentration are different between Borisov and Paturej. For details, see Appendix B.

Recently, a model has been developed for bottlebrush polymers in the melt which, we believe, help provide great insight that could be modified for the conformational behavior in solution. That model was by Paturej et al.[51] in which they identified two distinct length scales (for 3 length scale regimes). On the smallest length scale, $r<\xi_{Ten}$, the main-chain behaves as linear polymer (RW in theta, SAW in good). On this small length scale, the main-chain does not 'feel' the presence of side-chains. On intermediate length scales, $\xi_{Ten}<r<R_{SC}$, the excluded volume of the side-chains is felt by the main-chain and must adopt an extended array of tension blobs. On the largest length scale, $r>R_{SC}$, the excluded volume interactions of the side-chains are screened and the main-chain behaves as an ideal chain in the melt.

We want to conclude the literature review section by noting a few themes that we believe have reasons for concern. First, many works supporting the WLC model have incorporated an additional contribution to the bare persistence length of the system[23,24,31,36]

$$l_p = l_{p,0} + l_{p,b}$$

(1.1)

We believe this additive treatment of persistence length can obscure important interactions as the bare persistence length and side-chain excluded volume contributions are mechanistically distinct. The former is heavily influenced by the bond angles between subsequent monomers whereas the latter is due to the excluded volume imposed by the side-chains. Second, experimental verification of the WLC model has been largely based on the quality of fits to scattering profiles of the overall brush. The primary flaw in this criterion lies in the fact that many form factor models have been shown to fit the scattering profile of the overall brush[41,42,49,50]. The nondiscriminatory nature limits any model verification capabilities. This method has not only been reported to verify the WLC model, but led to the assumption[30] that end effects become negligible for $N_{MC} \geq N_{SC}$. Therefore, the main-chain length condition also is a reason for concern.

1.6   Purpose of this work

1.6.1   Conformational issues in literature to be addressed in this work

An overarching theme in literature work predicting wormlike chain of bottlebrush polymers is the presupposition of the wormlike chain itself. All theoretical works predicting a wormlike chain behavior discussed here invoke the wormlike chain assumption to some extent prior to their conclusion. Fredrickson[19], Nakamura[24], and Subbotin[23] invoke the curvature-bending free energy relationship for a wormlike chain, all concluding a $l_{p,app}/D \sim N_{SC}^{\alpha}$ relationship with $\alpha > 0$. Denesyuk[25] incorporated scaling results obtained for a wormlike chain when calculating the scaling relationship for the end-to-end distance of the main-chain. Likewise, simulation and experiments 'predicting' a wormlike chain behavior did not validate the wormlike chain assumption, but performed fits to obtain characteristic parameters of a wormlike chain. Fitting analysis to scattering profiles raises many concerns. Wataoka[41] and Rathgeber[39] demonstrated that SAXS/SANS/SLS scattering profiles can be fit to oblate ellipsoid to elliptical cylinder to worm-like chain model showing no side-chain dependence in the persistence/Kuhn length. With mutually

exclusive models showing fits to scattering profiles, the quality of fits cannot be a method for validating behavioral models, the condition used in literature. Therefore, we seek to verify if the wormlike chain model is a good approximation of a bottlebrush polymer without invoking wormlike chain assumptions/fits (Chapter 2).

The prevailing belief that the main-chain length required to achieve the asymptotic limit is on the order of the side-chain length. Terao[26,27], Wataoka[41], Denesyuk[25], and Pesek[42] showed main-chain length dependence and the longest reported main-chain length required to reach the asymptotic behavior occurred at N_{MC}=120 (for side-chain lengths up to 54 units) by Pesek, showing a transition from a spherical shape to a cylindrical shape. Recently, simulation results by Hsu[34,35,44] and experimental/simulation work by Dutta[46], call for a revision of that understanding. With main-chain length dependence reporting only on the overall shape of the molecule, no experimental reports of conformational dependence on the main-chain length has been discussed. We look at the internal structure and assess the origin of the main-chain length dependence reported by Hsu and Dutta (Chapter 2).

In addition, we compare our results to other models and begin to discriminate models that cannot explain our experimental results. We propose modifications to existent models to match our system in 'dilute' conditions (solvent quality, side-chain length, main-chain length, grafting density, etc.) to consistently explain all of our experimental results (Chapter 2 and 3).

More recent work has acknowledged the significance of long side-chains for experimental work. However, experiments have yet to resolve a side-chain length limit for bottlebrush polymer considerations. Instead, analysis has typically included side-chain lengths as short as N_{SC}=6 repeat units, which is exceptionally short. Our results show a qualitative change in main-chain conformation with side-chain length, distinguishing behavioral regimes (Chapter 3).

In the semidilute regime, lyotropic ordering was observed by numerous groups which indicate a large $l_{p,app}/D$ ratio. However, Bolisetty[49,50] predicts a softening from semidilute interactions, resulting in a decrease in persistence length, the opposite trend required for lyotropic behavior. We provide insight into this controversy in Chapter 3. In addition, simulation results by Paturej et al.[48] predicted four concentration regimes for semidilute solutions, confirming many predictions pioneered by Borisov[47]. However, they differ in the attributed semidilute interaction leading to overall behavior. Our results verify Borisov's analysis (Chapter 3).

1.6.2 Characterization of bottlebrush copolymer systems – self-assembly and crystallization

When two chemically distinct polymers are chemically joined forming what is known as a linear block copolymer, the energetic penalty of interaction of the two polymers results in phase separation for systems with temperature below the order-disorder temperature, $T<T_{ODT}$. The chemical attachment of the two polymers limits the degree of phase separation to micro- and nanoscales forming self-assembled structures known as morphologies[52]. Depending on the interaction parameter, χ, the relative volume fraction of each polymer, and the temperature of the system, a myriad of morphologies can be obtained. When either polymer is semi-crystalline, the phase behavior becomes increasingly complex[53]. For systems where the crystallization temperature, T_c, is below the order-disorder transition, $T_c<T_{ODT}$, in which crystallization proceeds from a preformed morphology, two possibilities exist. First, the semicrystalline component can crystallize within the preformed morphology without any disruption to the morphology. This process is referred to as confined crystallization, typically occurring for block copolymers in which the minor component is the semi-crystalline polymer. The other possibility is that in which the crystallization of the semi-crystalline component disrupts/modifies the preformed morphology. This process is referred to as breakout crystallization. Of course, the block copolymer can be tuned in such a manner that $T_{ODT}<T_c$, in which case the system immediately forms a crystallization driven morphology from a disordered phase. For linear

block copolymers with both components as semi-crystalline polymers, an additional degree confinement and breakout crystallization must be considered.

Although the interplay of self-assembly and crystallization has been well documented for linear systems, very little is known for bottlebrush architecture systems. A few reports have been made on the self-assembly (in the absence of crystallization) of bottlebrush copolymer systems[6–8,54–56] and a more diverse morphological behavior compared to linear block copolymers has been observed. Within the bottlebrush architecture, the two chemically distinct components can be grafted in a variety of ways, which influences the final morphology of the system. Xia et al.[6] and Dalsin et al.[8] have shown that when the chemically distinct side-chains are grafted in blocks along the main-chain (form an effective A-B polymer), large domain spacing can be obtained with the domain spacing being dependent on the main-chain length. Xia et al.[6] and Kawamoto et al.[54] showed that by simply changing the arrangement of the chemically distinct polymers within the bottlebrush architecture, the morphology could be drastically changed. When the side-chains were randomly grafted along the main-chain, smaller morphologies were obtained, with the domain spacing being dependent on the side-chain lengths, different from the main-chain length dependence for the side-chains grafted into blocks along the main-chain. With respect to the phase diagram for linear block copolymers, Gai et al.[55] had shown that bottlebrush copolymers have a higher affinity for lamellar morphology than linear block copolymers by showing a broader lamellar morphology range in the phase diagram. Work by Bolton et al.[56] has shown that specifying the relative volume fraction of each component is not sufficient to characterize the morphology of the system, as is the case for linear block copolymers. They showed that in addition to the relative volume fraction, the relative lengths play a significant role in determining both the size and the specific morphological structure. In addition, Chang et al.[7] has shown complex interactions for low-χ interactions in which a mixed-domain lamellar morphology had led to phase behavior not observed for linear block copolymers.

With the additional complexity in self-assembly behavior with respect to linear block copolymers, the interplay of crystallization is sure to lead to a fascinating array of crystallization behavior, morphological structures, and behavioral trends in bottlebrush

copolymers systems. In Chapter 4, we characterize bottlebrush polymers with two chemically distinct semicrystalline polymers, polyethylene and polycaprolactone, systematically arranged in three different ways within the bottlebrush architecture. We report the self-assembly behavior, crystallization behavior, and the intricate interplay between the two to unveil many interesting properties arising simply from the arrangement within the bottlebrush architecture that are not observed for linear systems.

C h a p t e r   2

BOTTLEBRUSH POLYMERS ARE NOT FRACTALS

2   Introduction

Bottlebrushes exist in a particular corner of the family of branched polymers in which the SC are much longer than the persistence segment ($N_{SC} >> s_{p,o}$), graft points are much closer than the SC radius of gyration ($\sigma^{-1} < R_{g,SC}$), and the MC is much longer than side-chains ($N_{MC} >> N_{SC}$) (upper right region, Figure 2.1A). Decreasing SC length and/or increasing graft spacing reduces SC-SC repulsion, eventually crossing over to the limit of a flexible linear chain. Even if SCs are long and graft spacing is small, decreasing MC length below that of the SCs eventually leads to the regime of star-like polymers. Theoretical studies of bottlebrush polymers generally treat the asymptotic regime of strong SC-SC repulsion.[17–19,23,24] Denesyuk[25] predicts three regimes: (1) $N_{MC} < N_{SC}$, star-like with side chains extending in all directions following Daoud-Cotton; (2) $N_{MC} \sim N_{SC}$, the molecule resembles a stiff cylinder with side-chains executing a 2D SAW perpendicular to the main-chain; and (3) $N_{MC} >> N_{SC}$, WLC much longer than its (long) persistence length, $l_{app}/D \sim Nsc^{3/4}$ and $l_{app} \sim N_{SC}^{5/4}$. Early experimental work by Wataoka et al.[41] showed an oblate ellipsoid form factor could fit the observed scattering pattern for brushes with short main chains ($N_{MC} \leq 9$) and, with increasing main-chain length, an elliptical cylinder provided quality fits. Pesek et al.[42] also inferred a shape transition, but from sphere to cylinder and at a much greater $N_{MC} \approx 120$. Unfortunately, neither experiments nor theory have established the boundaries between these regimes. Today it is not possible to evaluate which synthetically accessible molecules, if any, are in the asymptotic regime (Figure 2.1B).

Theoretical, simulation, and experimental attempts at understanding stiffening (characterized by $l_{p,app}$) behavior of bottlebrush polymers (BBP) has led researchers to an array of different scaling exponents for $l_{p,app} \sim N_{SC}^{\alpha}$ (from α=0-2) and conceptual models (e.g., Wormlike chain and SAW super blobs). Theoretical approaches assume the side-

chain crowding is invariant along the main chain, acknowledging that there is a small region near each end of the main chain where the crowding is less severe (Figure 2.1B). The geometric considerations that give SC grafted near the ends of the MC more space to occupy than SCs grafted in the middle of the MC lead to the expectation that only MC segments within approximately one SC R_g of the MC end have reduced SC-SC interactions. On this basis, theoretical effort has focused on the central portion of the BBP where fully developed SC-SC repulsion is independent of position along the main-chain. Here, we present scattering patterns of the backbone itself along with the corresponding overall scattering pattern. Our results show that SC-SC repulsion builds up very gradually such that bottlebrushes that are accessible to synthesis or simulation are long enough to access fully developed SC-SC repulsion. Consequently, increasing MC length changes the conformational character of the molecule, defying self-similar behavior and scaling arguments.

2.1   Literature Overview

The works in literature have been thoroughly discussed in section 1.3. Here, we summarize, the work related to the focus of this chapter – bottlebrush polymer in good solvent.

Theoretical treatments of bottlebrush conformation has led to two mutually exclusive models: a SAW of superblobs and a wormlike chain (cylinder) model. The former, pioneered by Birshtein et al.[18], that gradual bends with bending radius, R, larger than the diameter, D, of the brush does not increase crowding of SC due to freedom to redistribute from the concave side of the bend to the convex side. Consequently, the main-chain stiffness was on the order of the brush thickness, $l_{p,app}/D \sim O(1)$. The conformation of the molecule on longer length scales is governed by brush-brush repulsion between super-blobs of size $\sim D$, hence, a SAW of super-blobs (in both good and theta solvent conditions). Fredrickson[19] applied the Daoud-Cotton (for star polymers) modified for a torus representing a bottlebrush with a curvature $R>D$ and concluded a bottlebrush has a much longer apparent persistence length, $l_{p,app}/D \sim \sigma^{15/8} M^{9/8} >> O(1)$, causing bottlebrush polymers to behave like WLC—the opposite conclusion as Birshtein. Subbotin et al.[23], Nakamura et

al.[24], and Denesyuk[25] similarly viewed bottlebrushes as WLC. A large $l_{p,app}/D$ leads to lyotropic behavior,[22] so experimental observation of lyotropic order in concentrated solutions of bottlebrushes[21,57–59] was interpreted as evidence that $l_{p,app}/D>>1$.

Numerical and simulation results have not been able to reconcile the stark difference between Birshtein's SAW of super-blobs and Fredrickson's WLC. A Scheutjens-Fleer self-consistent-field approach employed by Feuz et al.[36] showed significant dependence of $l_{p,app}/D$ on N_{SC}. They found a crossover from the predictions of Birshtein, $l_{p,app}/D \sim O(1)$ for short side-chains, to Fredrickson, $l_{p,app}/D \sim N_{SC}{}^x$ for long side-chains. To the contrary, simulations by Gauger[38] showed the reverse dependence of N_{SC} on $l_{p,app}/D$, with $l_{p,app}/D$ decreasing with increasing side-chain length. Monte Carlo simulations of Saariaho et al.[37] showed $l_{p,app}/D$ is independent of N_{SC}, in accord with Birshtein; however, they also showed that increasing bead size could induce large $l_{p,app}/D$, consistent with Fredrickson. More recently, Monte Carlo simulations by Hsu et. al.[34,35,44,45] showed $l_{p,app}/D \sim O(1)$ in the asymptotic limit. Of particular interest to the present study, their simulations show that the MC length required to reach the asymptotic limit is roughly 2 orders of magnitude greater than the number of MC units in a super-blob.

Experimental studies have often been interpreted as confirming bottlebrushes are wormlike chains by the quality of fits to WLC models, and focus on determining the relationships between the N_{SC}, D and $l_{p,app}$. Terao et al.[26,27] and Hokajo et al.[28] showed R_g of the bottlebrush increases linearly with N_{SC} for N_{SC}=15, 33, and 65. Sugiyama et al.[29] added N_{SC}=113 to the prior set, supporting a quadratic increase of R_g with N_{SC} for N_{SC}=15, 33, 65 and 113 with similar N_{MC} range. Rathgeber et al.[39] analyzed scattering profiles (combined SLS and SANS) invoking a WLC model with excluded volume interactions to fit the data; the fit yielded $l_{p,app}$=70 nm independent of N_{SC} for N_{SC} from 22 to 98 (*i.e.*, $l_{p,app}/D$ *decreases* as Nsc increases), which suggests that the long $l_{p,app}$ is not due to SC-SC repulsion. Recently, Pesek et al.[42] demonstrated that bottlebrush SANS scattering profiles could be fit by any of a number of form factor models (Guinier-Porod, flexible cylinder, or rigid cylinder), leading to disparate values of $l_{p,app}$ for a single sample ($l_{p,app}=l_{p,NB}$=7nm,

$l_{p,app}$=110nm, and $l_{p,app}$=L=400nm (L is the fully extended contour length, respectively). Nevertheless, many experiments[16,26–29,31,32] have been interpreted by applying WLC to analyze the data, leading to large $l_{p,app}$, up to $l_{p,app}$ ~208nm ($l_{p,app}/D$~40). Thus, invoking the WLC model leads to large $l_{p,app}/D$, from which it is widely concluded that bottlebrushes are worm-like chains. The results we present contradict that view.
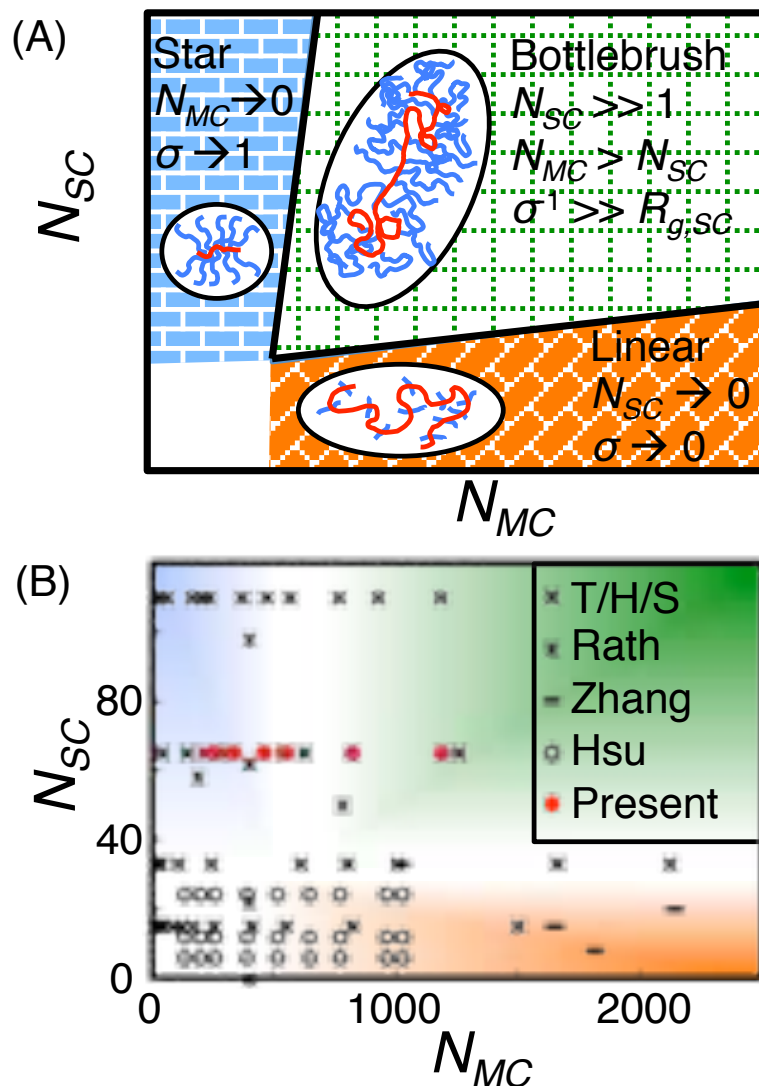
Figure 2.1. Bottlebrush polymer parametric space. (a) Parametric mapping of graft polymer regimes. (b) Molecules studied in this chapter overlaid with experimental and simulated molecules investigated in literature on the parameter map. T/H/S = Terao/Hokajo/Sugiyama, Rath = Rathgeber, Zhang = Zhang, and Hsu = Hsu.

To reveal the conformation of the main chain in a BBP requires $N_{SC} \gg 1$, $N_{MC} \gg N_{SC}$ and $c < c^*$, which in turn requires solutions with concentration less than 1.0%wt. The main chain is roughly 1% of the molecule, consequently MC units are present at a mere 0.01%wt. Neutron scattering, with contrast matching, enables selective measurement of the scattering profile of the MC; however, the signal is very weak under the conditions of interest.

Here, we report direct measurements of the MC conformation of a BBP and the overall conformation of a corresponding BBP by using matched pairs, one with hydrogenous (hSC) and the other with perdeuterated (dSC) side chains. Using a deuterated solvent that is contrast matched to dSC provides scattering contrast for the entire hSC-BBP and for the main chain of the dSC-BBP. SANS patterns were acquired at the lowest concentration for which dSC-BBP gave a measurable signal (1%wt). Unfortunately, we were unable to make meaningful measurements under truly dilute conditions. To complement the SANS measurements, hSC-BBP were also characterized using SAXS, SLS, and DLS, all of which have sufficient sensitivity to characterize dilute solutions.

Six MC lengths are examined, all of which are relatively long in the context of prior experimental literature (Fig 2.1B). Filling this gap in the prior literature reveals that, when taken together, the scattering patterns for the whole bottlebrush and for the main chain of a matching bottlebrush powerfully discriminate among different models of bottlebrushes in good solvent. The results demand a significant revision of current thinking about existing bottlebrush polymers, definitively showing they are *not* worm-like. Further, the results show that the asymptotic limit that has been the focus of theory has yet to be reached in experimental molecules.

2.2 Experimental section

2.2.1 Synthesis approach

For elucidating the branching affects on molecular conformation in bottlebrush polymers, grafting-through synthesis was chosen for well-characterized architectural

parameters with precise control of length of the side-chains and the grafting density. The chosen approach follows the ROMP (Grubbs catalyst 2nd generation) synthetic procedure of ROMP synthesized via ATRP detailed by Xia et al.[6] The specific procedure is detailed in the SI. The samples were characterized via gel permeation chromatography (GPC) and Multi-angle laser light scattering (MALLS), static light scattering (SLS), small-angle neutron scattering (SANS), small-angle X-ray scattering (SAXS), and dynamic light scattering (DLS).

2.2.2   Synthesis by Pirogovsky[60]

Styrene and 10-undcyn-1-ol (98%) were purchased from TCI America. Styrene-d8 was purchased from Polymer Source. Deuterated Chloroform (CDCl3) w/o TMS was purchased from Cambridge Isotope Laboratories. Tetrahydrofuran (THF, ACS grade, manufactured by EMD), Hexanes (ACS Grade, manufactured by BDH), Ethyl Acetate (HPLC grade, manufactured by J.T. Baker) and Dichloromethane (DCM, ACS Grade, manufactured by J.T. Baker) were purchased from VWR. N-(3-Dimethylaminopropyl)-N'-ethylcarboimide hydrochloride (EDC, >99%) was purchased from ProteoChem. Exo-5-Norbornene-2-Methanol (97%) was purchased from Frinton Laboratories. All other chemical reagents were purchased from Sigma Aldrich and used as received.

2.2.3   Small Angle Neutron Scattering – NIST

At NIST, small angle neutron scattering experiments were carried out on the 30m cold neutron SANS instruments on beamline NG-3 using refractive lens to improve signal at low-q. Patterns were taken at three different configurations: (1) 6Å neutrons, 7 guides, and 1.3m sample-to-detector distance (SDD); (2) 6Å neutrons, 5 guides, and 4m SDD; and (3) 8.4Å neutrons, 0 guides, and 13m SDD with refractive lens. The total q-range spanned $0.0015 < q$ [Å^{-1}] < 0.5. The samples were dissolved in d-THF and d-Toluene and placed into 2mm banjo cells. For contrast matched side-chains, dPS was used. The solvent selected was dTHF which offered the same scattering light density as dPS($SLD_{dTHF} = 6.4 \times 10^{-6}$ Å^{-2}, $SLD_{dPS} = 6.4 \times 10^{-6}$ Å^{-2})[61]. The concentrations used were 1% (by weight)

unless otherwise specified. Temperature was controlled using a circulating water bath in aluminum sample changer.

2.2.4 Small Angle Neutron Scattering – ORNL (Preliminary experiments)

SANS data was acquired at ORNL-HFIR using 40m GP-SANS on CG-2 as well. Solutions were placed into 2mm banjo cells with temperature control by peltier temperature controller. Patterns were acquired at three configurations: (1) 4.72Å neutrons, 7 guides, 0.3m SDD, (2) 4.72Å, 5 guides, and 6m SDD, and (3) 12Å neutrons, 0 guides, and 18.5m SDD. The total q-range spanned $0.0012 < q$ [Å^{-1}]< 0.8. The concentrations used were 1% (by weight) unless otherwise specified.

2.2.5 Small Angle X-ray scattering – ALS-LBNL

SAXS data was acquired at ALS-LBNL on beamline 7.3.3. The wavelength and energy used were 1.24 Å and 10 KeV, respectively. The q-range accessible was $0.006 < q$ [Å^{-1}]< 0.2. The samples were dissolved in toluene at roughly c=1% and the solutions were placed into borosilicate capillary tubes with 1.5-2mm in path length. Lower concentrations were achieved by diluting the c=1% solution.

2.2.6 Dynamic Light scattering

DLS experiments were carried out on Brookhaven Instrument Company ZetaPALS instrument with integrated laser light source (λ= 632.8nm). The detector at 90° position was used. 10mm path length cuvettes at concentrations approximately 0.5mg/mL in THF was used as the sample holder.

2.2.7 Static Light Scattering

SLS data was acquired using a BI-200SM goniometer from Brookhaven Instrument Corporation with coherent sapphire laser, λ=488nm, and maximum power of 75mW. Decalin was used to match the refractive index of the vat. The samples were dissolved in

toluene at roughly c=1% and the solutions were placed into scintillation vials. Lower concentrations were achieved by diluting the c=1% solution. The q-range for SLS was $0.0006 < q$ [Å^{-1}] < 0.004 and in conjunction with SANS, a wider q-range could be elucidated.

2.3   Results – Overall and main-chain scattering profiles

2.3.1   Dilute scattering of the overall brush

Static Light Scattering (SLS) and Small Angle X-ray Scattering (SAXS) patterns the overall BBP were measured at dilute conditions (0.1%wt) in a good solvent (toluene) for the side-chains (Figure 2.2). Following Rathgeber et al.[39,40], Zhang et al.[31], and Bolisetty et al.[49,50] we combine SLS ($0.0006<q$[Å^{-1}]<0.004) and SAXS ($0.006<q$[Å^{-1}]<0.2) to capture the Guinier plateau at $q<0.002$ Å^{-1} and the Porod region at $q>0.02$ Å^{-1} (using a power-law interpolation across the gap from $0.004<q$[Å^{-1}]<0.006). The qualitative shape and features of the scattering profile were consistent with the prior literature[31,33–35,39,40,42,44], showing three distinct scattering regimes: Guinier plateau, Porod regime, and surface scattering regime. The q-boundary between the first two regimes was identified using the maximum in the Holtzer plot, qI vs. q (q^*_H, Figure 2.2B); and the boundary between the latter two regimes was identified using the peak in a Kratky plot, q^2I vs. q (q^*_K, Figure 2.2c). This treatment of the data extracts physically significant length scales—without invoking theoretical models[31,34,39,40,42]. The overall size of the bottlebrush increases with the MC degree of polymerization, DP$_{mc}$, (Table 2.2, $d_H=2\pi/q^*_H$). In contrast, the Porod-surface transition, q_K, is independent of DP$_{mc}$ (Table 2.2, $d_K=2\pi/q^*_K$).

Zimm plots of SLS data (section 2.6) were used to evaluate the radius of gyration of the whole bottlebrush and the second virial coefficient (R_g and A_2, Table 2.2). In accord with prior literature, R_g increases monotonically with MW[26–29]. Based on having similar polymer chemistry to Pesek et al.[42] (identical number of main chain atoms between graft points and using polystyrene side chains), it is surprising that the R_g that Pesek et al. inferred by fitting to a Guinier-Porod model is greater than the R_g values we obtained using

a Zimm plot, despite the fact that the present BBPs have longer SC and longer MC (*e.g.* Pesek *et al.*[42] report R_g=48.9nm for 216-PS54, which is 60% larger than R_g=34.0nm from a Zimm plot for 330-PS65). We checked to see if the molecules's scattering patterns were substantially different by examining Holtzer and Kratky plots of the data of Pesek *et al.* for 216-PS54 at 1%wt: these gave $q*_{H,1\%}$=0.013 Å^{-1} (cf. $q*_{H,0.1\%}$=0.0049 Å^{-1} and $q*_{H,1\%}$=0.012 Å^{-1}) and $q*_K$ = 0.026 Å^{-1} (cf $q*_K$ =0.020 Å^{-1}); for reference in relation to SANS data below, $q*_S$ = 0.086 Å^{-1} for 216-PS54 (cf. 0.067 Å^{-1} for 330-PS65) at the minimum of the Kratky plot. Note that the characteristic wavevectors evident for 216-PS54 in the scattering data itself (without presuming any model) are consistently greater than those of 330-PS65, indicating a somewhat smaller and more compact conformation of the bottlebrush as expected for a polymer with shorter shorter SC and MC. Also note that the experiments of Pesek *et al.* were performed at 1% concentration; when our data are compared at the same concentration the $q_{H,1\%}$ accord well. Thus, the molecules 216-PS54 and 330-PS65 appear to be very similar based on the scattering patterns; the difference in the method of analyzing the data appears to be responsible for the apparent discrepancy in R_g. We return to this in the Discussion.

Calculation of the overlap concentration assuming an isometric shape, $c*_{iso} = 3M/(4\pi N_A R_g^3)$, leads to the (incorrect) impression that c=1% is dilute for 330-PS65 and 550-PS65 (with $c*_{iso}$ of 1.7 and 1.1%, respectively, Table 2.2). However, as discussed in the previous paragraph, we observed $q*_{H,0.1\%}< q*_{H,1\%}$, a shift indicative of significant semidilute interactions at 1% for 330-PS65 and 550-PS65. By comparing SLS patterns of solutions at a series of dilutions, we noted the first dilution that $I(q)/c$ no longer significantly decreased (greater than linear) with subsequent dilution (the lower bound for $c*_{obs.}$, Table 2.2; the next higher concentration is listed as the upper bound for $c*_{obs}$). The onset of overlap occurs at approximately 1/3 $c*_{iso}$, expected for an anisometric conformation.

2.3.2 Contrast matched side-chains reveal the main-chain conformation

To compare the main chain conformation to the overall bottlebrush conformation, we synthesized a pair of macromonomers of similar side chain degree of polymerization (DP); as described in the Experimental section, the hydrogenous side chains have DP_{SC}=63 and the deuterated side chains have DP_{SC}=65 (both have PDI<1.05) and uncertainty less than 10%. From these macromonomers, we prepared three bottlebrushes, attempting to obtain hydrogenous and deuterated pairs with similar DP_{MC}; as described in the Experimental section, the shortest main chains have hSC-BBP DP_{MC} =330 and dSC-BBP DP_{MC} =250, the mid-length main chains have hSC-BBP DP_{MC} =550 and dSC-BBP DP_{MC}=450, and the longest main chains have hSC-BBP DP_{MC} =1160 and dSC-BBP DP_{MC} =820. The deuterated counterparts have main chains that are approximately 20% shorter than the hydrogenous counterpart; therefore, we limit our conclusion to those robust enough to be insensitive to a 20% change in main-chain DP.

To isolate the main chain conformation, we chose d_8-THF as a solvent that has matched scattering length density to poly(d_8-styrene). It is important to note that the scattering power of the side-chain deuterated bottlebrushes is much weaker than that of the fully hydrogenous bottlebrushes; using the square of the ratio of the number of hydrogens to estimate the relative scattering power, the dPS bottlebrushes that is 0.26% as strong as their hPS counterpart. Realizing that the acquisition time to obtain comparable signal/noise would be more than 300x longer than for the hydrogenous bottlebrushes, we sought the lowest concentration that would provide adequate signal/noise within 8 hours of beam time. Comparison of the SANS patterns of the hPS BBP at 1% to SALS/SAXS measurements at 1% and 0.1% concentration (Figure 2.3) shows that SANS patterns and SALS/SAXS patterns agree when compared at the same concentration; however, there is a significant suppression of intensity at q<0.007 Å^{-1}=q_o at 1%wt concentration relative to 0.1%wt. Due to the effect of concentration on measuring time, we did not pursue lower concentrations (*e.g.*, comparable SANS signal/noise would require 16 hours per dPS bottlebrush at 0.5%wt, which would still be affected by overlap).
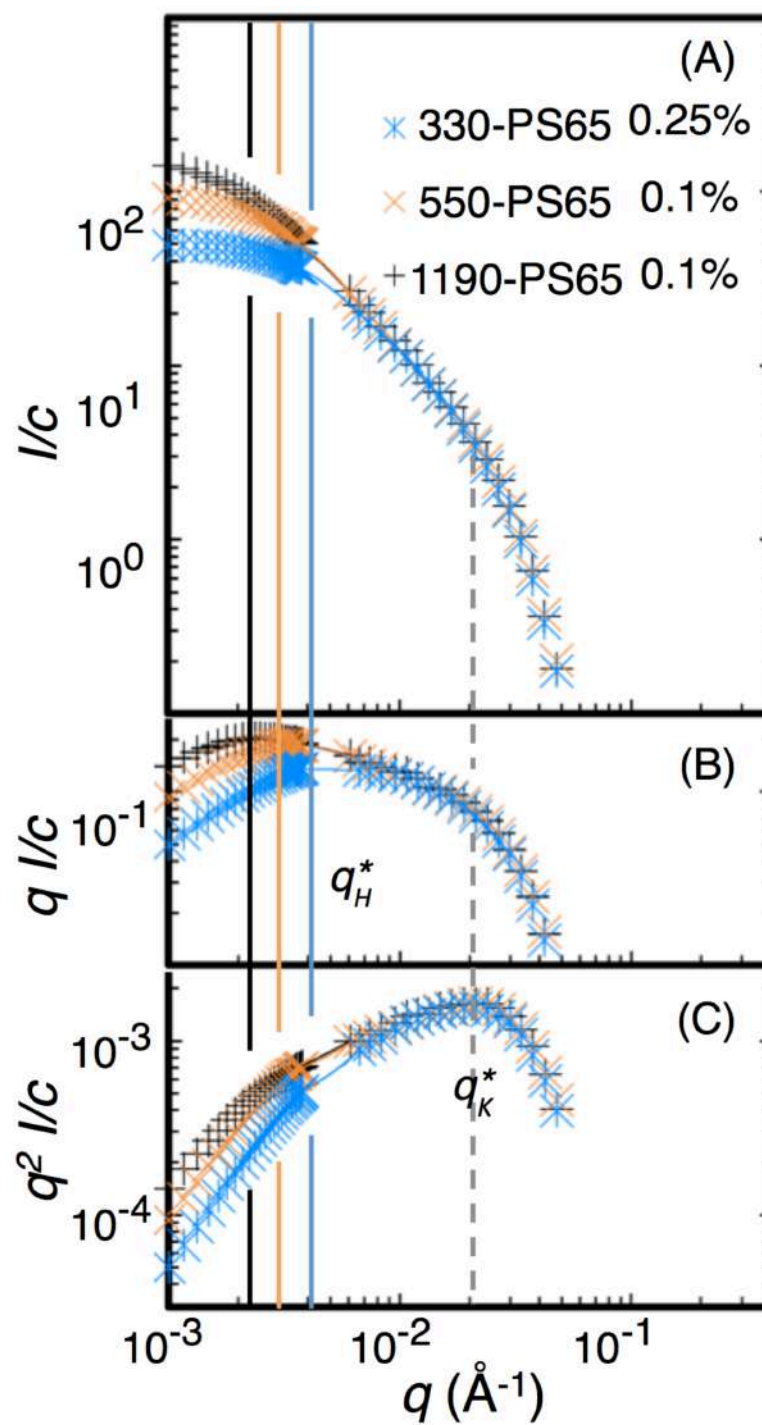
Figure 2.2. SLS/SAXS of bottlebrush polymers in dilute/good solvent. Scattering patterins of dilute conditions shown as (A) I vs. q, (B) Holtzer Plot of qI vs. q, and (C) Kratky plot of q^2I vs. q. Maxima in the Holtzer and Kratky plot were used to identify characteristic wavevector values q^*_H and q^*_K and corresponding length scales (Table 2.1). Data at q up to 0.04 Å^{-1} is provided by SANS, below.

Table 2.1. SLS/SAXS features of scattering in dilute solution and corresponding length scale through the relationship $d=2\pi/q$.

Sample	Holtzer (SAXS/SLS)		Kratky (SAXS/SLS)		Kratky (SANS)	
	q^*_H [Å^{-1}]	d_H [nm]	q^*_K [Å^{-1}]	d_K [nm]	q^*_S [Å^{-1}]	d_S [nm]
330-PS65	0.0048	131	0.02	31.4	0.067	9.4
550-PS65	0.0034	185	0.021	29.9	0.067	9.4
1190-PS65	0.0025	251	0.021	29.9	0.067	9.4

Table 2.2. Results from SLS and DLS and calculated parameters.

Sample	L_{ext} [nm]	A_2*10^5 [cm^{3}mol/g^2]	$R_{g,Zim}$ [nm]	$R_{h,DLS}$ [nm]	R_g/R_H	c^*_{iso} % (wt)	c^*_{SLS} % (wt)	c^*_{SLS}/c^*_{iso}
330-PS65	198	3.2	34	26	1.3	1.7	0.25-0.50	0.15-0.30
550-PS65	330	1.8	50	33	1.5	1.1	0.10-0.25	0.09-0.23
1190-PS65	714	1.7	75	43	1.7	0.6	0.10-0.25	0.17-0.42

Due to the necessity of performing main-chain SANS measurements at concentrations above overlap (i.e., 1%wt overall, <0.01%wt of MC), we need to identify the q-range in which the scattering pattern is unaffected by semi-dilute correlations. As noted above, SAXS and SANS of hSC BBP match when compared at the same concentration, and that 1.0%wt clearly suppresses the Gunier plateau relative to dilute conditions (Figure 2.3). Nevertheless, there is a significant high-q region ($q>q_o$=0.007 Å^{-1}) in which the scattering pattern at 1%wt coincides with the dilute solution pattern. Therefore, we restrict the interpretation of SANS measured at c=1.0% to $q>q_o$ to gain insight into the single chain conformation.
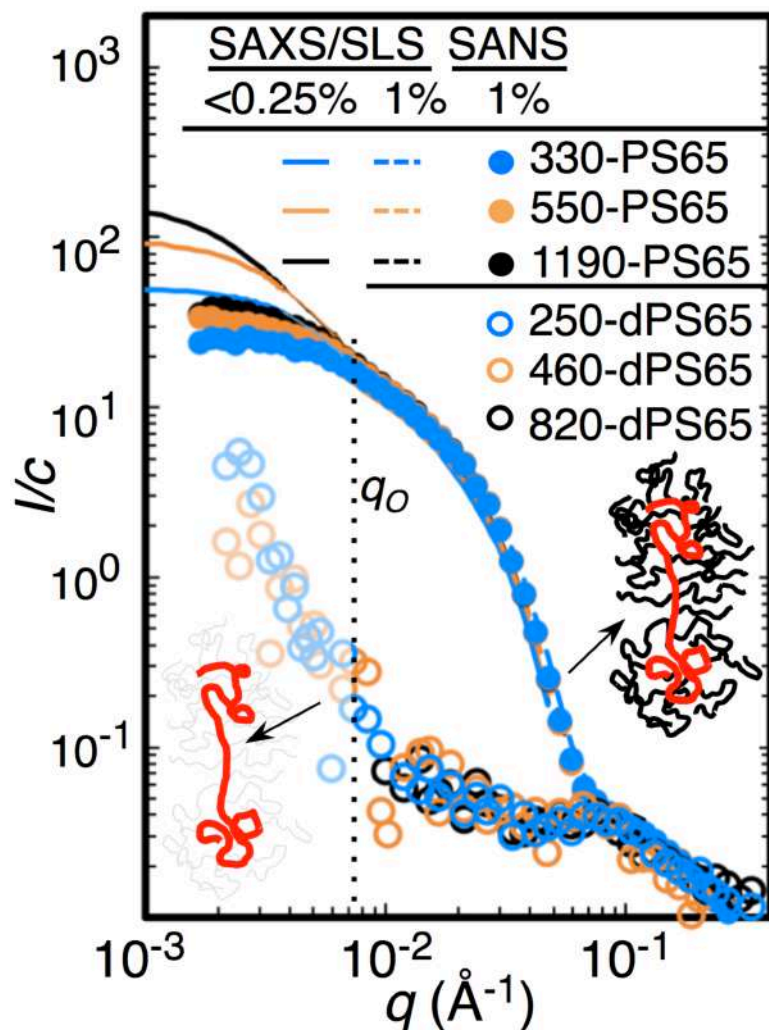
Figure 2.3. Dilute vs. slightly semidilute scattering of bottlebrushes. A comparison of scattering from dilute and c=1% solutions from SAXS/SLS juxtaposed with scattering profile from c=1% of SANS solution. The scattering results from contrast matched side-chains of c=1% are included as well. q_O is identified as the onset of semidilute interactions.

Neutron scattering measurements at 1%wt concentration gave adequate signal/noise out to q=0.4 Å^{-1}, almost a decade beyond the q-value at which the SAXS intensity of dilute solutions became too weak (note the difference in highest-q data in Figure 2.4 relative to Figure 2.2). Consequently, the SANS patterns span the boundary between the surface regime and the local scattering regime, manifested by a minimum in the Kratky plot of the SANS pattern of hSC BBPs (filled symbols, Figure 2.4C), which we use to identify q^*_S. Like q^*_K, q^*_S is independent of MC length.

The SANS pattern at $q>q_o$ is indistinguishable for the three bottlebrushes with contrast-matched side-chains (dPS in dTHF) and is strikingly different from the SANS pattern of the overall bottlebrush. At high-q, we observe the overall and the main-chain $I(q)$ superimpose with a $|m|\approx1$ and deviations begin at q^*_S for the overall $I(q)$ and at q^*_{Sp} for the main-chain I(q) weakens. Surprisingly, the two length scale coincide within error and for our samples, $q^*_{Sp}\approx q^*_S$ and listed in Table 2.3. For $q>q^*_S$, a single fractal dimension is observed with $1<|m|<1.3$ for $I(q)\sim q^{-m}$. In the q-range below q^*_S the scattered intensity from the main-chain hardly varies with q ($m<0.5$), precisely where the intensity rises most steeply with decreasing q for the bottlebrush as a whole (cf. open and filled symbols, Figure 2.4A). This intermediate-q regime extends down to $q^*_L=0.012$ Å^{-1} ($d_L=52.3$nm) at which point an upturn in the scattering intensity is observed. At 1% concentration, overlap between bottlebrushes prevents us from accessing information regarding length scales longer than roughly 70nm (based on q_o, shaded q-range in Figure 2.4). With the similarity in q^*_L and q_o, discussion points regarding q^*_L must be taken with caution. Nevertheless, the consistent results for $I(q)$ at $q > q_o$, for all three of the bottlebrushes with contrast-matched side chains is sufficient to demand a major revision of the literature description of bottlebrushes.
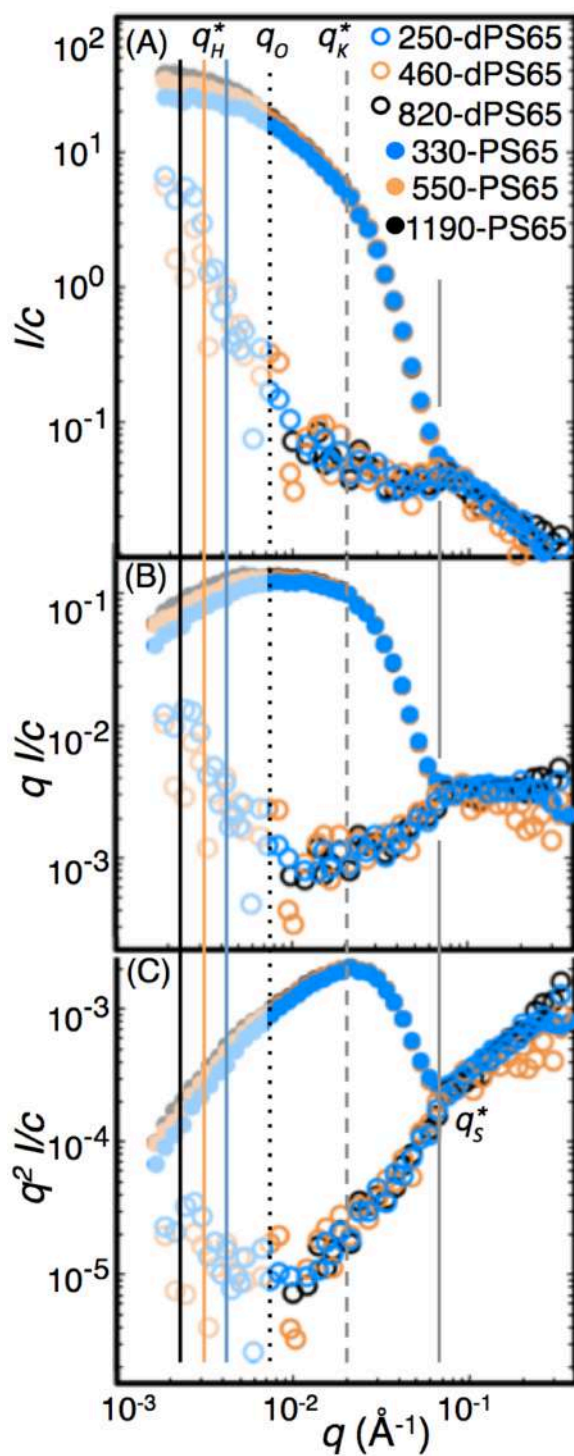
Figure 2.4. Overall and main-chain SANS profile. Main-chain (open symbols) and overall (filled symbols) SANS patterns at c=1%. (a) I vs. q, (b) Holtzer Plot (qI vs. q), and (c) Kratky plot (q^2I vs. q). The length scales, $q*_H$ and $q*_K$, determined from the dilute conditions (Fig. 2.2) are shown. In addition, neutron scattering at high-q regime showed additional extrema in the Kratky plot, used to identify $q*_S$.

Table 2.3. Length scales for main-chain $I(q)$.

Sample	q^*_{Sp} [Å^{-1}]	d_{Sp} [nm]	q^*_L [Å^{-1}]	d_L [nm]
250-dPS65	0.067	9.4	0.012	52.3
450-dPS65	0.067	9.4	0.012	52.3
820-dPS65	0.067	9.4		

2.4   Discussion

We begin our discussion by expounding on the missing result in literature – the main-chain scattering data, which shows a very unexpected SANS profile. Then, we propose a conceptual model that captures the qualitative features of the main-chain and the overall scattering profiles utilizing fundamental concepts. Then we compare and assess our model to our other surprising results: (1) **main-chain length dependence on anisometry** and (2) **reduced overlap concentration**. We conclude by comparing values to literature pioneering the study of bottlebrushes.

2.4.1   Intermediate q-range – coil-rod-coil toy model

To us, the most surprising feature in the main-chain scattering profile is the very weak dependence of $I(q)$ in the range $q_o < q < q_s$. For the three most common polymer fractal behaviors, a decreasing slope is usually associated with stiffening of the polymer chain, approaching the limiting behavior of rods. In relation to the frequent description of bottlebrushes as wormlike or cylindrical, one would expect the weakest q-dependence of main-chain scattering to have $I \sim q^{-1}$ (weak q-dependence relative to a Gaussian coil $I \sim q^{-2}$ or a self-avoiding walk $I \sim q^{-1.7}$) and approach that of a SAW with increasing molecular weight. It is highly unusual to find a polymer that gives a scattering pattern in which the intensity varies more weakly than $I \sim q^{-1}$. To our knowledge the existence of a regime in which the MC scattering profiles is very shallow relative to a rod is unanticipated and highly informative.

To appreciate the physical significance of $I(q)$ with a weaker decay than a rod, it is useful to visualize the increase in the number of scattering units enclosed by a sphere of

increasing size $d \sim 2\pi/q$ that is centered on a particular unit in the main-chain and averaging over spheres centered at all possible MC monomers. Starting from the scale of persistence step (approximately 3.5nm for a bare polynorbornene main chain, corresponding $q{\sim}0.18$ Å^{-1}, slightly less than q_s, and increasing d (decreasing q), we observe a significant q-range in which the number of scattering units enclosed increases *less than linearly* down to $q_u{=}0.012$Å^{-1} ($d_u{=}52.4$nm).

A conceptual explanation is suggested by simulations that show that the main-chain is relatively flexible near its ends. Repulsion between side-chains is minimal at an end of the main chain and accumulates with distance from a MC end. An exceedingly primitive toy model of a main chain that is relatively flexible near the ends and stiff in the middle is a coil-rod-coil. Such a "toy MC" is sufficient to explain a window of wavevector in which I varies more weakly than q^{-1} at intermediate q, corresponding to length scales larger than the diameter of one coil domain d_f ($q < q_f \sim 2\pi/d_f$, where subscript f denotes flexible), and smaller than the length L of the rod domain ($q > q_L \sim 2\pi/L$). As d increases from d_f to L, the scattering power hardly increases (akin to the Gunier plateau of a single coil). On the high-q side of this interval ($q > q_f$), the internal structure of the coil gives a stronger q dependence; and on the low-q side ($q < q_L$), correlations between segments in separate coil domains cause a stronger q dependence. In relation to the present data, we would associate the experimentally observed q_s with q_f of the "toy MC", leading to an estimate of 9.4nm for its coil domains; and we would associate the experimentally observed q_u with q_L of the "toy MC," leading to an estimate of $L{=}52.4$nm for its rod domain.

2.4.2 Tension blob model

The three internal scattering regimes, defined by boundaries q^*_s and q^*_u, of the main-chain scattering pattern indicate that a single internal length scale cannot fully capture the conformational behavior of the bottlebrush main-chain. Our attempt to understand the main-chain scattering pattern led us to an interplay of three different length scales as shown in Figure 2.5A: in increasing size, the intrinsic persistence length of the MC, $l_{p,o}$, tension blob, $\xi_{ten}(k)$, and the induced persistence $l_p(k)$. Here, we are building on the blob

interpretation proposed by Paturej et al.[51] for melts (screened excluded volume interactions which are pronounced in dilute solution). To overview, the Paturej-Rubinstein Model states that bottlebrushes in the melt, for $r<\xi_{ten}$, the MC remains unperturbed with chainlike statistics, Gaussian/SAW, with bare Kuhn length b. For $\xi_{ten}<r<R_{CS}$, the MC can be visualized as an extended array of tension blobs. On the largest length scale, $r>R_{CS}$, the MC can be represented as chainlike statistics of the extended array of tension blobs.

To account for the bottlebrush-solvent interactions in solution and the MC-SC chemical properties used for our molecules, we made the following modifications to the Paturej-Rubinstein Model which are summarized in Fig 5B. First, literature has shown that SC-crowding increases approaching the center of the MC; therefore, we propose a k-dependence on the tension blob, $\xi_{ten}=\xi_{ten}(k)$. Similarly, the reduced crowding near the ends would also lead to a reduction in the brush-brush repulsion and lead us to propose a k-dependence on the overall persistence length as well, $l_p=l_p(k)$. Finally, include a length scale which we define as the intrinsic persistence length, $l_{p,o}$, which defines the length scale with which successive bonds units lose correlation. The number of monomers in the intrinsic persistence length is the intrinsic persistence segment, $s_{p,o}$. Feuz et al.[36] and Subbotin et al.[23] treated $l_{p,o}$ to be that of the persistence length of the bare main-chain, $l_{p,bare}$, whereas Nakamura et al.[24] hypothesized that $l_{p,o}$ would be affected by the short-range interactions between the side-chain and main-chain. In agreement with Nakamura, we argue that even without side-chain repulsion, additions to the chemical structure of the main-chain will apply additional restrictions to the total torsional space leading to an increase in $l_{p,o}$ such that $l_{p,o}>l_{p,bare}$. For example, polystyrene is a polyethylene unit with an additional benzene group which increases the Kuhn step[62] from 1.4nm to 1.8nm even though brush interactions are not yet in play. Without this distinction, a PS would be categorized as a type of graft polymer, which is has yet to have a brush-brush correlation. In addition, Zhang et al.[31] had shown a roughly 3-fold increase in $l_{p,o}$ from side-chains in bottlebrushes compared to $l_{p,bare}$. Most surprisingly, Paturej et al.[51] showed with 4 side-chains per main-chain monomer, the main-chain became rod-like, indicating a significant

increase in $l_{p,o}$ (to longer than L) from that of the bare main-chain and screening the effects of tension and thermal fluctuations.

As can be seen in Fig 2.5B, the interplay of the three length scales with position dependence can lead to a variety of regimes. What is shown is a tension blob interpretation that is consistent with our MC scattering data. In regime I, $r<l_{p,o}$, $\xi_{ten}(k)$, the MC conformation is 'stiff' because the PNB monomers in the MC have yet to lose correlation. In regime II, $\xi_{ten}(k)<r<l_{p,o}$, tension is strong enough to affect the local conformation and affect the bond rotations, still leading to a 'stiff' conformation. Regimes I and II would correspond to $q>q^*_s$ which is consistent with a $1<|m|<1.3$.

In regime III, $l_{p,o}<r<\xi_{ten}(k)$, chainlike statistics of $l_{p,o}$ is expected. Here, we run into what seems to be a contradiction – chainlike statistics of Gaussian/SAW are expected to show a slope of $1.6<|m|<2$ for $I(q)$, but we observed $|m|<0.5$ in our intermediate-q regime. This issue is resolved in regime IV, $l_{p,o}$, $\xi_{ten}(k) < r < l_p(k)$, where the main-chain conformation can be visualized as an extended array of tension blobs of variable size similar to polyelectrolytes[63]. The extended conformation would predict a slope $|m|\approx1$, but with a varying MC density approaching the center of the MC reduces the scattering density resulting in a slope with $|m|<1$. Therefore, the interplay of $\xi_{ten}(k)$ and $l_{p,o}$ in regimes III and IV can resolve the peculiar intermediate q-regime. We applied a high tension profile, $\xi_{ten}(k)\approx l_{p,o}$, due to the absence of a chainlike statistic region at high-q, $q\sim q^*_s$. If the tension blobs for all k were much larger than the intrinsic persistence length, a regime with $1.6<|m|<2$ would have been observed. Unfortunately, the exact tension blob profile could not be ascertained.

On the largest length scale of regime V, $r>l_p(k)$, main-chain can be visualized as having chainlike statistics of these extended array of tension blobs, confirmed by the upturn in scattering intensity for $q<q^*_L$. Due to the short-range nature of SC-repulsion, a more local tension is expected compared to polyelectrolyte solutions. Instead, a better approximation would be a polyelectrolyte solution partially screened with salt ions leading to a electrostatic persistence length. In a similar manner, the tension is screened on a length

scale we define as the induced persistence length, $l_p(k)$. With reduced SC-repulsion near the ends, the size of the corresponding SC would be smaller, reducing the tension screening length. Therefore, we apply a persistence profile that approaches a maximum in the center of the MC. This qualitative feature is pertinent in another observation which will be in subsequent discussion. The SAW superblob model predicts $l_{p,app}/D \sim O(1)$. Although, the noise of our data prevents us from extracting a specific $l_p(k)$ profile, the MC scattering profile reveals an effective persistence length, $l_{p,eff} \approx 52.3$nm, and the overall scattering profile reveals a cross sectional length scale, $d_K \approx 30$nm. Taking the ratio, we show that $l_{p,eff}/d_K \approx 1.75 \sim O(1)$, confirming the SAW superblob model by Birshtein.
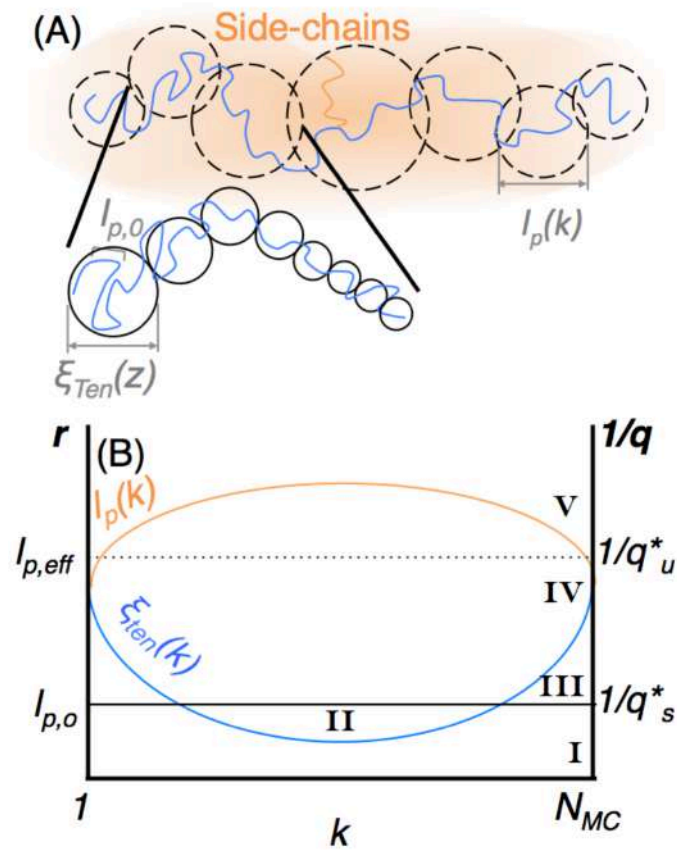
Figure 2.5. Tension blob model of bottlebrush polymers in solution. (A) The main-chain conformation can be characterized by an interplay of 3 length scales, the intrinsic persistence length, $l_{p,o}$, the position dependent tension blob, $\xi_{ten}(k)$, and the position dependent persistence length, $l_p(k)$. The side-chains are omitted in this schematic. (B) The end-to-end distance, r, of submolecules of the main-chain showing the length scale at each main-chain index, k. The interplay of $l_{p,o}$, $\xi_{ten}(k)$, and $l_p(k)$ to describe our results led to five regimes: I – $r<l_{p,o}$, II - $\xi_{ten}(k)<r<l_{p,o}$, III – $l_{p,o}<r<\xi_{ten}(k)$, IV - $\xi_{ten}(k)<r<l_p(k)$, V – $r>l_p(k)$.

Here, we emphasize that $l_{p,0}$ and $l_p(k)$ are mechanistically different and should not be added together, *i.e.*, $l_{p,app} \neq l_{p,0}+l_{p,ind}$ which can obscure important features, as done by Feuz, Subbotin, Nakamura, Zhang. If considered independently, the tension blob model can predict the MC conformation shown by our scattering data.

For the longest length scale, $r>l_p(k)$, approaching the Guinier plateau, linear polymers exhibit chain-like statistics (Gaussian/SAW). Indeed, the slope of roughly $|m|\approx2$ confirms the chain-like statistics at low-q. In Chapter 3, 460-dPS65 for $c=0.4\%$ shows a slope shallower than at $c=1.0\%$, although the noise prevents us from extracting a quantitative value. Thus, the semidilute interactions force the bottlebrush polymer to adopt a more compact conformation than at dilute conditions[47,48], which may favor a SAW, consistent with the SAW superblob model by Birshtein.

2.4.3 Calculation Details/Results

To understand the MC scattering profile, we employed an approach similar to the method employed by Dozier et al.[64] to approximate the scattering spectra of star polymers. They identified two q-regimes with scattering and approximated the $I(q)$ spectra as a sum of two primary contributing factors. This methodology has been used to approximate the scattering spectra for the overall bottlebrush polymers by Rathgeber et al.[39] and Bolisetty et al.[49,50] In a similar fashion, we approximate the MC profile by considering two q-regimes: rodlike behavior at high-q to approximate the stiff conformation for $r<l_{p,o}$, and Gaussian behavior at low-q with steps on the size of the $l_p(k)$ with total scattering of $N_{Ten}=N_{tot}/s_{p,o}$. The specific details of the calculations can be found in the Appendix.
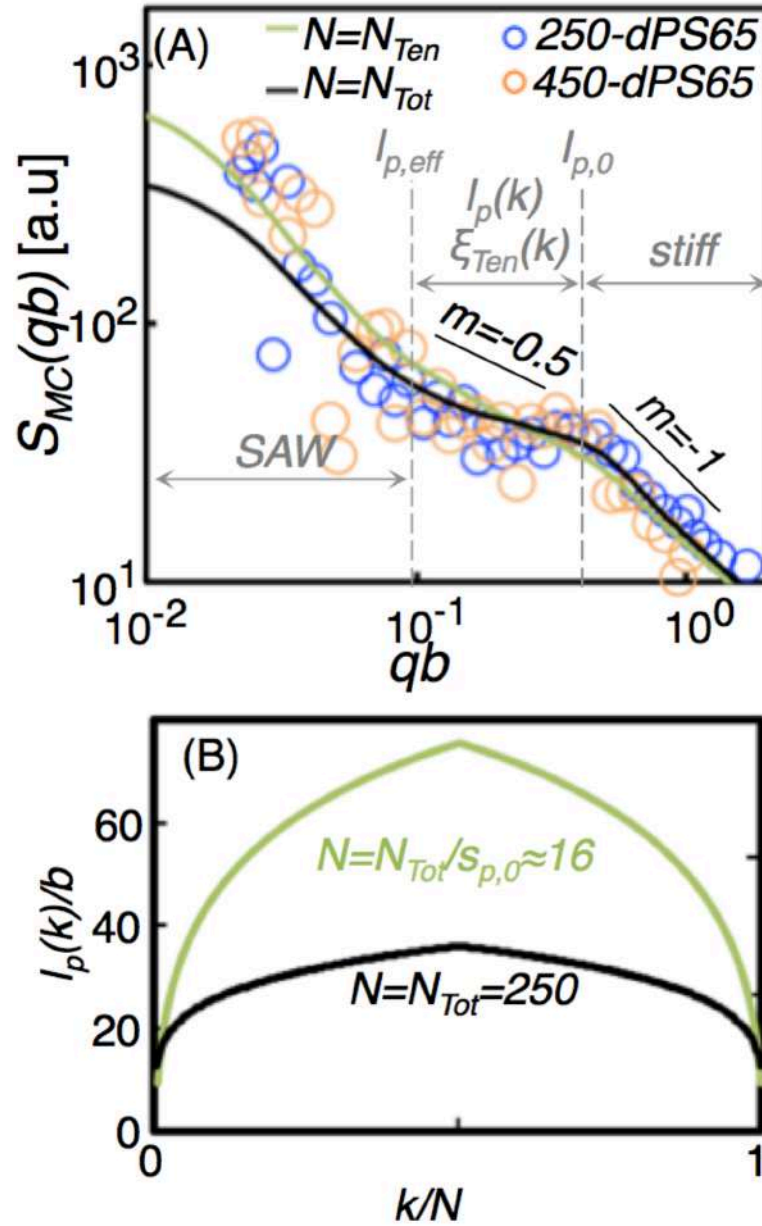
Figure 2.6. Approximating main-chain scattering with S(qb). (A) The calculated S(qb) approximating the main-chain through both models juxtaposed to 250-dPS65 and 450-dPS65 SANS result. Labeled on the graph are the length scales and behavior in q-space. To map $I(q) \rightarrow I(qb)$, b=5 Å. In addition, $S_{MC}(qb)$ for method 2 needed to by shifted by 1.8 as well. (C) The $l_p(k)$ used to calculate $S_{MC}(qb)$ in (B).

For a $l_p(k)$ profile, we look to simulation results from Hsu et al.[33–35,44,45] showing that a the local persistence length, defined $l_{p,local}(k) = l_b \left\langle \vec{a}_k \cdot \vec{R}_e / |\vec{a}_k|^2 \right\rangle$, can be fit to

$l_{p,local}(k) = l_b \alpha \left[k \left(N_{mc} - k \right) / N_{mc} \right]^{2\nu-1}$ for 0.3<k/N_{tot}<0.7. We applied this model to estimate

the $l_p(k)$ profile as the salient features from SC-repulsion are captured – symmetry about the midpoint of the MC, a monotonic increase of the induced persistence length from the MC ends, and a constant value in the central portion of the MC at the asymptotic limit. Their results of the overall brush dimensions, R_g and R_{CS}, showed agreement with predictions made by Birshtein et al.[18] with the overall persistence length being approximately $2R_{CS}$. Although not explicitly stated in their work, their results indicate the main-chain length required to reach the asymptotic limit of SAW of superblobs is $N_{MC,AL}$>50 superblobs. This result is contradictory to the popular understanding in literature that the asymptotic limit for the main-chain length is N_{MC}>>N_{SC}, severely underestimating the lower bound of main-chain length. Experimental efforts also underestimate the lower bound with the condition[28,30,41,42] DP_{MC}≈10-120. With respect to the persistence length, the condition that has been used in literature for the asymptotic limit for MC length has been L/l_{app}>1, where L is the fully extended contour length, two orders of magnitude shorter than the lengths observed by Hsu. We apply $l_{p,local}(k)$ to estimate the persistence length profile only at the asymptotic limit, $l_{p,aL}(k)$. For $l_p(k)$ profiles of N_{MC}<$N_{MC,AL}$, we propose that $l_p(i)=l_{p,AL}(i)$ for $i=1:N_{MC}/2$ and applying symmetry about the midpoint, can get the full k profile. To understand the proposition, we visualize a SC grafted at the ends of the MC. The degree of crowding is independent of the MC length. The SC crowding builds up with distance away from the end MC unit, independent of the number of MC units to the $k=N_{MC}/2$. Therefore, the crowding buildup is determined by the outer portions of the $l_{p,AL}(k)$.

The calculated $S(qb)$ can be seen Fig. 2.6A (green) with the $l_p(k)$ profile in Fig 2.6B. We chose the parameters such that the minimum $l_p(k)$ is $l_{p,o}$, the chain cannot be more flexible than the intrinsic persistence length, and the average $l_p(k)$≈$l_{p,eff}$. The calculations show excellent agreement with the experimental data for $q<q_o$.

In addition, we tested to see if the scattering profile of the overall bottlebrush could be obtained by the corresponding MC decorated with SCs at every MC monomer. Therefore, we expanded our calculation to consider scattering contributions from (1) MC to

MC, (2) SC to MC, (3) SC to same SC, (4) and SC to a different SC. With a SC grafted to every MC monomer, the MC could no longer be subdivided into segments of $s_{p,o}$ which required re-indexing of the MC units to DP_{MC} of the PNB of our samples. A $l_p(k)$ spanning the entire DP_{MC} range was chosen to with a similar R_g as the array of tension blobs. The $S_{MC}(qb)$ approximating the MC can be found in Fig 2.6A and B (black). Using this approach, we calculated the $S_{Overall}(qb)$ with side-chains grafted onto every MC monomer. We applied Gaussian statistics on the side-chains as a brutal approximation, allowing us to recover a general profile and refined the approximation by an increase in the SC Kuhn step to account for the extended conformation. The results of $S_{MC}(qb)$ for DP_{MC}=250 and 450 and $S_{Overall}(qb)$ with DP_{MC}=330 and 1190 can be seen in Figure 2.7A. Juxtaposed to the $S(qb)$ calculations are the $I(q)$ results mapped onto qb-space by b=2.5Å with the corresponding DP_{MC}. The $l_p(k)/b$ used for each calculation can be found in Fig. 2.7A. With MC length, we see that the calculations can accurately capture the experimental results in the q-range for $q<q_0$. Most notably for $S_{MC}(qb)$, the intermediate q-regime with $|m|<0.5$ has been captured showing that an interplay of multiple length scales can produce the sublinear profile. Without a built-in wormlike treatment, the overall scattering has been successfully recovered, even the Porod scattering region of the overall brush of roughly $|m|$=1.3, significant evidence which has been used to corroborate the wormlike chain hypothesis. In accord with experimental results, we note that the $S_{MC}(qb)$ does not have a q-range with $|m|$=1.3, showing the MC behavior is masked by the signal dominating SCs. Thus, we show that inferring MC conformation from the overall scattering data can lead to misleading conclusions, such as the wormlike chain hypothesis.
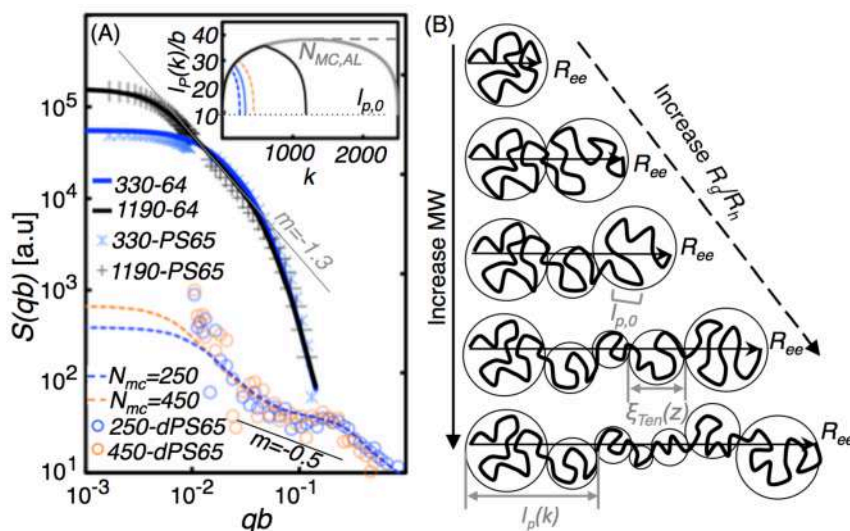
Figure 2.7. Main-chain length dependence on conformation. (A) A comparison of calculated main-chain and overall $S(qb)$ to experimental results for main-chain and overall $I(q)$ for multiple main-chain lengths. Slopes of $|m|=1.3$ and $|m|=0.5$ are included to guide the eye in the q-range of interest. Mapping $I(q) \rightarrow I(qb)$ required $b=2.5$Å. In the inset, the local persistence length profile, $l_p(k)$, as described by our method 2 showing the profile for $N_{MC}=250$ (blue, dotted), 330 (light blue), 450 (orange), and 1190 (black). The profile at the asymptotic limit, $N_{MC}=N_{MC,AL}$ (gray), and $N_{MC}>N_{MC,AL}$ (dotted gray) are also included. (B) Schematic of conformation dependence on the main-chain length through the interplay of various length scales described by the tension blob model.

2.4.4 Shape anisometry of bottlebrush polymers

2.4.4.1 Rg/Rh and main-chain length dependence

The MC length dependent persistence length would explain another observation, which is that R_g/R_h, a common method of quantifying anisometry, increases as the main-chain gets longer —opposite to predictions by Denesyuk and expectations for a wormlike chain (dsDNA) (Figure 2.8). This observation is consistent with the main chain being relatively flexible near its ends, which is dominant for short main-chains (flexibility favors isometric shape). An addition of a stiff segment in the center will increase the anisometry, reflected in an increase in R_g/R_h. As can be seen in Figure 2.7A (inset) and schematically in 2.7B, each increase in main-chain molecular weight would be accessing additional central portion of the main-chain, which corresponds to the most extended unit from having a higher degree of crowding than the rest of the chain. Although not explicitly discussed in their work (and their discussion contradict their results), the main-chain length trend was observed by Norisuye group[28,29] for PS_{MC}-PS_{SC} system. They show the same qualitative

trend of increasing R_g/R_h with main-chain length, but the magnitude was much higher. With a smaller graft spacing (2 carbons, 0.25 nm vs 5 carbons, 0.6nm), $l_{p,0}$ is expected to be much higher and side-chains repulsion leads to higher $l_p(k)$, consistent with the higher R_g/R_h values. The largest molecules in the PS-PS65 series seems to be at or very close to the asymptotic limit for the main-chain, but their PS-PS115 series clearly shows the main-chain is still too short. Recently, simulations by Dutta et al.[46] showed that the shape anisometry (sphericity and prolateness) is SC length dependent and long MCs were required to reach an asymptotic limit, consistent with our experimental data. Their reported R_g/R_h for $PNB_{MC}-PLA_{SC}$ show excellent agreement with our results.
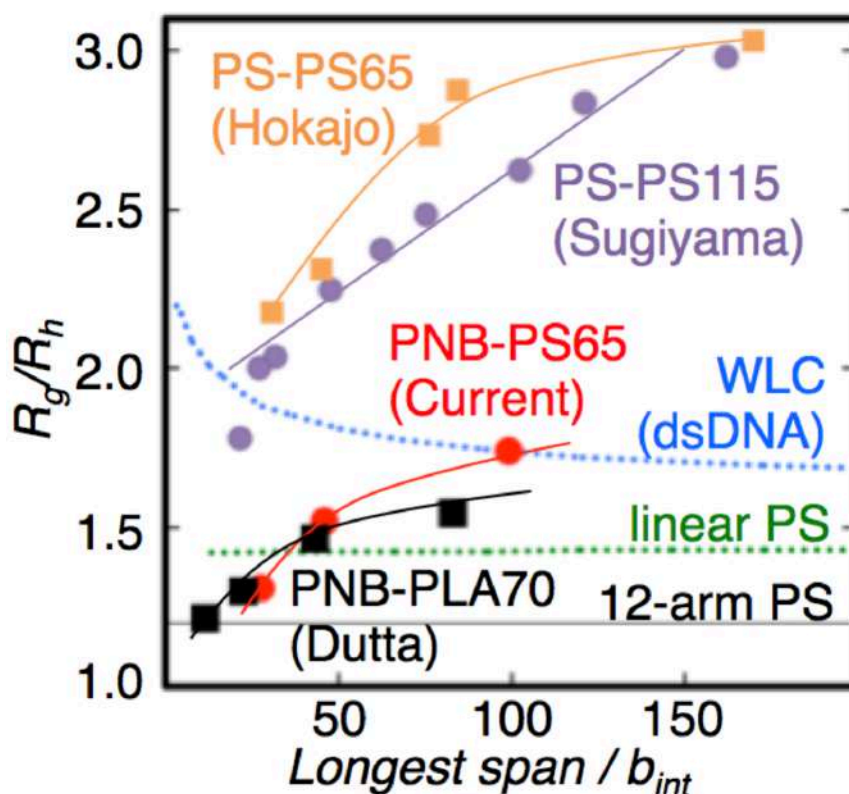
Figure 2.8. R_g/R_h comparisons of BBPs to other topological systems: linear (dotted green), 12-arm star (black) and wormlike chain represented by dsDNA (dotted blue). 'Longest span' represents the fully extended contour length of the polymer for linear and WLC and of the arms of the star and the fully extended contour length for bottlebrushes. Results from Hokajo and Sugiyama and Dutta are also included. The lines are to guide the eye and not for parametric fitting.

2.4.4.2   Lower c* than expected

Our observation of lower overlap concentrations also confirms the anisometric shape observed by our other experiments and consistent with our conceptual model. We observed the substantially lower overlap concentration than the c^*_{iso}. For particles with $L \gg R_g$, interactions begin at $\sim R_{CS}L^2$, much larger than predicted by $\sim R_g^3$. Three distinct length scales, different than the $R_{g,isotropic}$, can be ascertained from SAXS/SLS patterns from dilute conditions. The largest length scale, from d_H, showed main-chain length dependence whereas the middle and short length scales, d_K and d_S, respectively, showed no dependence on the main-chain length. Hence, d_K and d_S are non-contributors and d_H is the biggest contributor to the anisometry. We assign $d_H \sim L$ and $d_K = D_{CS}$ and calculate the concentration which correspond to $\sim d_H^2 (d_K/2)$, the onset of semidilute interactions. As can be seen in Table 2.4, we show that the ratio of $R_{g,zimm}^3/d_H^2(d_K/2)$ is comparable to the suppression in overlap concentration assuming isometric shapo, c^*_{SLS}/c^*_{iso}.

2.4.4.3   Origins of R_g

In addition, the d_H and d_K was used to calculate a R_g for a cylinder, $R_{g,cyl}^2 = R_{CS}^2/2 + L^2/12$, using $d_H \sim L$ and $d_K = D_{CS}$. Here, we are not validating a rigid cylinder as a way to approximate the shape of bottlebrush polymers. Instead, we use it as a reference anisometric shape to estimate if the observed length scales, d_H and d_K, are consistent with a shape increasing in anisometry with MC length. The results are listed in Table 2.4. For all three MC lengths of the overall brush, the $R_{g,cyl}$ values show good agreement with the observed R_g ($R_g/R_{g,cyl} > 0.8$). Therefore, we show R_g cannot fully characterize a bottlebrush polymer shape and size since it is an interplay of a long and short dimension. In addition, $R_g/R_{g,cyl}$ approaches unity with increasing MC length, supporting our assessment from R_g/R_h analysis that the bottlebrush becomes increasingly anisometric with MC length, that is, the bottlebrush becomes 'stiffer' as the main-chain becomes longer.

Table 2.4. Summary of overlap concentration and length scales.

Sample	c^*_{iso} % (wt)	c^*_{SLS}/c^*_{iso}	$R_g^3/10^4$ [nm³]	$d_H^2d_K/2/10^4$ [nm³]	$2R_g^3/d_H^2d_K$	$R_{g,cyl}$ [nm]	$R_g/R_{g,cyl}$	R_g/R_h
330-PS65	1.7	0.15-0.30	3.93	27.0	0.15	39.3	0.87	1.3
550-PS65	1.1	0.09-0.23	12.5	51.3	0.24	54.5	0.92	1.5
1190-PS65	0.6	0.17-0.42	42.2	94.5	0.44	73.2	1.02	1.7

2.4.5   Not a wormlike chain with $l_{p,app}/D>>O(1)$

Lastly, we compare our results and calculations to other works in literature and begin to discriminate amongst other popular, mutually exclusive, models (Figure 2.9). First, the rod form factor for a rod shows no internal features present in our experimental and calculation results and can be eliminated as a possible model. Next, we compare our results to the form factor adapted from Paturej et al.[51] in the melt. Their results showed an excellent resemblance to a semiflexible chain. Therefore, the difference between their $S_{MC}(qb)$ in the melt compared to our $S_{MC}(qb)$ and $I(q)$ in solution shows that a semiflexible chain cannot adequately approximate a bottlebrush polymers in solution and that the behavior of bottlebrushes in solution and melt behavior are significantly different. The arrow in Figure 2.9 represents the primary difference in solution compared to the melt, which can be attributed to the excluded volume interactions that are screened in the melt. With that view, the additional tension forces the random-walk behavior to lower-q while the position of $l_{p,o}$ remains unchanged. As widely accepted, we show the overall persistence length of the main-chain is significantly amplified. However, there exists a discussion in literature inquiring about the extent to which the persistence length increases with WLC models predicting $l_{p,app}/D>>O(1)$ and SAW of superblobs model and tension blob model both predicting $l_{p,app}/D\sim O(1)$. With both main-chain scattering and overall scattering data, we can directly compare length scales, and more specifically, we can verify the highly controversial value of $l_{p,app}/D$. Our results show that the ratio of the cross sectional length scale of the overall bottlebrush, $d_K\sim 2\pi/q^*_K$, and the $l_{p,eff}\sim 2\pi/q^*_u$, is roughly $l_{p,eff}/D=q^*_K/q^*_u=1.75\sim O(1)$ verifying Birshtein's SAW superblob model and Paturej-Rubinstein tension blob model.

When we input a much higher $l_p(k)$ such that $l_{p,eff}/D \approx 4$ to approximate a WLC model (orange in Figure 2.8), the intermediate-q regime extends much lower than our experimental data. Thus, for synthetically accessible bottlebrush polymers, the SC-repulsion leads to $l_{p,app}/D \approx O(1)$ and excludes $l_{p,app}/D \gg 1$ as possible models. Finally, we show that a constant $l_{p,eff}$ can approximate the main-chain $I(q)$ very well (green); however, it can be dismissed on account of our increasing R_g/R_h with MC length observation. If $l_{p,eff}$ is a constant with main-chain length, we would expect a R_g/R_h to mimic that of the dsDNA, but the opposite behavior is observed.
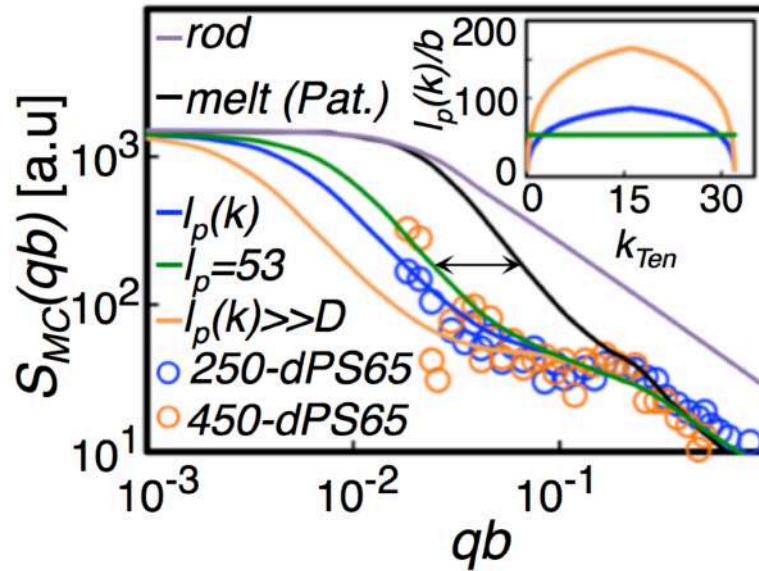
Figure 2.9. $S(qb)$ for various systems. (A) The main-chain $S(qb)$ calculations for hypothesized models for bottlebrushes found in literature. The exact persistence profiles inputted into the calculations are shown in the inset.

2.4.6 Revisiting Literature

Our work shows the wormlike-chain/cylinder to be a poor approximation for bottlebrush systems with a high degree of SC-repulsion. With many theoretical/experimental efforts predicting a wormlike behavior, it is important to understand where the source of error may be coming from. First, as discussed earlier, two independent modes of stiffness were convoluted into a single stiffness parameter, assumed to be a constant throughout the chain or considered negligible. In doing so, important

features, such as the mechanism of tension, were obscured. In addition, a common practice of theoretical works predicting a wormlike chain behavior is their use of relationships predicted for a wormlike chain. Authors Fredrickson, Nakamura, and Subbotin all invoke a scaling relationship of bending for wormlike chain with Kuhn length, l_K. This assumes a constant Kuhn length which is likely the source of error. Birshtein did not invoke this relationship as SC repulsion (the mechanism for main-chain extension) is reduced when side-chains redistribute during the bending of a bottlebrush system. Thus, as the side-chain reorders, the free energy cost of bending is reduced in that respective direction, and the free energy of bending a cylinder should not be used for bends with long contours. Similarly, Denesyuk had used other relationships for wormlike chains to conclude a wormlike chain behavior. Thus, these approaches had a wormlike chain built into their work.

Likewise, experimental approaches have committed a similar fallacy. The criteria for confirming wormlike chain/cylinder behavior was (1) the quality of fits with many adjustable parameters to experimental results and (2) values consistent with theoretical predictions made by theorists described in the previous paragraph. If a wormlike chain/cylinder models exclusively fit the data, then this approach could be a proper method used to ascertain wormlike behavior. However, Pesek et al., Wataoka et al., and Rathgeber et al. showed scattering profiles could be fit nonexclusively to many different models and aphysical behavior. Works by Norisuye group showed substantial variation in fit parameters with the addition of an additional set of polymers with different side-chain length, also demonstrating the nonexclusive nature of fits to experimental data.

More recent works, [Hsu, Paturej, Dutta] and pioneering work by Birshtein did not invoke any wormlike chain assumptions/relationships and concluded $l_{p,app}/D \sim O(1)$, consistent with our observations.

2.5   Summary

We acquired scattering profiles for bottlebrush polymers with hydrogenous side-chains (dilute conditions) and analogous bottlebrush polymers with deuterated side-chains (slightly semidilute), isolating the scattering to the main-chain only. From the observed features, we show that a wormlike chain model with a single stiffness parameter, the induced persistence length, with $l_{p,app}/D>>O(1)$ cannot adequately describe the main-chain scattering results obtained in this work. Instead, we show that the interplay of a few length scales, modified tension blob model by Paturej et al., can accurately predict the scattering profile. In addition, the cross sectional length scale from the overall scattering profile and persistence length profile from the MC scattering profile enabled us to verify the value of the highly controversial $l_{p,app}/D$ value. Our results indicate $l_{p,app}/D=1.75\sim O(1)$, confirming a feature predicted by the SAW supreblobs model pioneered by Birshtein and the tension blob model by Paturej.

One significant feature of our proposed tension blob model is the *k*-dependence in both the tension blob size and the persistence length. We observed the anisometry increases with MC length, the opposite of wormlike chains (dsDNA), a feature that *k*-dependence persistence length accurately predicts. In doing so, we show that a fractal, or a self-similar treatment, may be a poor approximation of bottlebrush conformation as the behavior at the end of the BBP is vastly different than in the central portion of the BBP.

2.6   Supporting Information

2.6.1   S(qb) calculations

We begin by discussing the calculations of the main-chain $S_{MC}(qb)$. We employed two approaches which gave successful approximation of the *I(q)* vs. *q* for the main-chain for $q<q_O$ shown in Figure 2.6. Similar to the approach by Dozier et al., Rathgeber et al., and Bolisetty et al., we identify scattering regimes and approximate the $S_{MC}(qb)$ from two different contributions, Gaussian behavior (allowing for calculations without orientation

effects) of arrays of tension blobs with step size $l_p(k)$ at low-q and stiff behavior of persistence segments at high-q

$$S_{MC}(qb) = S_{Gauss}(qb, l_p(k)) + S_{Rod}(qb, s_{p,o}),$$ (2.1)

where

$$S_{Gauss}(qb) = \frac{1}{N_{sp}} \sum_{i=1}^{N_{sp}} \sum_{j=1}^{N_{sp}} \prod_{k=i}^{j} \exp\left(\frac{-(qb)^2 (l_p(k)/b)^2 (1)^k}{6}\right)$$

$$S_{Rod}(qb) = \frac{1}{s_{p,0}} \sum_{i=1}^{s_{p,0}} \sum_{j=1}^{s_{p,0}} \left(\frac{\sin(qb|i-j|)}{qb|i-j|}\right)$$ (2.2)

where $N_{sp}=N_{MC}/s_{p,0}$ is the number of intrinsic persistence segments in the main-chain. Unfortunately, the double sum in $S_{Gauss}(qb)$ cannot consider the internal structure for $r<l_p(k)$. By re-indexing i and j to represent a subsegment, the profile was obtained for higher-q, allowing for a proper summation. Within the intrinsic persistence segment, $s_{p,o}$, the conformation was approximated as a rod, consistent with our observation that $1<|m|<1.5$ (for $I(q)\sim q^{-m}$). With the addition of side-chains from PNB, the intrinsic persistence step, $s_{p,o}$, is expected to be even bigger than for bare PNB ($s_{p,PNB}=6$) (for PHEMA, Zhang observed roughly 3x increase in intrinsic persistence length due to side-chains). Our main-chain scattering profile shows a stiff length scale at $d_S=9.4$nm. Using $l_{p,o}=d_S$, we use $s_{p,o}=16$, and $N_{sp}=N_{MC}/s_{p,o}$.

Paturej et al. showed local flexibility in melts showing thermal fluctuations beyond the intrinsic persistence length, defined as the tension blob. When the excluded volume interactions are not screened these rodlike segments are under significant tension, preventing freely adopting a Gaussian/SAW conformation at large length scales. Instead, the Gaussian/SAW of $s_{p,0}$ segments are aligned by the tension blobs which begin to lose correlation at the induced persistence $l_p(k)$, where $l_p(k)>l_{p,0}$ for all k since the chain cannot be more flexible than the intrinsic persistence length. Here, k represents the k-th persistence segment of the main-chain. Hsu, Elli, Schafer showed persistence length to

vary with the main-chain index, k, such that $l_p(k) \approx \alpha l_b \left[k(N-k)/N \right]^{2\nu-1}$. We used this profile for the asymptotic, $l_{p,AL}(k)$, asymptotic main-chain length, $N=N_{MC,AL}$, with a vertical offset such that $l_p(1)=l_{p,NMC,AL}=l_{p,o}$. Our bottlebrushes are not yet in the asymptotic limit $l_p(k)$ profile that was obtained by using $l_p(i)=l_{p,AL}(i)$ for $i=1:N_{MC}/2$ and applying symmetry for the remainder of k. Although a constant $l_p(k)=l_p$ can recover the desired $I(q)$ profile, it fails to explain the main-chain length dependence observed in our other results and can be omitted as an appropriate model. Even so, $l_p>s_{p,0}$ was required for a constant l_p to capture the $I(q)$ profile, discriminating the wormlike-chain model on the basis of requiring a separation of two length scales. Because the indexing represents different units for each term, main-chain monomers for $S_{Rod}(qb,s_{p,0})$ vs. intrinsic persistence segments for $S_{Gauss}(qb,l_p(k))$, the magnitude must be normalized to the condition $S_{Ten}(0)/S_{l_{p,0}}(0) = N_{Ten}$. In Figure 2.6, the results for $s_{p,0}=16$, $N_{Ten}=250/16$ and $l_p(k)$ profile ($\alpha=50$, $N_{MC,AL}=50$) is in green.

Although we were able to approximate the main-chain $I(q)$, we aimed to consistently recover $I(q)$ for the overall bottlebrush as well. We found it necessary for the main-chain indexing to be consistent throughout the entire qb-range to account for a SC at each MC monomer, not each persistence segment. We chose a Gaussian chain of $N=N_{PNB}=250$ with approximately same R_g as by the system of tension blobs by readjusting the $l_p(k)$ to that observed in black in Figure 2.6 in black. As before, $S(qb)$ was approximated from two different contributions, Gaussian at low-q and a rod at high-q

$$S_{MC}(qb) = \sum_{i=1}^{N_{MC}} \sum_{j=1}^{N_{MC}} \left(S_{i_G j_G}(qb, l_p(k)) + S_{i_R j_R}(qb) \right), \qquad (2.3)$$

where

$$S_{i_G j_G}(qb, l_p(k)) = \frac{1}{N_{MC}} \exp\left(\frac{-(qb)^2 \left(l_p(k)/b\right)^2 |i-j|}{6}\right) = \frac{1}{N_{MC}} \prod_{k=i}^{j} \exp\left(\frac{-(qb)^2 \left(l_p(k)/b\right)^2 (1)^k}{6}\right) ,$$

$$S_{i_R j_R}(qb) = \sum_{|i-j| < s_{p,0}} \frac{\sin\left(qb|i-j|\right)}{qb|i-j|}$$

(2.4)

where l_p is the induced persistence length by side-chain repulsion. We note that $S_{i_R j_R}(qb, l_p)$ is only calculated if $|i$-$j| < s_{p,o}$. Here, the crossover between low-q regime and the high-q regime is not handled explicitly. Since our aim is to discriminate amongst accepted mutually exclusive models, a quantitative modeling and fitting go beyond the scope of this work.

To properly capture the architectural parameters of the chemical structure and PNB$_{MC}$-PS$_{SC}$ used in this work, modifications must be made to the $S_{MC}(qb)$. With 100% grafting density for PNB, multiple side-chains are grafted per intrinsic persistence step for bare PNB ($s_{p,PNB}$=6). With the addition of side-chains from PNB, the intrinsic persistence step, $s_{p,0}$, is expected to be even bigger (for PHEMA, Zhang observed roughly 3x increase in intrinsic persistence length due to side-chains). Therefore, at high-q, the $S_{MC}(qb)$ is dominated by a rod-like scattering from i and j pairs shorter than the intrinsic persistence segment satisfying the condition $|i$-$j| < s_{p,o}$.

Unfortunately, due to the monomer length mismatch between our main-chain (PNB) and side-chain (PS), i and j must be normalized to give equal contribution to the intensity and monomer step size. After normalization, δ_{MC}=0.6 for PNB (monomer length of 0.6nm) main-chain, we obtain the final expression used

$$\delta_{MC}S_{i_G j_G}(qb,l_p(k)) = \frac{\delta_{MC}}{N_{MC}} \prod_{k=i}^{j} \exp\left(\frac{-(qb)^2 \left(l_p(k)/b\right)^2 \delta_{MC}}{6}\right),$$

$$\delta_{MC}S_{i_R j_R}(qb) = \sum_{|i-j|<s_{p,0}} \frac{\sin\left(qb|i-j|\delta_{MC}\right)}{qb|i-j|}$$

(2.5)

Next, we incorporated side-chains at every main-chain monomer approximated by Gaussians profile and verify if our overall $I(q)$ can be recovered by side-chains grafted to a main-chain described by $S_{MC}(qb)$. To account for the underestimation of the Gaussian treatment of the side-chains, we use an increased persistence length of the side-chains. The overall structure factor $S_{Overall}(qb)$ is the sum of four different contributions from the different locations of monomers i and j,

$$S_{Overall}(qb,l_p(k),l_{p,SC}) =$$
$$\sum_i \sum_j \Big(\delta_{MC}S_{i_M j_M}(qb,l_p(k),\delta_{MC})$$
$$+ \delta_{SC}S_{i_{S1} j_{S1}}(qb,l_{p,SC},\delta_{SC})$$
$$+ S_{i_M j_S}(qb,l_p(k),l_{p,SC},\delta_{MC},\delta_{SC})$$
$$+ S_{i_{S1} j_{S2}}(qb,l_p(k),l_{p,SC},\delta_{MC},\delta_{SC})\Big)$$

(2.6)

where $S_{i_M j_M}(qb,l_p(k))$ is the contribution from monomer i and j on the main-chain, $S_{i_{S1} j_{S1}}(qb,l_{p,SC})$ is the contribution form monomer i and j on the same side-chain, $S_{i_M j_S}(qb,l_p(k),l_{p,SC})$ is the contribution monomer i and j on a side-chain and main-chain, and $S_{i_{S1} j_{S2}}(qb,l_p(k),l_{p,SC})$ is the contribution of monomer i and j on different side-chains spaced by the main-chain summarized in Figure 2.10.
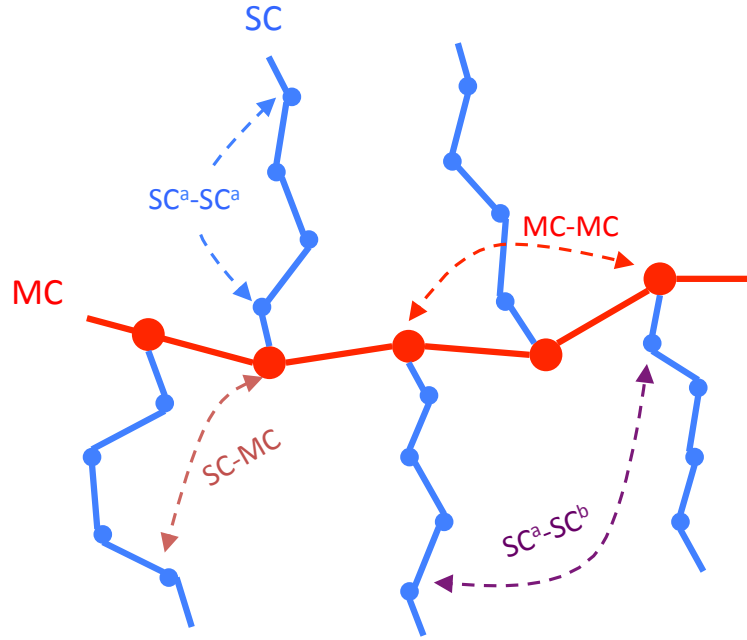
Figure 2.10. Schematic of the four different $S(qb)$ contributions: side-chain to same side-chain (orange), side-chain to different side-chain (light blue), main-chain to side-chain (black), and main-chain to main-chain (green).

For monomers i and j on the main-chain, the profile can be described by

$$S_{i_M j_M}(qb, l_p(k)) = \delta_{MC} \prod_{k=i}^{j} \exp\left(\frac{-(qb)^2 \left(l_p(k)/b\right)^2 \delta_{MC}}{6}\right) + \sum_{|i-j|<s_{p,0}} \frac{\sin\left(qb|i-j|\delta_{MC}\right)}{qb|i-j|\delta_{MC}}, \qquad (2.7)$$

as described before.

Likewise, the contribution from the side-chain to the same side-chain is a Gaussian with persistence length $l_{p,SC}$

$$S_{i_{S1} j_{S1}}(qb, l_p(k)) = \delta_{SC} \exp\left(\frac{-(qb)^2 \left(l_{p,SC}/b\right)^2 |i-j|\delta_{SC}}{6}\right), \qquad (2.8)$$

where δ_{SC}=0.25 is the for PS (monomer length of 0.25nm). The next contribution to consider is from a main-chain monomer i to a side-chain monomer j (and vice versa). The

Gaussian treatment of side-chains and main-chain allows the side-chain to main-chain contribution to be the product of two Gaussians – (1) SC-SC from monomer i on the side-chain to the SC-MC junction monomer m with $l_{p,SC}$ and (2) MC-MC from monomer m to monomer j on the MC with $l_p(k)$

$$S_{i_M j_S}(qb, l_p(k), l_{p,SC}, \delta_{SC}, \delta_{MC}) = \left(1 - f_{MC}(\delta_{MC} - 1)\right) S_{i_M m_M}(qb, l_p(k))\left(1 - f_{SC}(\delta_{SC} - 1)\right) S_{m_S j_S}(qb, l_p$$

(2.9)

where $(1 - f_{MC}(\delta_{MC} - 1))$ and $(1 - f_{SC}(\delta_{SC} - 1))$ account for the index differences in the MC and SC respectively with f_{MC} and f_{SC} representing the fraction of monomers between i and j that are on the MC and SC respectively. The final contribution comes from monomer i on side-chain to monomer j and a different side-chain which reduces to a product of three terms with the Gaussian treatment – (1) SC1-SC1 from monomer i on side-chain no. 1 to the SC-MC junction monomer m with lp,SC, (2) MC-MC from the SC1-MC junction monomer m to the SC2-MC junction monomer n with $l_p(k)$, and (3) SC2-SC2 from SC2-MC junction monomer n to monomer j on side-chain no. 2 with lp,SC

$$S_{i_{S1} j_{S2}}(qb, l_p(k), l_{p,SC}, \delta_{SC}, \delta_{MC}) =$$
$$\left(1 - f_{MC}(\delta_{MC} - 1)\right) S_{n_M m_M}(qb, l_p(k))\left(1 - f_{SC}(\delta_{SC} - 1)\right) S_{i_{S1} n_{S1}}(qb, l_{p,SC}) S_{m_{S2} j_{S2}}(qb, l_{p,SC})$$

(2.10)

In addition, the neutron scattering power is not identical between our main-chain (PNB+linker=27 hydrogens/mon) and side-chains (PS=8 hydrogens/mon). However, this hydrogen count is of the molecular DP. As treated before, the hydrogen count must also be for the monomer index for a contribution of 11.25hydrogen/index and 8 hydrogen/index for the main-chain and side-chain respectively. With contrast matched deuterated PS and

solvent showing identical scattering length density, the total scattering power is weighted by the square of the number of Hydrogens in each scattering unit. Therefore, to properly compare to SANS data, an additional each contribution must be weighted by the scattering intensity offered by the Hydrogen content.

2.6.2   Zimm plots
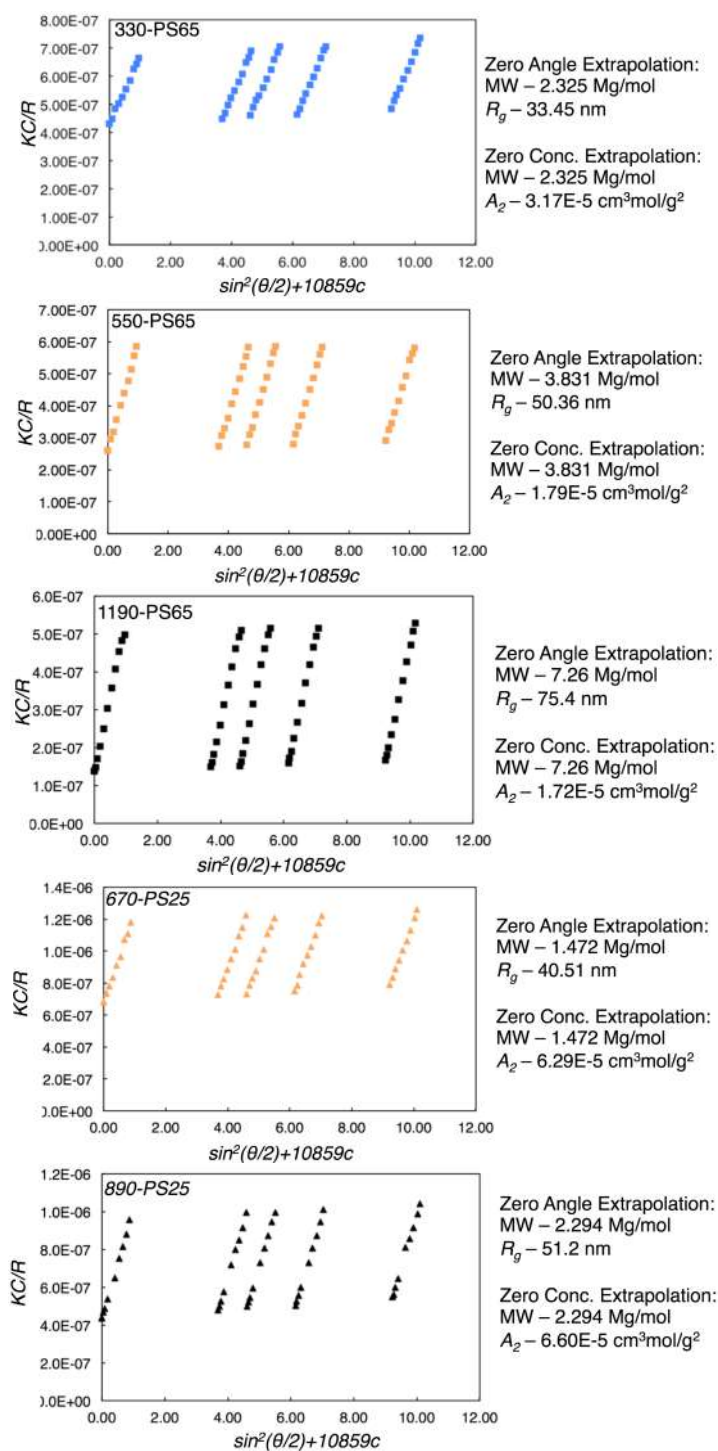
Figure 2.11. Zimm plots. Zimm plots for 330-PS65, 550-PS65, 1190-PS65, 670-PS25, and 890-PS25.

Chapter 3

BROADER SCOPE OF BOTTLEBRUSH ARCHITECTURE – EFFECT OF SIDE-CHAIN LENGTH, SOLVENT QUALITY, AND CONCENTRATION

3   Introduction

In this chapter, we shift our focus to the conformational behavior deviating from bottlebrushes with PS65 (and dPS65) side-chains through changing parameters such as the solvent quality, side-chain length, and solution concentrations. Prior works in literature under these conditions has been reviewed in detail in Chapter 1. Here, we will briefly summarize the results pertaining to θ solvent and/or side-chain dependence on the conformation of the main-chain and the effects of concentration while highlighting unanswered questions, discrepancies, and/or contradictions in literature. In light of the vacancy in understanding in literature, we share our results and discuss the new insights that could fill the gaps.

3.1   Literature Overview

3.1.1   *Complexities from branching – side-chain dependence*

With SC repulsion leading to an extension of the main-chain, significant efforts have been made to understand the interplay between side-chain and main-chains. With the underlying theory predicting stiffening, the following scaling relationship has been invoked $l_p \sim N_{SC}{}^{\alpha}$. Table 3.1 summarizes the scaling relationship that has been obtained from theory, simulation, and experimentalists for good solvent conditions. We see that $0 < \alpha < 2$, an expansive range predicting significant effect of side-chain length to complete side-chain independence. Here, we want to make a special note of work by the Norisuye[28,29] group studying PS_{MC}-PS_{SC} systems. With $N_{SC} < 65$, they showed that their persistence length results could be fitted to $\alpha = 1$. Surprisingly, with an addition of another side-chain length into their analysis, $N_{SC} = 113$, they showed that their results for $N_{SC} < 113$ now fit to $\alpha = 2$.

Table 3.1. Summary of scaling exponent, α, for $l_k \sim N_{SC}{}^{\alpha}$, ascribed model, and methodology in literature.

Author	α	Ascribed Model	Method
Panyukov et al. (2009)		Tension blobs	Theory
Birshtein et al. (1987)	49/75=0.65	SAW super blobs	Theory
Feuz et al. (2005)	1.82	WLC	Theory
Fredrickson (1993)	15/8=1.875	WLC	Theory
Subbotin et al. (2000)	2	WLC	Theory
Nakamura et al. (2001)	2	WLC	Theory
Hokajo et al. (2001)	1	WLC	Experiment
Sugiyama et al (2008)	2	WLC	Experiment
Rathgeber et al. (2005)	0	WLC	Experiment
Zhang et al. (2006)	1.79	WLC	Experiment
Saariaho et al. (1998)	0.69-0.71		Simulation
Hsu et al. (2011)	0.525	SAW super blobs	Simulation

3.1.2   Complexities from branching – solvent quality

Even in θ solvent, the inherent semidilute regime of bottlebrush polymers (as discussed in Chapter 2) results in 2- and 3- body excluded volume interactions, similar to that of star polymers[17,18]. However, the architecture driven 2-body interaction is an intramolecular interaction, not intermolecular, brush-brush interaction. Work by Terao[26,27,65], Hokajo[28], and Sugiyama[29] showed that for BBP with N_{SC} up to 110, the θ point coincides with that of linear polymer of the side-chains.

Birshtein et al.[18] had predicted that even in θ solvent conditions for the bottlebrush, a SAW scaling exponent would be observed. They argued that due to the high concentration of monomers around the main-chain from the dense grafting of side-chains, excluded volume interactions are still present at the θ solvent conditions. Their prediction of SAW of superblob model was for both good and θ solvent conditions.

Likewise, Nakamura[24] predicted the identical scaling relationship ($l_{p,app} \sim N_{SC}{}^{2}$) for the overall brush for good and θ solvent conditions. However, unlike Birshtein, they predicted a wormlike chain behavior in both solvent conditions. With different theoretical approaches predicting the same solvent effects but on mutually exclusive behavioral models, simulations and experimental results are a necessity to discriminate the predicted models.

Simulations by Feuz et al.[36] showed significant solvent effects showing reduced scaling relationships for $l_{p,app}$, α=1.59 and 1.89 in θ and good solvent, respectively, and for $l_{p,app}$/D, α=1.01 and 1.11 in θ and good solvent, respectively. Although the good solvent (and long side-chains) shows good agreement with WLC as predicted by Fredrickson[19], the good θ solvent shows relationships much closer to the SAW of superblobs, the prediction made by Birshtein, demonstrating the substantial solvent effects on the overall brush conformation.

On the other hand, experiments by Zhang et al.[31] showed that $l_{p,app}$/D is more consistent with work by Fredrickson than Birshtein for both good and θ solvent conditions. Although, like Feuz, they showed different scaling relationship values for $l_{p,app}$ (α=1.69 for good solvent and 1.42 for θ solvent), their $l_{p,app}$/D>6.77 for all samples analyzed with N_{SC}=6-33. They also show that $l_{p,app}$/D is highly dependent on the side-chain length in both good and θ solvent, showed $l_{p,app}$/D approach 12 and 20 for good and θ solvent respectively for N_{SC}=33. In addition, they did not consider the main-chain length dependence on the brush behavior. With our new conclusion from Chapter 2, we understand the significant affects the main-chain length can have. Unfortunately, Zhang et al. did not use a systematically varying sample set. They analyzed a single brush for each side-chain length. The main-chain DPs vary unsystematically from N_{MC}=1000-4500. Although these side-chain lengths are very long, the transition to the brush limit has to be verified, which has yet to be done.

3.1.3 *From Wormlike chain to Random Chain*

In contrast to Feuz and Saariaho[37], Rathgeber[39] showed that the scattering patterns of PAMA$_{MC}$-PnBA$_{SC}$ could be fit to a constant persistence length for side-chain range N_{SC}=22-98. Therefore, with a decreasing $l_{p,app}$/D beginning with $l_{p,app}$/D$|_{Nsc=22}$=8, they showed that bottlebrushes transition from a wormlike chain to random chain with increasing side-chain length.

3.1.4   Complexities from branching – concentration effects

Borisov et al.[47] pioneered the theoretical approach through free energy minimization and predicted four concentration regimes with a dilute solution at the lowest concentration regime. Three semidilute regimes were predicted with increasing degree of overlap with concentration beginning with conformational deviations of the overall bottlebrush, then the local structure, and finally the overall behavior again.

Bolisetty et al.[49,50] observed a suppression in low-q scattering with concentration, in accord with observations by Zhang. Fits to the scattering profile using a PRISM integral theory led them to conclude the persistence length decreases (from $l_{p,app}$=17.5nm to 5.3nm) with increasing concentration (from c=4.0-0.2wt%). With a R_{CS}=5.0nm, $l_{p,app}/D$=1.75-0.53 within the concentration range tested. However, with lyotropic behavior observed[21,57–59], applying pioneering work by Onsager[22] to bottlebrushes[19] required $l_{p,app}/D$>3.34 for lyotropic conditions. Thus, the decreasing $l_{p,app}$ with concentration observed by Bolisetty and the existence of lyotropic phases are contradictory and motivate further studies.

Rathgeber et al. [40] showed formation of a lyotropic phase for a sample with fit parameters corresponding $l_{p,app}/D$=3.5 in dilute conditions, which exceeds the critical value of 3.34 as predicted by Onsager. However, if the observation of Bolisetty is applied, $l_{p,app}/D$ would fall below that of the critical value, and the formation of the lyotropic phase is no longer predicted. Despite the apparent contradiction, Rathgeber showed a lyotropic phase which disappears with increasing concentration due to the softening of the excluded volume interactions from side-chain interpenetration of neighboring bottlebrushes. They showed that when the concentration is increased such that the bottlebrush-bottlebrush distance is lower than the cross-sectional diameter, the interpenetration of the side-chain leads to softening of SC-repulsion effects. In addition to discrepancy between experiments and classical theory, we see contradictory results within the experimental frontier as well.

Recent work by Paturej et al.[48] of bottlebrushes in melt quantified the degree of interpenetration in bottlebrushes, showing five different concentration regimes starting

from dilute (Figure 3.1). With increasing concentration, the excluded volume interactions becomes progressively screened resulting in, from a SAW, to a RW of persistence steps, to RW of main-chain monomers, to RW of side-chains. In the melt, they showed the side-chains do not completely penetrate in accord with the highest concentration regime showing screening of side-chains from the same bottlebrush. Although the concentration dependence of the overall and local length scales follow the same qualitative trend for predictions by Borisov and results by Paturej, they do not agree on the mechanism of interaction for side-chains of neighboring bottlebrushes. Borisov predicts a SAW to RW transition (before side-chain interpenetration) due to impermeability of side-chains whereas Paturej et al. claims the side-chains screen the excluded volume interactions through side-chain penetration. Although the discrepancy seems minor, the net effect on the overall conformation can be severe. If Borisov's predictions are true, the compression of the side-chains results in a further extension of the main-chain where as the interpenetration predicted by Paturej would result in a softening of the main-chain extension. From lyotropic phase observations, Borisov's analysis seems more validated, but more experiments are required to say anything conclusive.
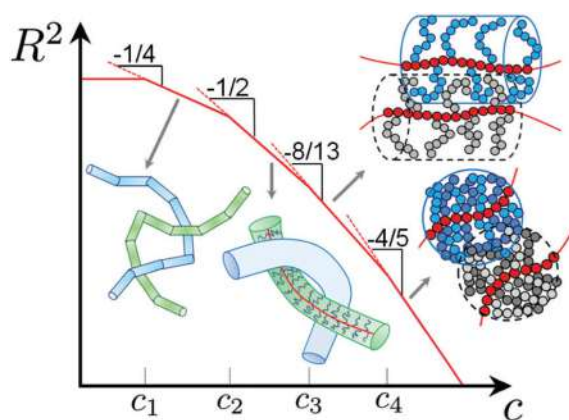
Figure 3.1 Concentration regimes for bottlebrush polymers. Adapted from Paturej et al.[48]

3.2   Experimental Section

The experimental conditions used to obtain the data in this chapter are detailed in Chapter 2.

3.3   Results

3.3.1   Effect of Solvent Quality - PS65 in θ Solvent

The scattering results for c=1.0% PS65 and dPS65 solutions in θ solvent, dCH 35°C, can be seen in Figure 3.2. Juxtaposed are the scattering profiles the samples in good solvent. The overall scattering in θ solvent shows similar scattering regimes, the Guinier, Porod, surface, and local scattering. The high-q profile for dPS65 could not be obtained, likely due do the low contrast as well as low concentration of scattering units in the sample. As was done in Chapter 2 for good solvent, the transition between regimes are identified through extremas in the Holtzer and Kratky plots, listed in Table 3.2

Table 3.2. Summary of SANS features and corresponding length scale obtained through the relationship $d=2\pi/q$ for BBPs with PS65 and dPS65 side-chains in θ Solvent.

	q^*_H [Å⁻¹]	d_H [nm]	q^*_K [Å⁻¹]	d_K [nm]	q^*_S [Å⁻¹]	d_S [nm]	q^*_{lp} [Å⁻¹]	l_p [nm]
330-PS65	0.007	89.7	0.027	23.3	0.094	6.7	-	-
550-PS65	0.0053	118	0.027	23.3	0.094	6.7	-	-
1190-PS65	0.0042	150	0.027	23.3	0.094	6.7	-	-
250-dPS65	-	-	-	-	-	-	0.05	12.6
450-dPS65	-	-	-	-	-	-	0.05	12.6
820-dPS65	-	-	-	-	-	-	0.05	12.6

Relative to good solvent as discussed in Chapter 2, the same scattering regimes are present in the overall scattering data for bottlebrushes with dPS65 in θ solvent – Guinier plateau, Porod, surface, and local density fluctuations. However, some quantitative difference is observed. Most notably, the Porod region, indicative of the conformation of the overall molecule, has a slope of $|m|$=1.6 and the surface fractal has a slope of $|m|$=4.0. For the main-chain scattering profile, significant differences are observed relative to the good solvent behavior. The intermediate-q regime in which the tension from SC-replusion that was captured in good solvent conditions is completely missing. Instead, as can be seen in the Holtzer and Kratky plots in Fig. 3.2B and 3.2C, there is a distinct q-value, q^*_{lp}, in which the slope changes. For $q<q^*_{lp}$, a slope $|m|$=1.6 is observed. For $q<q^*_{lp}$, a slope of $|m|$=2.0 is observed ($|m|$=0 in Kratky plot).
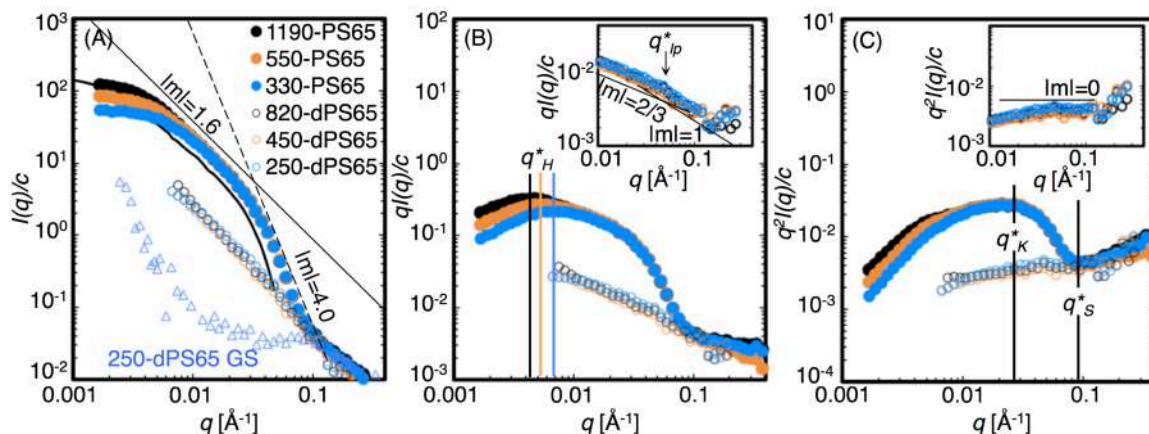
Figure 3.2. SANS spectra for BBPs with PS65 and dPS65 side-chains in θ Solvent. The scattering spectra (A) *I(q) vs. q* for BBPs with PS65 and dPS65 in θ solvent. Also plotted is 250-dPS65 in good solvent (blue triangle) and 1190-PS65 in good solvent (black). Slopes of |*m*|=1.6 and |*m*|=4.0 is included. (B) The Holtzer plot, *qI(q) vs. q* in which the q^*_H was determined. In the inset is the dPS65 series in which q^*_{lp} was identified. Slopes of |m|=1 and |m|=0.6 is included. (C) The Kratky plot, $q^2I(q)$ *vs. q*. in which q^*_K and q^*_s were determined. In the inset is the dPS65 series. A slope of |m|=0 is included.

3.3.2   *Effect of SC length – Good solvent*

The scattering results for *c*=1.0% PS25 and dPS25 in good solvent can be seen in Figure 3.3 and the length scales are summarized in Table 3.3. The 1.0% scattering profile was compared to dilute scattering profile. We show that the *q*-regime obscured by the semidilute interactions is *q*<*q_o*=0.095. The Guinier, Porod, surface, and local density fluctuation features are observed in the overall scattering profile. The Porod region can be characterized by a fractal dimension of |*m*|=1.4. The surface fractal shows a slope of |*m*|=4.
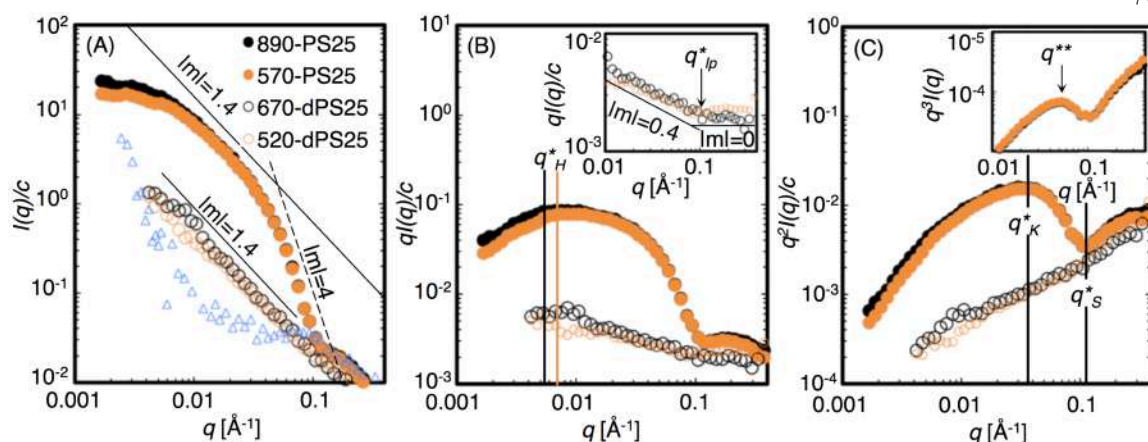
Figure 3.3. SANS spectra for BBPs with PS25 and dPS25 side-chains in good solvent. The scattering spectra (A) *I(q) vs. q* for BBPs with PS25 and dPS25 in good solvent. Also plotted is 250-dPS65 in good solvent (blue triangle). Slopes of $|m|$=1.4 and $|m|$=4.0 is included. (B) The Holtzer plot, *qI(q) vs. q* in which the q^*_H was determined. In the inset is the dPS25 series in which q^*_{lp} was identified. Slopes of $|m|$=0.4 and $|m|$=0 is included. (C) The Kratky plot, $q^2I(q)$ *vs. q.* in which q^*_K and q^*_s were determined. In the inset is the $q^3I(q)$ *vs. q* for PS25 series to identify the maximum, q^{**}.

As was the case for a reduction in solvent quality to θ solvent, with shorter side-chains, the intermediate-*q* regime with the $|m|$<0.5 behavior completely disappeared for the main-chain only profile. At high-*q*, $|m|$=1 is observed, the behavior observed in dPS65 good solvent, to $q=q^*_{lp}$=0.11. The slope observed in the Porod region of the overall bottlebrush is observed in the MC as well.

Table 3.3. Summary of SANS features and corresponding length scale obtained through the relationship $d=2\pi/q$ for BBPs with PS25 and dPS25 side-chains in good solvent.

	q^*_H [Å⁻¹]	d_H [nm]	q^*_K [Å⁻¹]	d_K [nm]	q^*_S [Å⁻¹]	d_S [nm]	q^*_{lp} [Å⁻¹]	l_p [nm]	q^{**} [Å⁻¹]
890-PS25	0.0052	121	0.038	16.6	0.12	5.2	-	-	0.058
570-PS25	0.0069	90	0.038	16.6	0.12	5.2	-	-	0.058
670-dPS25	-	-	-	-	-	-	0.11	5.7	-
520-dPS25	-	-	-	-	-	-	0.11	5.7	-

3.3.3 *Effect of side-chain length and main-chain length – dPS25 in θ solvent*

The scattering results for *c*=1.0% for PS25 and dPS25 in θ solvent can be seen in Figure 3.4 and the length scales are summarized in Table 3.4. The overall scattering pattern shows qualitative features consistent with that of bottlebrushes in literature. In this sample, the Porod region can be characterized by $|m|$=2.0 and the surface by $|m|$=4.0. Due

to the Porod region exhibiting a $|m|=2$, the Kratky plot could not be used to obtain the boundary between the Porod and surface scattering regime. Instead, the maximum from a $q^3I(q)$ vs. q plot was used and identified as q^{**} (for good solvent condition, the q^{**} is listed in the Table 3.3).

Figure 3.4 SANS spectra for BBPs with PS25 and dPS25 side-chains in θ solvent. The scattering spectra (A) $I(q)$ vs. q for BBPs with PS25 and dPS25 in θ solvent. Also plotted is 250-dPS65 in good solvent (blue triangle). Slopes of $|m|=2$ and $|m|=4$ is included. (B) The Holtzer plot, $qI(q)$ vs. q in which the q^*_H was determined. In the inset is the dPS25 series. A slopes of $|m|=1$. (C) The Kratky plot, $q^2I(q)$ vs. q. in which q^*_s was determined. In the inset is the $q^3I(q)$ vs. q for PS25 series to identify the maximum, q^{**}.

The main-chain conformation can be characterized by a fractal dimension of $|m|=2$. Due to the low scattering contrast, the high-q behavior could not be captured, and thus a length scale could not be defined. Once again, we see the intermediate q-regime with $|m|<0.5$ is absent in the main-chain in dPS25 solutions in θ solvent.

Table 3.4. Summary of SANS features and corresponding length scale obtained through the relationship $d=2\pi/q$ for BBPs with PS25 and dPS25 side-chains in θ solvent.

	q^*_H [Å^{-1}]	d_H [nm]	q^{**} [Å^{-1}]	d^{**} [nm]	q^*_s [Å^{-1}]	d_s [nm]	q^*_{lp} [Å^{-1}]	l_p [nm]
890-PS25	0.0058	108	0.060	10.5	0.13	4.8	-	-
570-PS25	0.0075	84	0.060	10.5	0.13	4.8	-	-
670-dPS25	-	-	-	-	-	-	-	-

3.3.4   Concentration Effect – Overall conformation

3.3.4.1   Single chain behavior of the MC

In BBPs, the concentration of monomers in the MC is extremely minute, for *Nsc*=65, 1 out of every 65 (roughly 1.5%) monomers is on the MC. Therefore, obtaining scattering signal from contrast matched side-chains is extremely difficult for dilute conditions. For example, a 1% solution of BBP contains roughly 0.015% MC units. In addition, as discussed in Chapter 2, BBPs adopt a highly anisometric shape in which intermolecular interactions begin at larger distances (lower concentrations). Therefore, the majority of the experiments were with conditions slightly in the semidilute conditions. Here, we compare the 1% results, extensively discussed in Chapter 2, and 0.4% data (still slightly semidilute) of 460-dPS65 to understand the MC behavior with decreasing concentration to gain insight about dilute condition behavior through extrapolation.
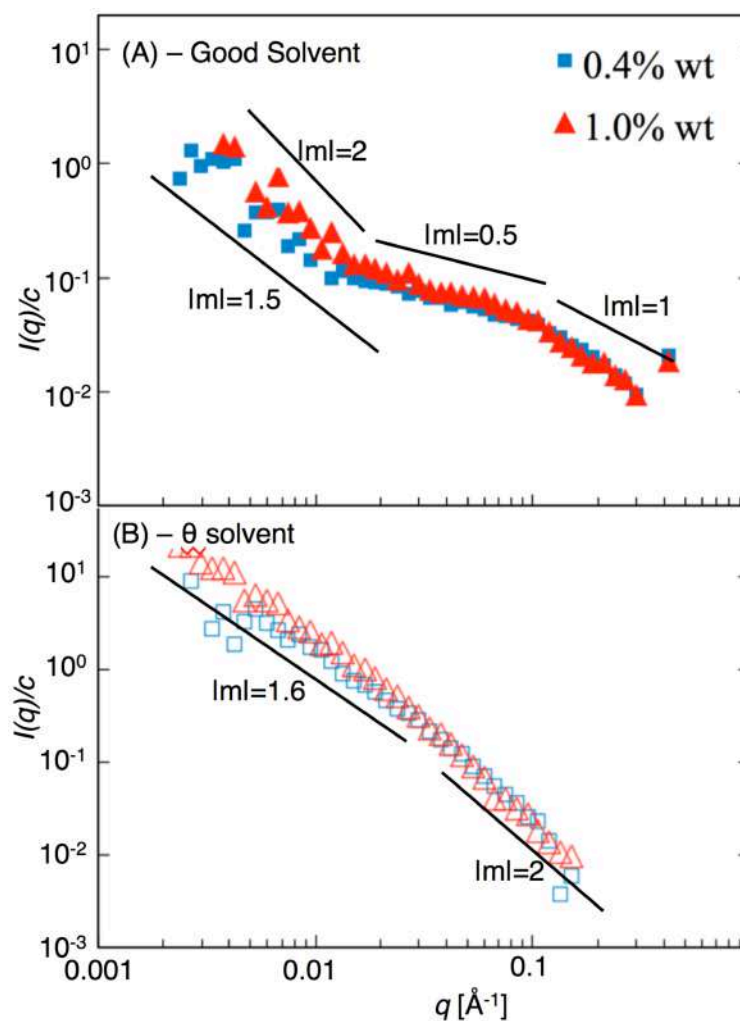
Figure 3.5 SANS spectra of 460-dPS65 in good and θ solvent at two concentrations. The scattering spectra for 460-dPS65 for two concentrations, 1% and 0.4% in (A) good solvent conditions. Slopes of $|m|=1$, $|m|=0.5$, $|m|=2$ and $|m|=1.5$ are included. (B) in θ solvent conditions. A slope of $|m|=1.5$ and $|m|=2$ is included.

Figure 3.5A shows 460-dPS65 in good solvent for 0.4% and 1.0%. Immediately, we see that the scattering regimes observed in 1.0% is present in the 0.4% as well. At high-q, $q>q^*_S$, a slope of roughly $1<|m|<1.3$ is observed. In the intermediate-q regime, $q^*_S<q<q^*_u$, the slope of $|m|=0.5$ is observed. The primary difference between 1% and 0.4% is observed in the low-q regime, $q<q^*_u$. Although extremely noisy and a quantitative value of the slope cannot be extracted, we see that the data points for 0.4% lie systemically below the 1.0% data, indicating a shallower slope for 0.4% than the 1.0% data. As a reference, a slope of $|m|=2$ seems to be a good approximation for 1.0% data.

In θ solvent, Figure 3.5B, a similar observation can be made. The low-q regime ($q<q^*_{lp}$) for 0.4% shows a nearly identical shape as the 1.0%. Only a slight decrease in slope is observed in the fractal dimension.

3.3.4.2 PNB-PS65 in Good solvent

With increasing concentration from 1% to roughly 20%, all of the PS65 samples seem to behave in a similar manner. In part (A) (Figure 3.6), the scattering profile of each concentration is offset by a factor of 10. In parts (B), (C), and (D), are the concentration normalized $I(q)/c$ vs. q for 330-PS65, 550-PS65, and 1190-PS65, respectively. In Chapter 2, we showed that the transition from dilute to slightly semidilute results in suppression of low-q intensity. Here, from 1% to 3-5%, the primary feature is the suppression of the low-q intensity. Each successive concentration step from 3-5% to 17-20% shows a steepening of the surface fractal ($q^*_S<q<q^*_K$) in addition to a suppression in low-q intensity. Beginning at 7-10%, a peak at roughly $q_{peak}(7\text{-}10\%)=0.025$ is observed. This peak shifts to higher-q with concentration $q_{peak}(20\%)=0.055$. In addition, at 19-20%, the high-q intensity upturn begins at higher $_q$-value than the other concentrations.
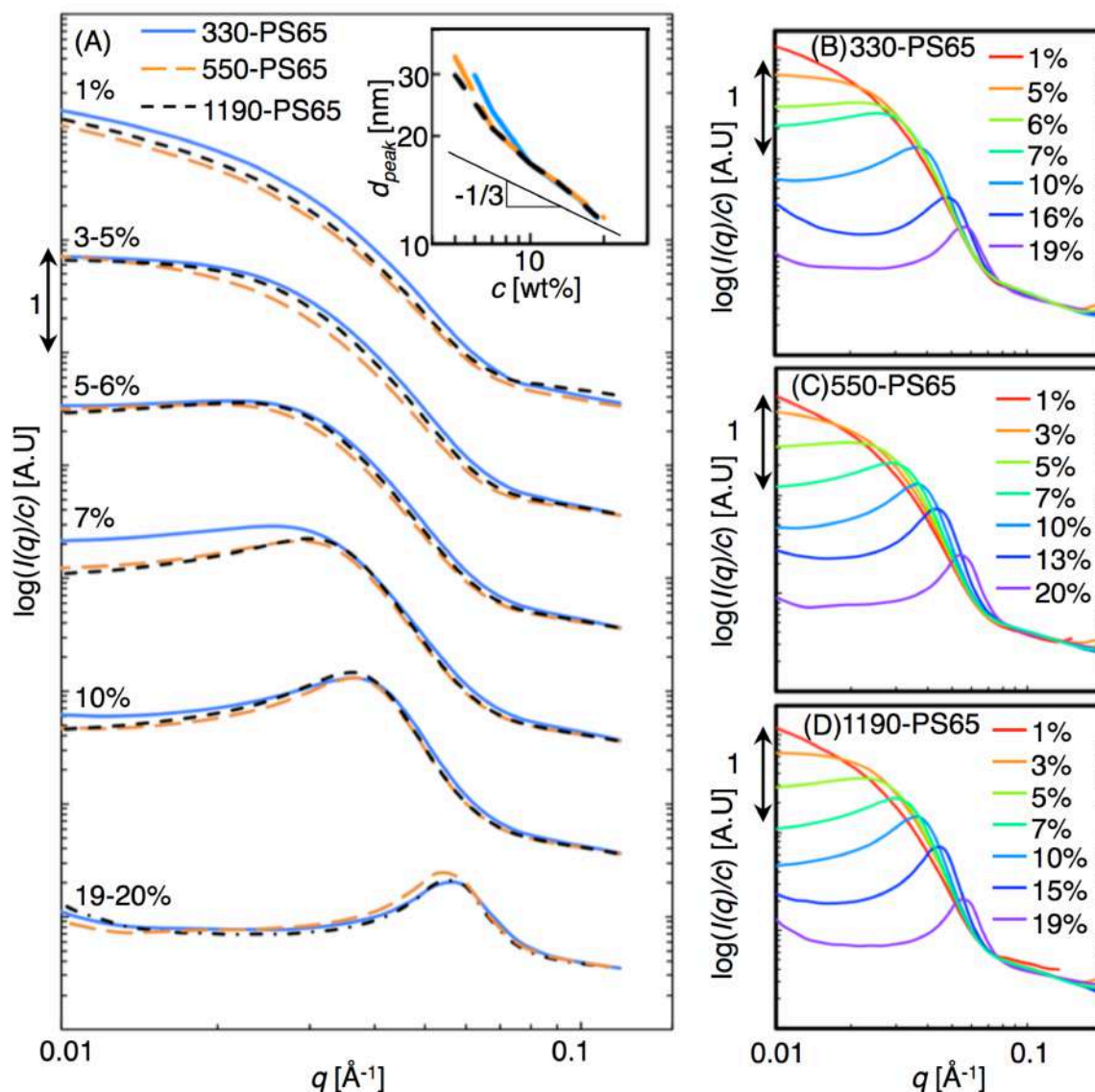
Figure 3.6. SAXS spectra for BBPs with PS65 side-chains in semidilute, good solvent, conditions. The SAXS scattering spectra for 330-PS65, 550-PS65, and 1190-PS65 in semidilute conditions ranging from concentrations 1% to 20% in good solvent. Each spectra is labeled with the corresponding concentration and was offset by a factor of 10. The concentration dependence on the peak position in d-space (d_{peak}) is summarized in the inset. For each BBP (B) 330-PS65, (C) 550-PS65, and (D) 1190-PS65, the scattering spectra for each concentration is plotted.

3.3.4.3   PNB-PS25 in Good Solvent

Similar results to PNB-PS65 in good solvent is observed for PNB-PS25. Figure 3.7 shows results, arranged in a similar format as Figure 3.6. At low concentrations, the primary change observed with concentration is a suppression in low-q intensity. Like PNB-PS65, the surface fractal feature steepens with increasing concentration as well. A

peak is observed beginning at 8-10% corresponding to q_{peak}=0.06. Surprisingly, the shift in the position of the peak is not as pronounced as PNB-PS65 series. In addition, the shift in the high-q intensity upturn is not observed for PNB-PS25.
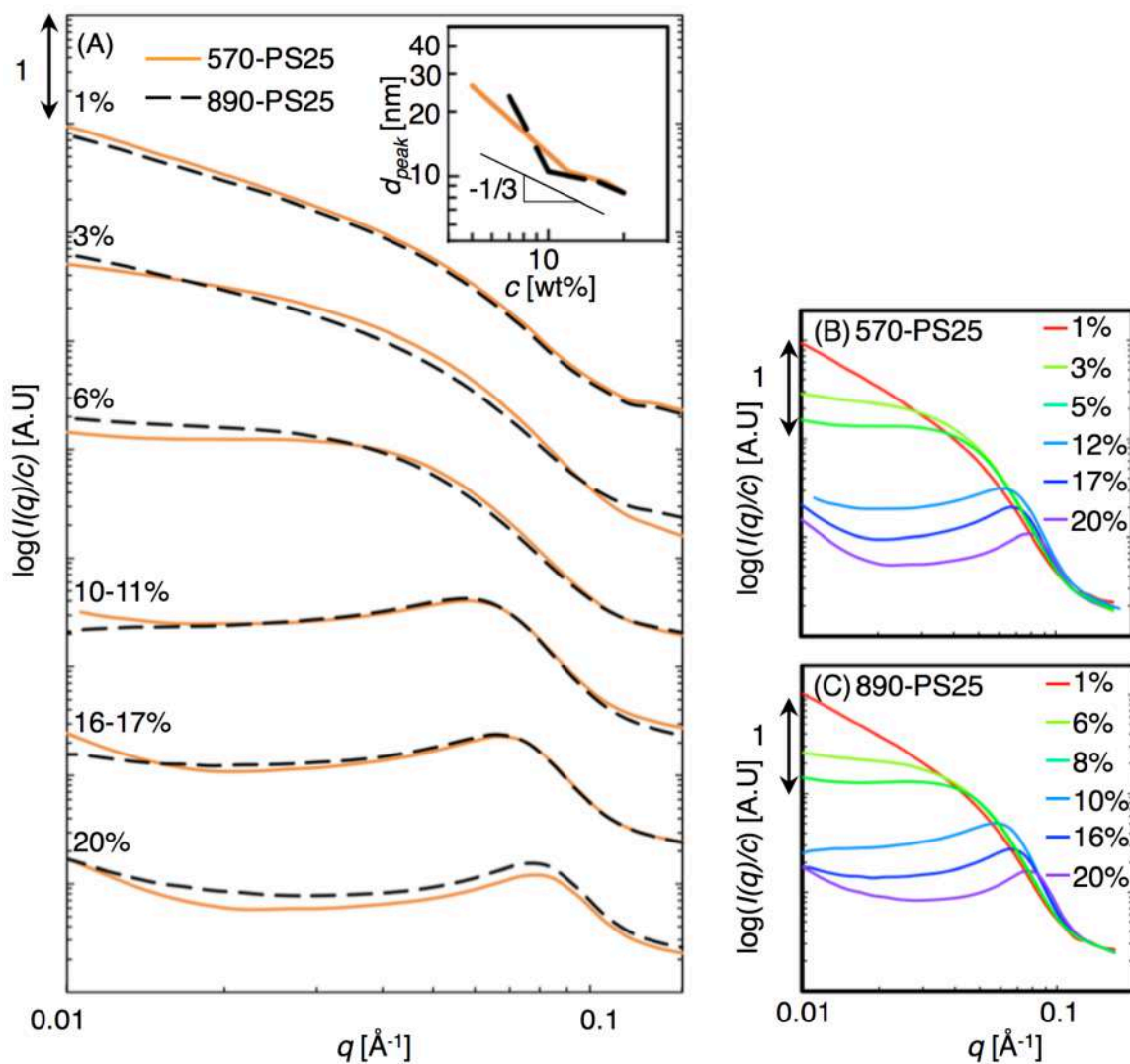
Figure 3.7 SAXS spectra for BBPs with PS25 side-chains in semidilute, good solvent, conditions. The SAXS scattering spectra for 570-PS25 and 890-PS25 in semidilute conditions ranging from concentrations 1% to 20% in good solvent. Each spectra is labeled with the corresponding concentration and was offset by a factor of 10. The concentration dependence on the peak position in d-space (d_{peak}) is summarized in the inset. For each BBP (B) 570-PS25 and (C) 890-PS25, the scattering spectra for each concentration is plotted.

3.3.4.4 PNB-dPS25 in Good solvent

The main-chain scattering spectra can be seen in Figure 3.8 for 540-dPS25 in good solvent for concentrations 0.4%-18%. With increasing concentration to 5%, a qualitative feature emerges for $q<0.02$Å. The scattering intensity is suppressed with respect to the 0.4%. For $q>0.02$Å, the scattering profile is consistent with that of 0.4%. The q-value at which the deviation from 'dilute conditions' is observed is defined as q_o. We see that q_o increases with increasing concentration, until c=14%. For c=14%-18%, q_o is approximately constant at q_o =0.075Å. For $q>q_o$=0.075Å, $|m|\approx1$.
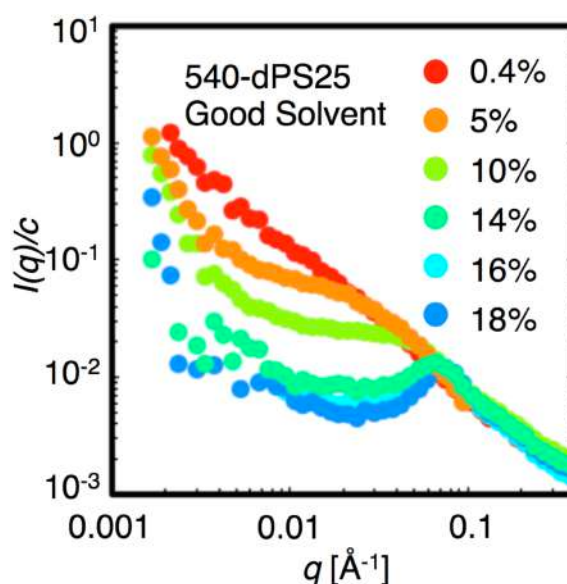
Figure 3.8 MC scattering spectra with increasing concentration for BBP with dPS25 side-chain. The SANS spectra for 540-dPS25 in good solvent for concentration range below 18%.

3.4   Discussion

3.4.1   θ Solvent for PS65/dPS65 Bottlebrush polymers

Our BBPs with dPS65 side-chains show that the pioneering work by Birshtein is observed, that even in θ solvent, BBPs adopt a SAW conformation. Both the main-chain and overall scattering spectra show a Porod regime with $|m|$=1.6, consistent with that of SAW. In addition, the high-q behavior of the main-chain shows Gaussian statistics, verified by the Kratky plot. Unlike wormlike chains, the main-chain is Gaussian at high-q

and SAW at low-q, accurately predicted by Birshtein and the tension blob model by Paturej et al.

Transitioning from good solvent to θ solvent, the tension from the SC repulsion is significantly decreased. Therefore, an increase in the tension blob size is expected as shown in Figure 3.9 indicating 4 length scale regimes. In regime I, $r<l_{p,o}$, the main-chain conformation is expected to be stiff. Unfortunately, $l_{p,o}$ was obscured by the low scattering intensity and the exact value of $q*_{lp}$ could not be resolved. In regime II, $l_{p,o}<r<l_p(k)$, chainlike statistics (Gaussian in θ solvent) of step size $l_{p,o}$ is expected. For $l_p(k)>r>\xi_{ten}(k)$, SAW of step size $l_p(k)\sim R_{CS}$ is expected from the tension blob model. Because the $\xi_{ten}(k)>R_{CS}$, the tension is completely screened. Our main-chain scattering spectra is consistent with the tension blob model, Gaussian at high-q and SAW at low-q. As was done for good solvent conditions in Chapter 2, $l_{p,app}/D=q*_{lp}/q*_K\approx0.54$ in θ solvent. With no 2-body interactions at the θ point (3-body interactions present), a reduced value of $l_{p,app}/D$ follows the expected behavior from reduced SC repulsion interactions.
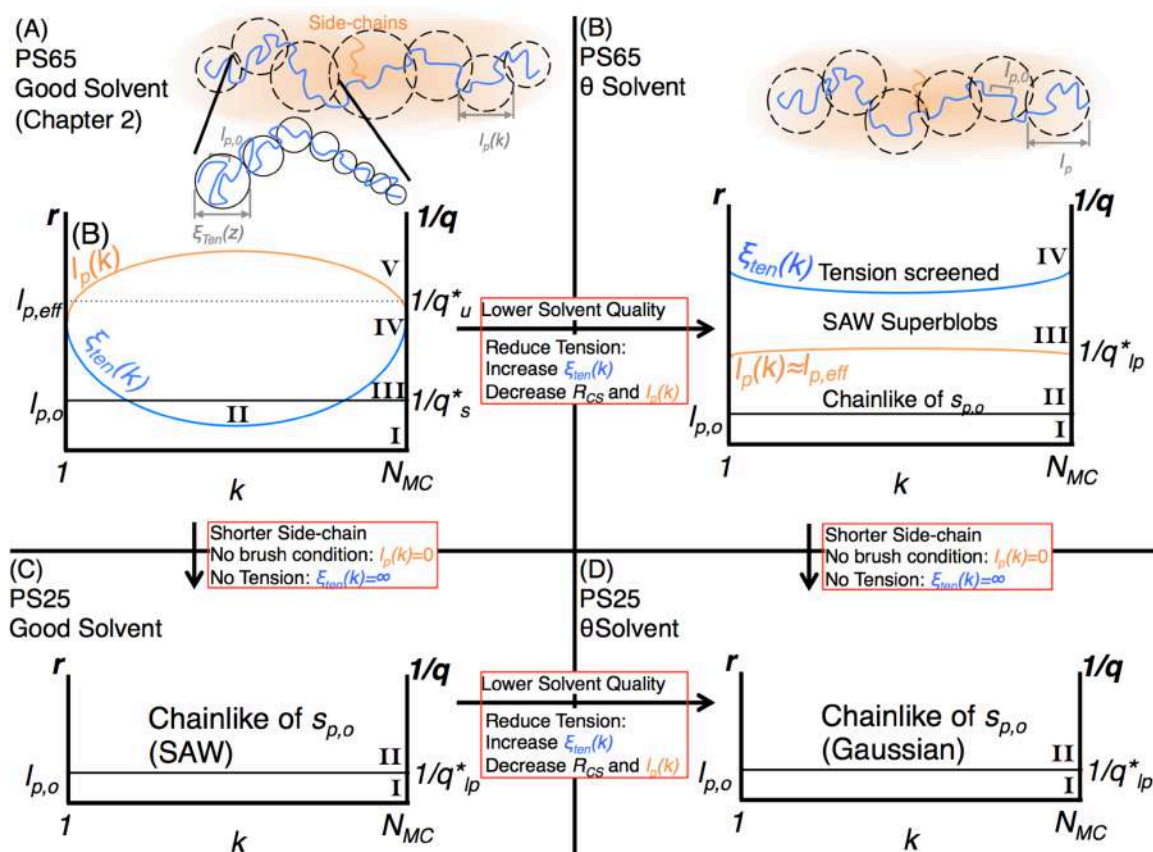
Figure 3.9. Summary of tension blob model. (A) The tension blob model analysis of PS65 in good solvent. The five different length scale regimes are detailed in Chapter 2. A schematic representation is included to help visualization of the length scales. (B) The tension blob model analysis of PS65 in θ solvent showing four length scale regimes. A schematic representation is included to help visualization of the length scales. The length scales of PS25 in (C) good solvent and (D) θ solvent showing 2 length scales in each solvent condition.

3.4.2   Effect of side-chain length

3.4.2.1   PS25 and dPS25 in Good solvent

When the sidechain length is reduced to PS25 and dPS25, we observed a qualitatively different main-chain scattering spectra in good solvent despite observing identical features in the scattering spectra of the overall bottlebrush. Therefore, we show that the side-chains dominate the scattering contribution and making assertions solely based on scattering spectra of the overall bottlebrush could lead to misleading results. The most notable difference between dPS65 BBPs and dPS25 BBPs is the absence of the intermediate *q*-regime with a slope |*m*|<1 indicative of tension. With shorter side-chains, tension is expected to be reduced. However, our results indicate that the system is not

under tension. Instead, we observe a $l_{p,o}$ (from sterics, not tension) adopting a slightly extended conformation from a combination of SAW of good solvent and an additional random walk restriction by impermeability of superblobs. Even though the main-chain is not under tension, there are 2-body and possibly 3-body interactions preventing from overlap of superblobs. Instead of BBP behavior observed in BBPs with PS65/dPS65, the behavior is more consistent with that of linear/comb-like polymers with a 'swollen' chain conformation of the main-chain as well as the overall brush behavior.

3.4.2.2   PS25 and dPS25 in θ Solvent

As expected, with PS25 and dPS25 side-chains the θ solvent behavior is reminiscent of linear polymers. First, the main-chain scattering profile can be characterized by a single fractal dimension of $v \approx 2$, approximately a Gaussian chain. The same fractal dimension can characterize the Porod regime of scattering spectra of the overall brush. Even though in a bottlebrush architecture, a SAW of superblobs has not been observed. Due to the absence of excluded volume interactions

3.4.3   Bottlebrush polymer limit

With a transition from PS65 to PS25 showing qualitatively different behaviors, we have shown that the side-chains constitute two different behavioral regimes – BBP for PS65 and linear/comb-like for PS25. This sheds light on some of the controversy in literature regarding the conformation of BBPs as many experimental work considers side-chains as short as $N_{SC}=6$ units to be in the same behavioral regime as much longer side-chains to extract a single scaling exponent. With the distinct conformational changes arising from tension, beginning at a critical side-chain length, the regimes must be considered independently to obtain appropriate parameters. Therefore, we can begin to delineate between a 'bottlebrush polymer' regime, which is characterized by an extension (distinct from 'swollen') of the main-chain from that of a 'comb polymer' and/or 'linear polymer' regime, which has yet to be done in literature (Figure 3.10). Here we want to emphasize that the side-chain length required for stretching is expected to be high

dependent on the graft spacing and chain properties of the main-chain, and thus the delineation is valid only for bottlebrush polymers with a PNB main-chain.
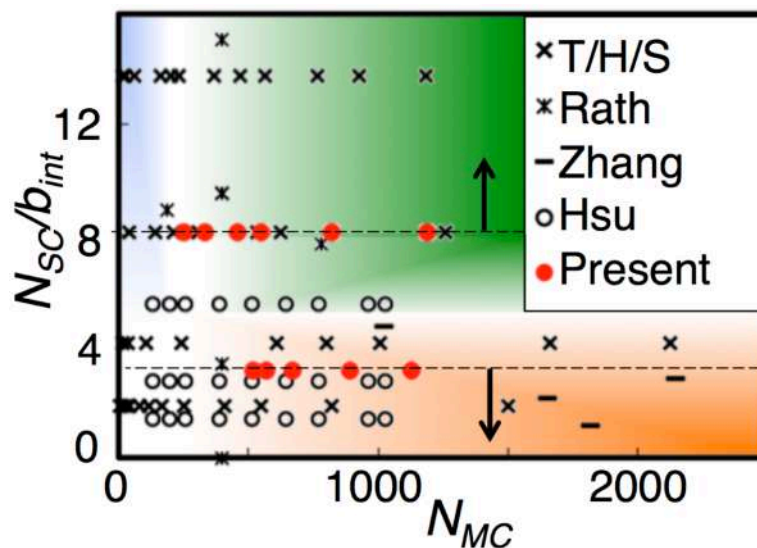
Figure 3.10. **Updated parametric space with current results**. The parameter mapping of bottlebrush architecture with bottlebrush limit (up arrow) and linear/comb (down arrow).

3.4.4 Concentration Effects - Screening of excluded volume interactions

Borisov et al. had predicted that with increasing concentration from dilute conditions, the excluded volume interactions begin to be screened in order of largest to shortest length scales, i.e. from dilute to slightly above dilute, the SAW of steps l_p gets screened to a RW of steps l_p while all shorter length scales remain unperturbed. They predicted 4 concentration regimes as described earlier. Recent simulations by Paturej et al. support the notion that screening of the excluded volume occurs on the respective length scales, and even identified an additional length scale to that of Borisov. Our experimental results show agreement to their predictions and observations to an approximation. First, we can see in the semidilute regime, the scattering profiles are nearly identical at approximately the same concentrations (±2wt%) for $q>0.01$ for PS65 BBPs, showing identical concentration regimes. From Chapter 2, we saw a transition from dilute (~0.1%) to (1%), a suppression in low-q ($q<0.007$Å) intensity while the rest of q-space profile was unperturbed, confirming the hypothesis by Borisov that screening of interactions occurs at

the different length scales. From parts (B)-(D), we can identify additional concentration regimes. First, the surface fractal ($q^*_S<q<q^*_K$) sharpening in slope is a trend observed for a sharper interface. The same behavior is observed in PS25 bottlebrushes. Therefore, with increasing concentration, interbrush SC interaction is observed, a trend expected with decreasing side-chain length predicted by both Borisov and Paturej. Paturej attributed the size decrease to be from interpenetration of side-chains of neighboring brushes to screen the SC excluded volume interactions from side-chains of the same brush. Our main-chain scattering profile challenges this notion.

From concentration 5%-14%, deviations from 0.4% profile shifts to progressively higher q value. This once again affirms predictions by Borisov and Paturej of screening excluded volume interactions at respective length scales. However, for 14-18%, remains unchanged at $q≈0.065$ corresponding to a d=9.7nm. With a roughly $1<|m|<1.3$ slope, this indicates the length scale corresponds to a persistence length. Therefore, we show an increase in persistence length from 1%, $l_{p,app}(c>14\%)/l_{p,o}(1\%)=1.7$. If interpenetration of side-chains from neighboring brushes was screening the excluded volume interaction of side-chains, we would not observe a higher persistence length at higher concentrations. If side-chains from neighboring brushes were to avoid interpenetration, a lateral repulsion would induced crowding of side-chains around the main-chain resulting in an increase in $l_{p,app}$, as observed here. This explanation also resolves the controversy of observing lyotropic phases (requiring $l_{p,app}/D>>3.34$ from predictions by Onsager) for bottblebrushes described by a SAW of superblobs model ($l_p/D\sim O(1)$). At higher concentrations, lateral repulsion from resisting interpenetration with neighboring brushes results in reduced side chain size (decrease D) and induces additional extension of the main-chain (increasing $l_{p,app}$). Therefore, both parameters vary in a manner favoring the existence of lyotropic behavior at high concentrations ($l_{p,app}/D$ increases).

Increasing concentration

(1) Dilute   (2) Semidilute   (3 & 4) Isotropic Concentrated   (3) Side chain repulsion   (4) Side chain interpenetration
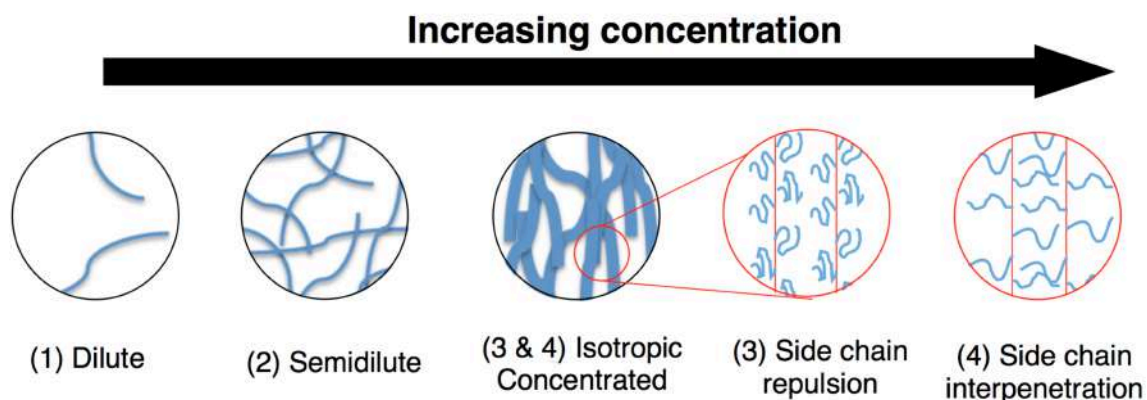
Figure 3.11. Schematic of concentration regimes of bottlebrush polymers. Schematic diagrams of various degrees of inter-bottlebrush interactions from dilute (left) regimes to side-chain interpenetrated regime (right).

Unfortunately, a lyotropic phase was not observed in any of our samples. Instead, bottlebrushes with PS65 side chains shows a concentration regime not observed for PS25. At concentration 19-20%, the high-q intensity upturn occurs at a higher q-value than for concentrations below 19%, in which case the q-value was a constant. This dramatic shift can be explained by an interpenetration of side-chains at which point the excluded volume interactions can be screened. Bottlebrushes with PS25 side-chains may exhibit this phase at higher concentrations, but our main-chain scattering results showing a lack of tension led us to believe that this effect will be minimal even at high concentrations. The absence of a lyotropic phase could be due to two reasons: (1) higher concentrations are required to induce lyotropic ordering or (2) higher SC-repulsion is required (longer side-chains or shorter graft distances). The latter seems more plausible as interpenetration of side-chains is expected begin screening excluded volume interactions.

In total, our work show the following concentration regimes summarized in Figure 3.11: (1) Dilute in which a bottlebrush can free adopt a conformation in solution ($c<0.1\%$), (2) semidilute I in which the excluded volume interaction of the overall brush were screened resulting in a more compact conformation than in dilute ($0.1\%<c<{\sim}1\%$), (3) semidilute II in which side-chains begin to become more compact through resisting interpenetration of side-chains of neighboring brushes, resulting in a higher persistence length than in dilute conditions (${\sim}1\%<c<{\sim}15\%$), and (4) semidilute III in which side-chains

begin to interpenetrate screening the side-chain excluded volume interactions within the same bottlebrush. A concentration regime observed by Paturej was not captured, as the main-chain scattering profile of dPS65 would be required to confirm or deny the existence of the respective concentration regime.

3.5   Summary

To summarize, we showed qualitative differences in the main-chain conformation of bottlebrushes with dPS65 and dPS25 in dilute solution, delineating a boundary between linear/comb-like polymers from that of bottlebrush polymers with extended main-chain conformation, a boundary which has yet to be discussed in literature. For bottlebrushes in the bottlebrush regime, our results are in accord with predictions by the tension blob in the θ solvent as well as the good solvent.

Although bottlebrushes with PS25 side-chains did not exhibit tension in dilute conditions, with semidilute interactions at higher concentrations, we observed an increase in the persistence length. With a decrease in side-chain size and an increase in persistence, we shed light onto a controversy in literature as to the existence of lyotropic phases for bottlebrushes in solution by showing that both parameters in $l_{p,app}$ and D, change in a manner to favor an increase in $l_{p,app}/D$.

However, we showed an upper bound to the $l_{p,app}$ as the side-chains began to interpenetrate at the highest concentration used in this work. In addition, we showed experimental verification of various concentration regimes discussed in literature.

Chapter 4

CRYSTALLIZATION DRIVEN ORDERING AND SELF-ASSEMBLING UTILIZING THE BOTTLEBRUSH ARCHITECTURE

4   Introduction

With many polymeric units incorporated into a single molecule in bottlebrush architecture, one primary advantage over linear polymers is the additional degree of functionality for bottlebrush polymers. Properly engineering macromolecules utilizing this advantage requires a fundamental understanding of the behavioral changes associated with additional functionality.   In addition, crystallization of polymers expands the range of properties accessible to polymer systems, and when incorporated into a bottlebrush architecture a fascinating interplay between self-assembly and crystallization is expected. In this chapter, we characterize bottlebrush polymers with two chemically distinct semi-crystalline polymers, polyethylene and polycaprolactone, arranged in the bottlebrush architecture into three representative bottlebrush copolymer connectivities. To properly understand the effect of connectivity within the bottlebrush architecture, we summarize literature work on the interplay of self-assembly and crystallization of linear systems and the self-assembly behavior of bottlebrush polymers.

4.1   Literature Overview

4.1.1   Linear block copolymer crystallization

Block copolymer crystallization can be grouped into two categories: crystallization from disordered melt or crystallization from an ordered (phase separated) melt. Depending on the initial amorphous conditions, a myriad of crystallization-morphology interplay was observed. In summary, three types of crystallization has been identified: (1) confined crystallization, where crystallization occurs within phase separated phase; (2) break-out crystallization, where crystallization drives the formation of morphology, overriding the pre-existing microstructure; or (3) template crystallization, which shows crystallization

kinetics similar to that of break-out crystallization while preserving the morphology. The type of crystallization was shown to depend on the following factors: the crystallization temperature, the glass transition temperature, the relative fraction of semicrystalline component, and original phase in which the crystallization takes place. A more detailed discussion is attached.

4.1.2   Crystallization from disordered melt

Rangarajan et al.[66,67] studied crystallization from weakly segregated diblock copolymers and showed the formation of lamellar morphology driven by crystallization, referred to as 'break-out' crystallization. He showed that the crystalline chains ran orthogonal to the morphological interface. Zhu et al.[68] considered weakly segregated block copolymer systems and showed that the interplay of crystallization and self-assembly could be controlled by the crystallization temperature, T_c, with respect to the glass transition temperature, T_g. For $T_c > T_g$, break-out crystallization favoring lamellar morphology was observed. For $T_c < T_g$, confined crystallization was observed due to the glassy state of the noncrystalline component.

4.1.3   Crystallization from ordered melt

Douzinas and Cohen[69] observed that crystallization from a lamellar morphology was confined to the microphase, preserving the overall morphology. In addition, they observed the chains ran parallel to the morphological interface. Ryan et al.[70] showed that the relative volume fraction of the semicrystalline not only affects the morphology in the morphology, but the degree of break-out crystallization. For symmetric block copolymers, the confined crystallization was observed. For asymmetric in favor of the crystallizable component, the hexagonal morphology was destroyed, forming a crystallization driven lamellar morphology. For asymmetric in favor of the amorphous component, the hexagonal morphology was destroyed. Hamley et al.[71] observed for a breakout crystallization from hexagonal morphology to lamellar morphology that the stems ran parallel to the morphological interface. Mai et al.[72] showed that thermal pathways could be used to control various morphologies in the melt to a lamellar crystallization driven

morpoholgy. Zhu et al.[73], using shear to orient the lamellar morphology, showed that the T_c, could be used to control the orientation of chains with respect to the morphological interface in crystallization confined to the lamellar morphology. Similarly, Loo et al.[74] oriented the cylinder through the use of flow and showed 2D crystallization. The morphology analysis by Hong et al.[75] showed that the chains run parallel to the morphology. Loo et al.[76] observed that in the ordered melt phase with a glassy matrix, confined crystallization was observed for various morphologies. Within the lamellar domain, the chains ran parallel to the morphological interface. Shiomi et al.[77] showed that crystallization within a lamellar morphology could break out into a newly crystallization lamellar morphology. In addition, they showed crystallization with a cylindrical morphology could be controlled with T_c. Generally, crystallization favors the formation of lamellar morphology, but is limited by the kinetics of crystallization. Crystallization kinetics by Loo et al.[78] showed an additional crystallization mode, templated crystallization retaining morphology while showing sigmoidal crystallization kinetics, distinct from confined crystallization (first-order crystallization) and breakout crystallization (overrides morphology).

Block copolymers with dual semicrystalline blocks show an additional interplay between morphology and crystallization, as the preformed morphology is neither rubbery nor glassy, but semicrystalline. Nojima et al.[79] showed that crystallization of the second component can override the semicrystalline morphology by the first crystallization component.

4.1.4   Self-assembly of bottlebrush copolymers

Xia et al.[6] showed that the self-assembly of bottlebrush systems can be controlled by the arrangement of chemically distinct side-chains within the bottlebrush architecture. When side-chains are grafted into to blocks, forming a bottlebrush block copolymer, they showed that the morphology domain spacing is dependent on the main-chain length and independent of the side-chain length. When side-chains are randomly interlaced, they

showed that side-chains reorient a lamellar morphology dependent on the side-chain length and independent of the main-chain length.

The domain spacing of the bottlebrush block copolymer was approximately the same size as the fully extended contour length of the main-chain, leading them to propose a fully extended main-chain conformation in a phase-separated melt, achieving the domain spacing through interdigitation of the main-chain. Dalsin et al.[8], through experiment and simulations, showed that although the main-chain is oriented away from the morphological interface, the main-chain is not fully extended. The domain spacing equal to the contour length was obtained with the main-chain from opposing interface contributing half of the domain spacing each. Chang et al.[7] also showed an interesting mixed-domain morphology behavior which required the main-chain to have some degree of flexibility.

Gai et al.[55] showed that relative to the linear block copolymers, lamellar morphology occupies a much larger volume fraction range in the phase diagram showing lamellar morphology for f_A=0.28-0.72, with the number of side-chains as the variable. However, Rzayev et al.[56] showed cylinder morphology for asymmetric side-chain lengths and symmetric main-chain lengths, showing the asymmetry in side-chain lengths can significantly influence the morphology. Simulation of bottlebrushes in aqueous solution by Wang et al.[80] showed a wide variety of morphologies for hydrophobic side-chains on hydrophilic main-chain (Figure 4.1).
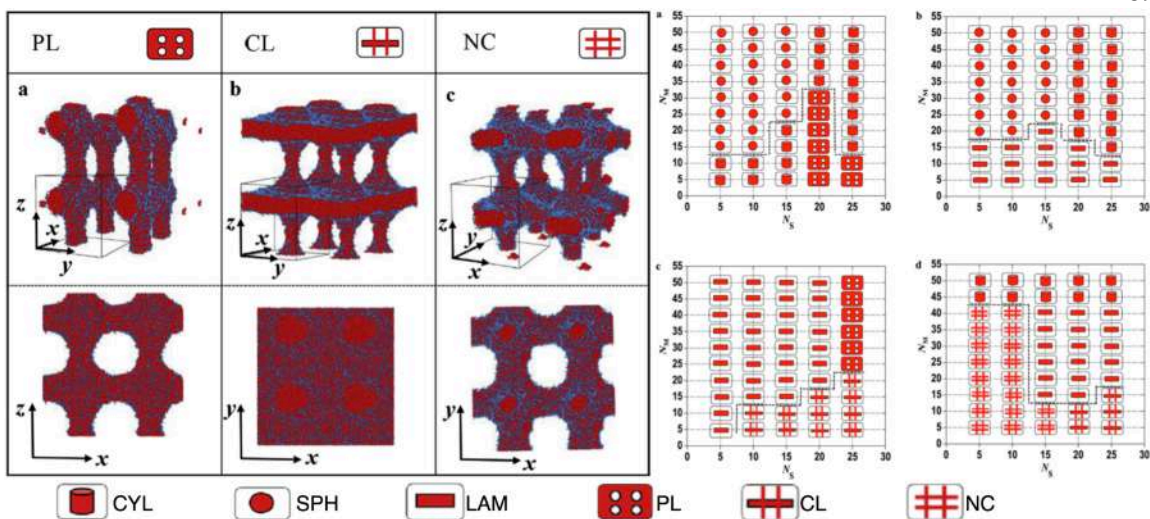
Figure 4.1. Bottlebrush morphology in solution by Wang et al. Schematic of complex morphologies not typically observed for linear polymers and the phase diagrams at various concentrations. CYL=cylinder, SPH=spherical, LAM=lamellar, PL=perforated lamella, CL=cross-linked lamella, NC=networked cylinder. [Adapted from reference 20].

4.2   Materials Section

4.2.1   Macromonomers

The materials used in this work was synthesized by Dr. Hefeng Zhang from the Hadjichristidis Group from KAUST. Their synthesis protocol has been detailed and published in Reference[81].

The chemical structure three macromonomers used are in Figure 4.2. With the short side-chain lengths used, the main-chain contribution cannot be assumed to be negligible (the PNB main-chain contributing up to f_{MC}=0.19 for the E5 side-chain). The melting temperature for an analogous linear polymer with identical MW is listed as well. Due to the differences in backbone atoms per monomer for PE (2 carbon atoms) and PCL (6 carbon and 1 oxygen atom) there is a substantial difference in length/monomer. Therefore, instead of identifying bottlebrushes with side-chain DP, as is typically done for polymeric systems, the fully extended contour length of the side-chains in nanometers will be used to more accurately reflect the length scale of each component, 'Notation' column

in Table 4.1. For the block copolymer side-chain, E8-*b*-C12, it is important to note that the side-chain is grafted on the PCL end.
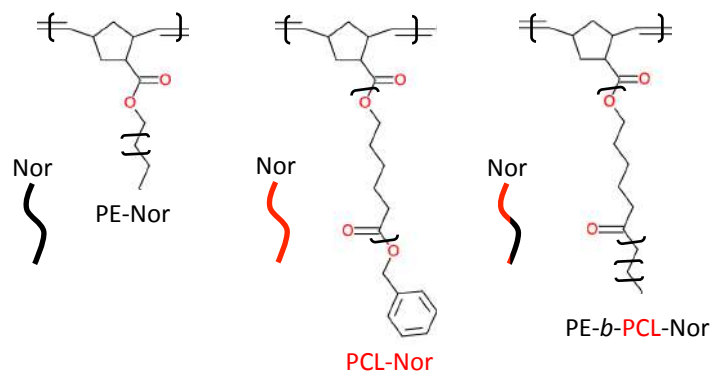
Figure 4.2. Macromonomer chemical structures. Chemical structures of the macromonomers used to synthesize the bottlebrush copolymers. Refer to ref. [81] for details on the synthesis.

Table 4.1. Molecular characteristics of macromonomers.

Macromonomer	PE/PCL MW [g/mol]	Non-crystalline MW [g/mol]	Mass Fraction [$f_{PE}/f_{PCL}/f_{NC}$]	Contour Length [nm]	Notation
PE-Nor	604	136	0.82 / 0 / 0.18	5.4	E6
	564	136	0.81 / 0 / 0.19	5.0	E5
PCL-Nor	4871	229	0 / 0.96 / 0.04	37.4	C37
	2801	229	0 / 0.92 / 0.08	21.5	C22
PE-b-PCL-Nor	853 (E)	136	0.33 / 0.61 / 0.05	7.6	E8-b-C12
	1567 (C)	-	-	12.0	

4.2.2 Bottlebrush Sample List

In collaboration with Nikos Hadjichristidis (KAUST), we study the effects of the connectivity, the variation in arrangement, of chemically distinct units within bottlebrush architectures (Figure 4.3) by studying 8 bottlebrushes. In contrast to **H**omo-bottlebrush polymers (H), which are composed of side chains having the same uniform chemical functionality, three types of bottlebrush copolymers combine two more different types of repeat units: 1) **M**ain-chain-block bottlebrushes (M) have chemically distinct side chains grafted in blocks along the main chain; 2) **R**andom-co-bottlebrushes (R) have a statistical distribution of side chains in accord with the number fraction of each side chain; and 3) **D**iblock-side-chain bottlebrushes (D) have diblock copolymers as their side chains, similar to Janus bottlebrushes as reported by Kawamoto et al.[54] With 100% grafting density, the

DP_{PNB} is equal to the number of side-chains and is incorporated into our notation. The final mass fraction of each component, PE, PCL, and noncrystalline (PNB/linker/ends), are listed in the Table 4.2. To understand the effects of connectivity, the segregation strength, χN, assuming a linear block copolymer constituted by the respective molecular weights of the side-chains, have been calculated and listed in the Table as well.
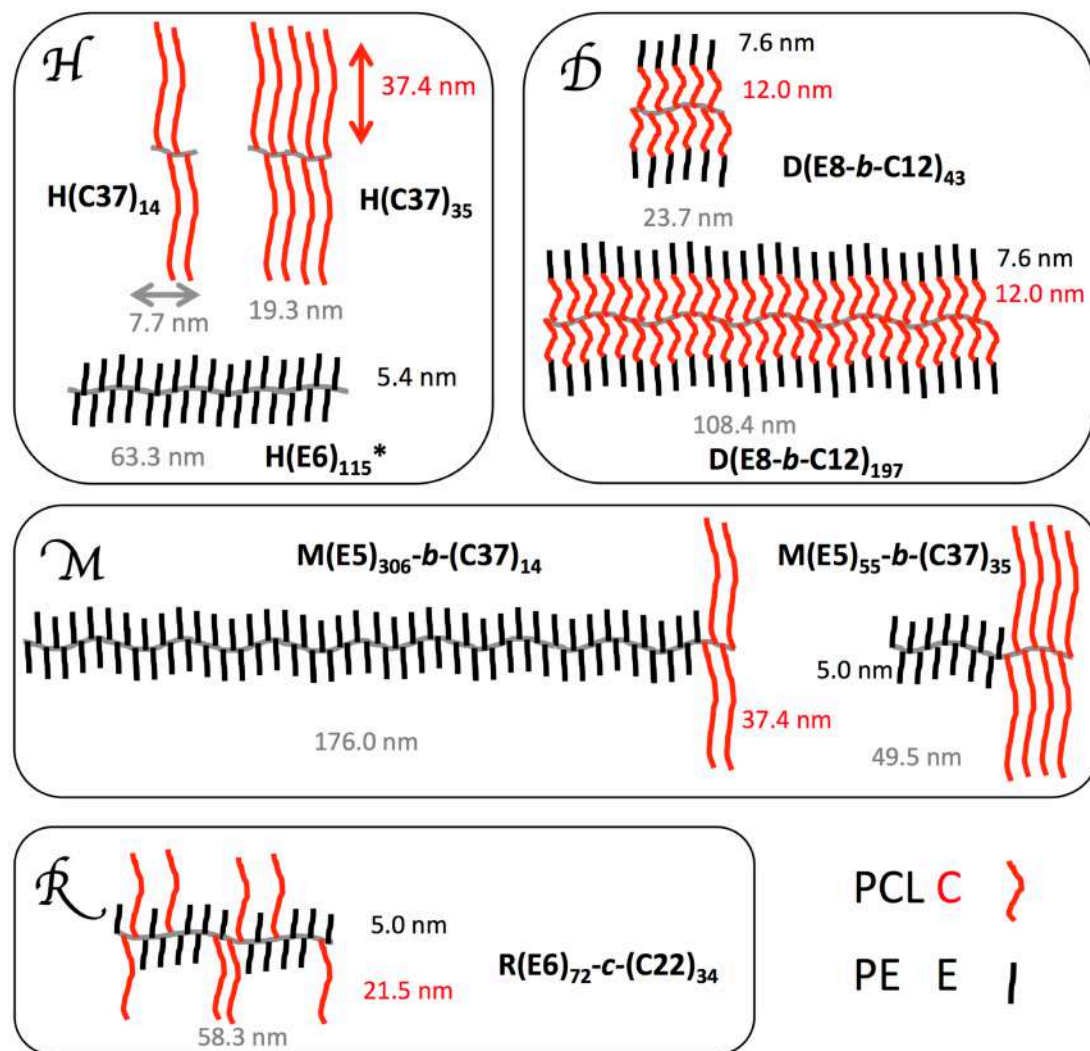
Figure 4.3. Schematic of bottlebrush copolymer samples. Schematic representation of the bottlebrush copolymer samples studied. The samples are categorized by the copolymer arrangement the bottlebrush architecture: H-Type for homo-bottlebrush polymer, M-Type for main-chain diblock bottlebrush copolymer, R-Type for random bottlebrush copolymers, and D-Type for diblock side-chain bottlebrush copolymer.

Table 4.2. Bottlebrush copolymers sample molecular characteristics. Material characteristics including molecular architecture and interaction parameter of the samples used in this study.

Sample	Side-chain MW PE [g/mol]	PCL [g/mol]	No. Side-chains PE	PCL	Mass Fraction f_{PE}	f_{PCL}	$f_{Non-cryst}$	χN Single SC[a]	Total Mass[b]
H(E6)$_{115}$	604	-	115	-	0.82	0.00	0.18	-	-
H(C37)$_{14}$	-	4871	-	14	0.00	0.96	0.04	-	-
H(C37)$_{35}$	-	4871	-	35	0.00	0.96	0.04	-	-
M(E5)$_{55}$-*b*-(C37)$_{35}$	564	4871	55	35	0.14	0.79	0.07	5.5	228
M(E5)$_{306}$-b-(C37)$_{14}$	564	4871	306	14	0.60	0.24	0.16	5.5	587
R(E6)$_{72}$-*c*-(C22)$_{34}$	604	2801	72	34	0.28	0.61	0.11	4.1	209
D(E8-*b*-C12)$_{43}$	853	1567	43	43	0.34	0.61	0.05	3.3	144
D(E8-*b*-C12)$_{197}$	853	1567	197	197	0.34	0.61	0.05	3.3	659

[a] for diblocks with PE and PCL block lengths identical to side chain length

[b] for diblocks with PE and PCL block lengths equal to the total PE and PCL lengths in a given sample

4.2.3 Miscibility Analysis

As can be seen in the phase diagram[52] in Figure 4.4, all of the hypothetical linear block copolymers made by the individual side-chain used in our work are predicted to be in the disordered phase. The Flory-Huggins parameter was estimated using the Hildebrand and Hansen solubility parameters. The filled and open symbols represent the lower and upperbound of the segregation strength.
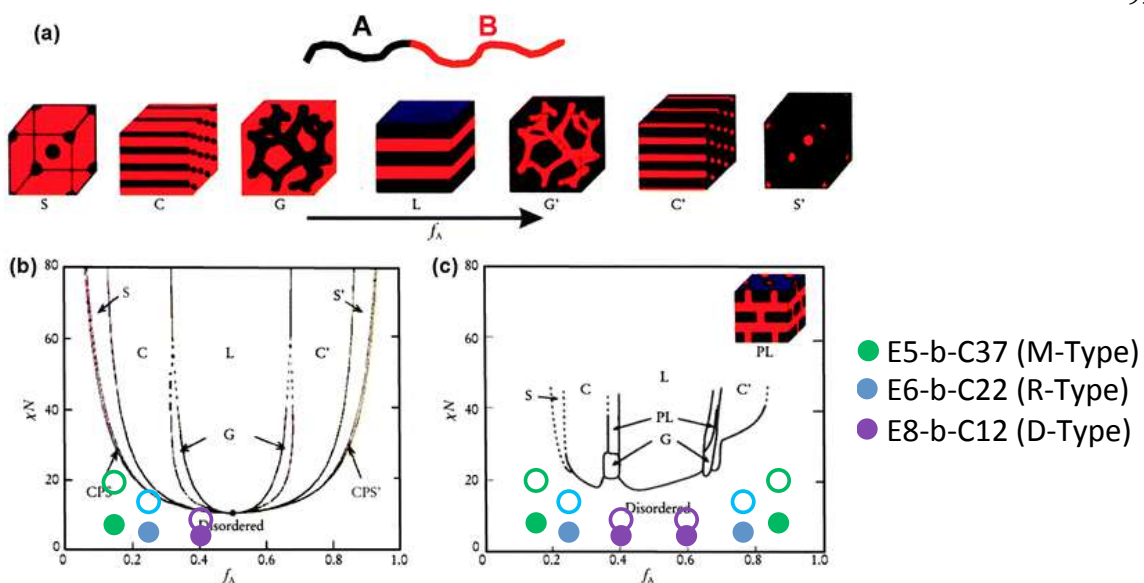
Figure 4.4. Miscibility Analysis. Interaction parameter of the samples used in this study on the interaction parameter phase map. The phase diagram was adapted from reference 78.

4.3 Experimental

4.3.1 Differential Scanning Calorimetry

Differential scanning calorimetry (DSC) thermograms were obtained at temperature scan rates of 10°C/min on a Mettler Toledo DSC1 Star System at the King Abdullah University of Science and Technology. The instrument was calibrated using an Indium standard. The samples were sealed in aluminum pans with about 2 mg per sample. The temperature protocols used were heating/cooling rates of 10°C/min with temperature ranging from -20 to 120°C. At -20°C and 120°C, the samples were held for 10 minutes. Enough temperature cycles were performed until consecutive cycles produced identical endo and exotherms.

4.3.2 Variable Temperature Small Angle X-ray Scattering

Small angle X-ray scattering patterns were obtained at Beamline 12-ID-B at the Advanced Photon Source at Argonne National Laboratory. Sample-to-detector distances were 3.61 m with an X-ray beam energy of 13.3 KeV (λ=0.932 Å) and calibrated with a silver behenate standard. The samples were sealed in aluminum DSC pans and a home-

built multiarray heating stage was used for temperature control. The temperature protocol ranged from 14°C to 120°C at a rate of 10°C/min with the sample held at the temperature extremes for 5 min to mimic the DSC results. SAXS patterns were collected approximately every 60 s (10°C) with an exposure time of 0.1s.

4.3.3   Transmission Electron Microscope

Transmission electron microscopy images were obtained on Tecna Twin 120V at the King Abdullah University of Technology. The samples were ultra-cryo-microtomed using LN_2 with thicknesses of 50nm. The sections were placed onto copper grids and vapor stained using OsO_4.

4.3.4   Atomic Force Microscopy

Atomic Force Microscopy images were acquired on the Asylum MFP-3D, with temperature control capabilities, at the Molecular Foundry at Lawrence Berkeley National Laboratory. Heating was postponed during image collection for D-Type. Samples were drop cast onto Si wafer from 1% solutions in toluene and dried in a vacuum oven. Samples were annealed with >3 cycles of heating/cooling from RT to 120°C at 10°C/min.

4.3.5   Variable Temperature X-ray Diffraction

X-Ray Diffraction (XRD) measurements were taken on a D8 Advance Bruker at the King Abdullah University of Science and Technology. Environment control was obtained using Anton Paar TTK 450 Low Temperature Chamber with liquid nitrogen cooling. Due to the temperature controller set up, the system tended to overshoot the targeted temperature by up to 6°C before equilibrating to the desired temperature. The X-ray λ=0.154nm. Samples were preannealed from cooling from 120°C to RT at roughly 10°C/min to mimic the thermal history of samples in DSC samples. XRD patterns were heated from 30°C to 120°C at roughly 10°C/min postponing heating during data acquisition.

4.4   Results

4.4.1   Differential Scanning Calorimetry

Distinct phase transition peaks were observed in DSC (Figure 4.5, Table 4.3). Surprisingly, a myriad of peak shapes (sharp, broad, split peaks), suppression in crystallization temperature, T_c, and changes in melting temperature, T_m, were observed in the BBcP samples. To properly assess the variety of crystallization/melt behavior, the time (and temperature) progression of ΔH_c and ΔH_m for PE and PCL phase transitions were considered independently and shown in Figure 4.6.
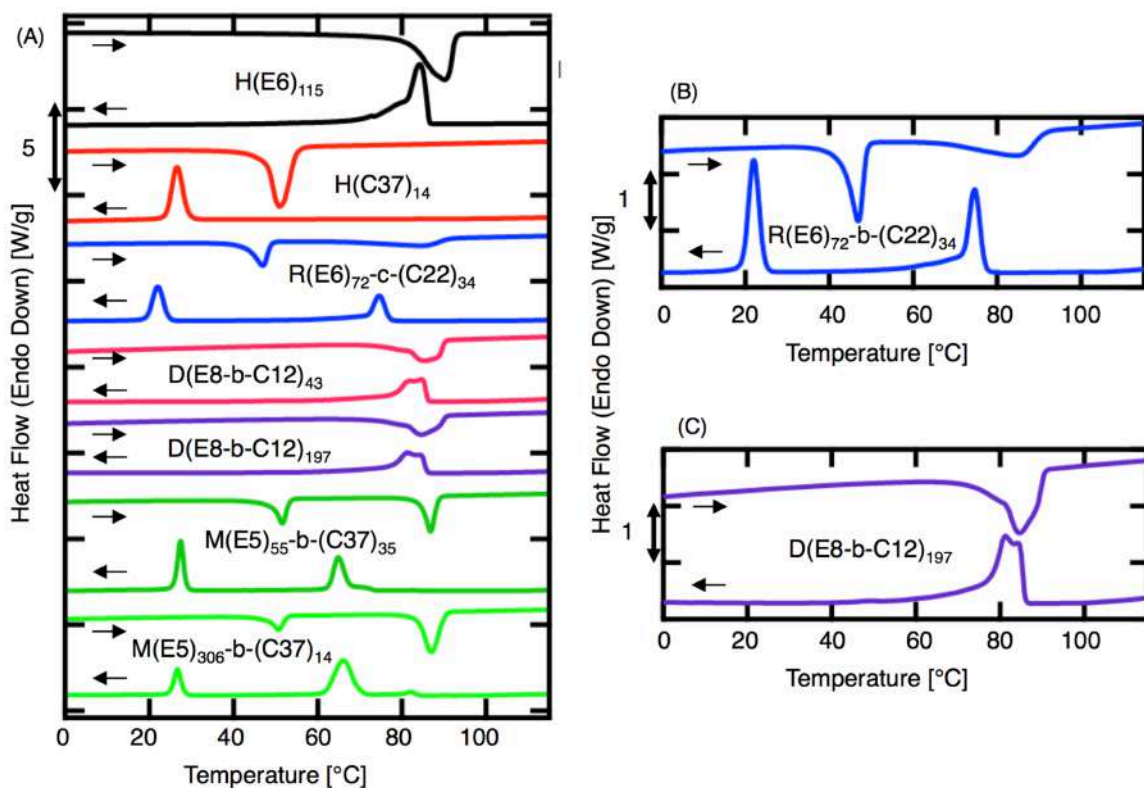
Figure 4.5. DSC thermograms of bottlebrush copolymers. (A) The DSC thermograms for cooling and heating (indicated by arrows) for all samples studied in this work on the same axis for scale. (B) The broad peaks observed are emphasized for (B) R(E6)72-c-(C22)34 and (C) D(E8-b-C!2)197.

Cooling from the melt, PE crystallizes before any PCL phase activity is observed. H(E6)$_{115}$ begins to crystallize at T_c=87°C as seen in Figure 4.6A. Despite R(E6)$_{72}$-c-(C22)$_{34}$ containing the same E6 units, the onset of crystallization is T_c=77°C, 10C lower

than that of H-Type. Although D(E8-*b*-C12)$_x$ shows onset of ethylene crystallization matching H(E6)$_{115}$, this is an unexpected result due to the longer length of E8 units – the T_m of E8 wax is roughly 15.8°C higher than E6 wax. Both M-Type samples show initial crystallization activity at 82°C; however, the main crystallization is delayed until approximately T_c=65°C, showing qualitative difference in crystallization compared to H-Type.

Table 4.3. Summary of DSC results. For comparison, 100% PE crystal $\Delta H°_{m,PE}$=293±14 J/g and $\Delta H°_{m,PCL}$=139.5J/g.

	Polyethylene (E)				Polycaprolactone (C)			
Sample	T_c [°C]	T_m [°C]	$\Delta\hat{H}_m$ [J/g]	$\Delta\hat{H}_{m,PE}$ [J/g$_{PE}$]	T_c [°C]	T_m [°C]	$\Delta\hat{H}_m$ [J/g]	$\Delta\hat{H}_{m,PCL}$ [J/g$_{PCL}$]
H(E6)$_{115}$	84.3	90.3	129	156	-	-	-	-
H(C37)$_{14}$	-	-	-	-	26.6	50.8	56.1	57.7
H(C37)$_{35}$*	-	-	-	-	26.1	51.5	58.8	60.4
R(E6)$_{72}$-*c*-(C22)$_{34}$	74.7	85.4	41.3	148	22.1	47.0	39.5	57.5
D(E8-b-C12)$_{43}$	84.5	85.5	85.9	257	-	-	-	-
D(E8-b-C12)$_{197}$	84.4	84.7	90.9	272	-	-	-	-
M(E5)$_{55}$-b-(C37)$_{35}$	64.9	86.8	42.3	296	27.4	51.5	36.9	46.7
M(E5)$_{306}$-b-(C37)$_{14}$	66.1	87.1	62.6	104	26.7	50.7	21.1	79.6
E8-b-C12*	85.7	87.0	66.9	201	7.0	28.0	21.5	35.2

To properly compare the PE crystal nucleation and propagation, the traces in (A) were normalized by ϕ_{PE} with a horizontal offset with matching crystallization onset in Figure 4.6B. Despite the suppression in T_c, R(E6)$_{72}$-*c*-(C22)$_{34}$ showed nucleation and propagation profile were nearly identical to H(E6)$_{115}$. Both D(E8) showed similar nucleation and propagation profile similar to H(E6)$_{115}$ except a slightly higher ΔH_c. Most surprising are the M(E5)$_x$-*b*-(C37)$_y$ samples. First, the delayed PE crystallization is emphasized in the inset of Figure 4.6A. Second, ΔH_c for M(E5)$_{55}$-*b*-(C37)$_{35}$ is substantially higher than H-Type, whereas M(E5)$_{306}$-b-(C37)$_{14}$ is much lower than H-Type.
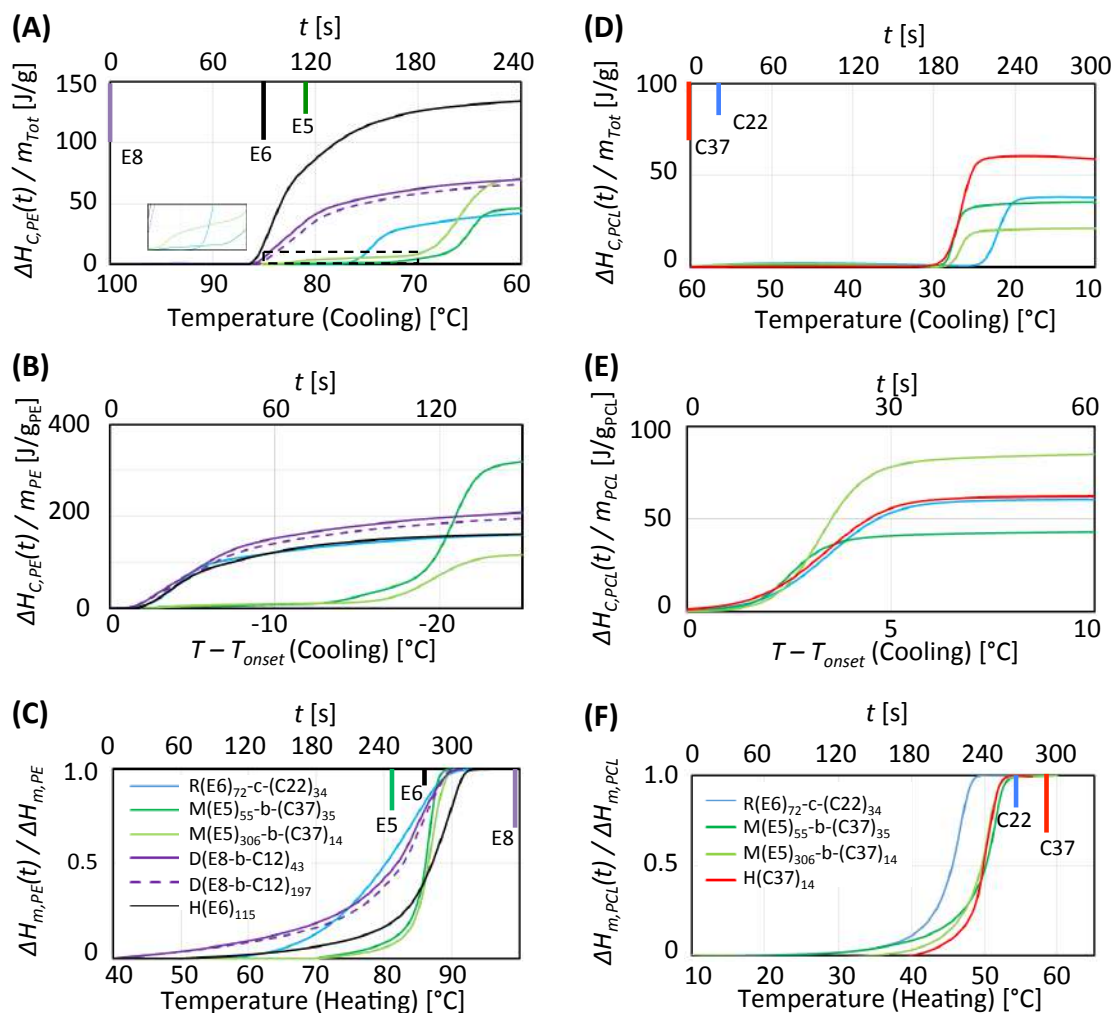
Figure 4.6. ΔH progression with time/temperature for semi-crystalline bottlebrush copolymers. DSC exotherms in the $T_{c,PE}$ temperature range (A) normalized by total mass of sample, (B) normalized by mass of PE component with a time shift to match onset of crystallization. (C) DSC Endotherm normalized by total ΔH_m in the $T_{m,PE}$ temperature range. (D), (E), and (F) analogues for (A), (A), and (C) respectively, for the PCL phase transition temperature range.

Following PE crystallization, PCL crystallizes as the sample is cooled (Figure 4.6D and E). Contrary to the observation of PE crystallization, PCL crystallization across the different connectivities shows similar behavior. All samples with C37 units crystallize between 26-27.5°C. Although R(E6)$_{72}$-c-(C22)$_{34}$ has a lower T_c, the difference can be accounted for by the shorter caprolactone units (Figure 4.6E). Unexpectedly, D(E8-b-C12)$_{43}$ and D(E8-b-C12)$_{197}$ samples do not exhibit C12 crystallization even at temperatures down to -50°C, even though E8-b-C12 macromonomer shows C12 crystallization. Thus,

the crystallization suppression in D(E8-*b*-C12)$_x$ is due to specific bottlebrush connectivity, and not length of C12 unit nor the block copolymer nature.

When the samples, now PE-PCL crystallized, are heated, PCL crystals are the first to melt (Fig. 4.6F). Similar to PCL crystallization, the melting profiles show uniform and qualitative similarities. The difference in the T_m of C°22 relative to C37 can be explained by the shorter length of C22 compared to C37. Again, no PCL phase activity was observed on the heating.

Further heating of the samples leads to melting of PE crystals (Fig. 4.6C) where each connectivity exhibits different melting behavior. The most striking result is the broad melting profile of R(E6)$_{72}$-*c*-(C22)$_{34}$, which shows a profile with no sharp increase in ΔH_m. In addition, the T_m was 9.6°C lower than H(E6)$_{115}$. For D(E8-*b*-C12)$_x$, the melting profile shows similar behavior as H(E6)$_{115}$. Despite the longer E8 units, which predicts an 15.8°C higher T_m, both D(E8-*b*-C12)$_x$ samples showed a T_m increase within 3°C relative to H(E6)$_{115}$, roughly 13°C much lower than expected. For M(E5)$_x$-*b*-(C35)$_y$ samples, a sharp PE melting profile is observed, showing a qualitative difference between the crystallization profile which showed a 2-step process. Despite the delayed crystallization, the T_m appears unaffected, resulting in a very large T_m-T_c.

4.4.2 *Variable Temperature Small Angle X-ray Scattering*

VT-SAXS provides structural insight into the broad spectrum of PE-PCL phase behavior in the 4 connectivities studied in this work (Figure 4.7). To start, H(C37)$_{35}$ shows a featureless pattern on cooling until about 23°C (consistent with T_c from DSC), where a correlation peak corresponding to a *d*-spacing=13nm in Figure 4.7A. The correlation peak persists until 55.3°C, consistent with T_m from DSC.

The black traces in Figure 4.7B show the anisotropy in R(E6)$_{72}$-*c*-(C22)$_{34}$ at room temperature through 1min acquisition times, where both PE and PCL have crystallized during a 10°C/min cooling rate. Along the direction of the max intensity, a primary peak with d_I=18.2nm is observed. Two additional peaks are observed at integer multiples of the

primary peak, consistent with a lamellar morphology. Orthogonal to the max intensity direction, only one correlation peak is observed, d_l=18.0nm.
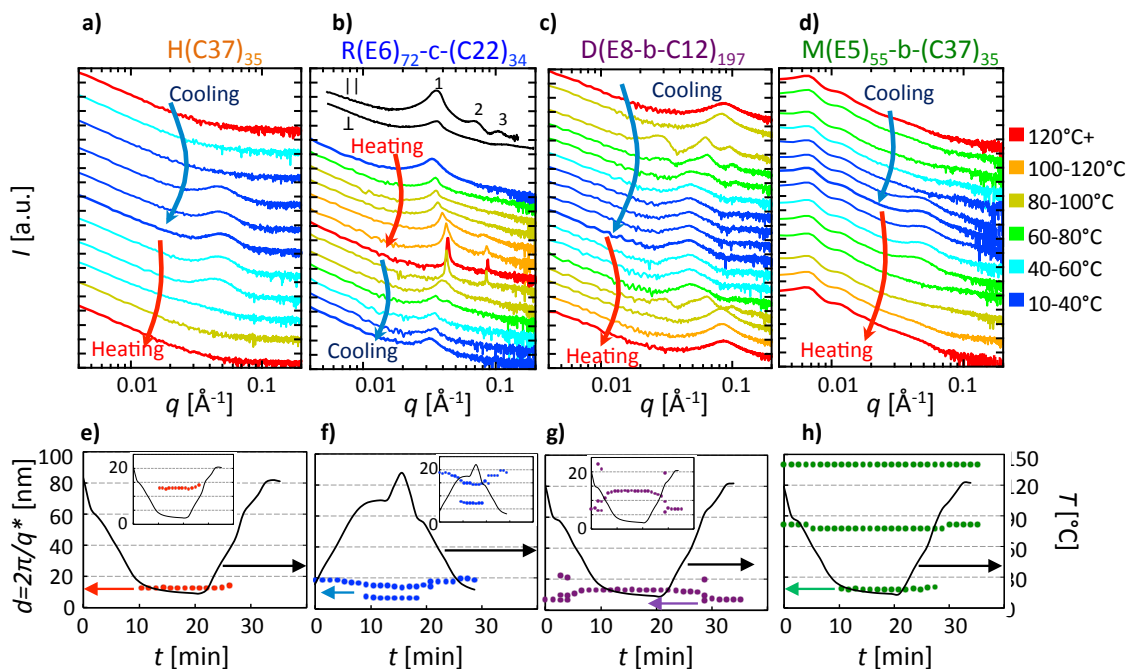
Figure 4.7. VT-SAXS Results. VT-SAXS patterns for a) H(C37)$_{35}$, b) M(E5)$_{55}$-*b*-(C37)$_{35}$, c) R(E7)$_{72}$-*c*-(C22)$_{34}$, and d) D(E8-*b*-C12)$_{197}$. The black traces in b) show the anisotropy of R(E6)72-*c*-(C22)34 at RT: top trace shows pattern along the max intensity of the primary peak, and the lower trace shows the pattern orthogonal to the max intensity. The corresponding *d*-spacings of peaks from a), c), c) and d) are on e), f), g) and h), respectively.

Upon heating R(E6)$_{72}$-*c*-(C22)$_{34}$, no significant change in *d*-spacing is observed in the temperature range that the caprolactone is expected to melt. However, at temperatures above 62.1°C, a gradual increase in *d*-spacing is observed beginning with 19nm (62.1°C) to 15.9nm (100°C). In the same temperature range, the orientation of the sample gradually changes shifts as can be seen in Figure 4.8. In the melt, a second peak emerges (*d*-spacing = 7.9nm) at an integer multiple of the primary peak. Upon cooling, the high-*q* peak disappears at 83.3°C, followed by an abrupt increase in *d*-spacing of the primary peak from 14.9nm (83.3°C) to 17.8nm (58.4°C). The *d*-spacing of 17.8nm persists until 34.0°C, and then another abrupt change to 19.0nm occurs.
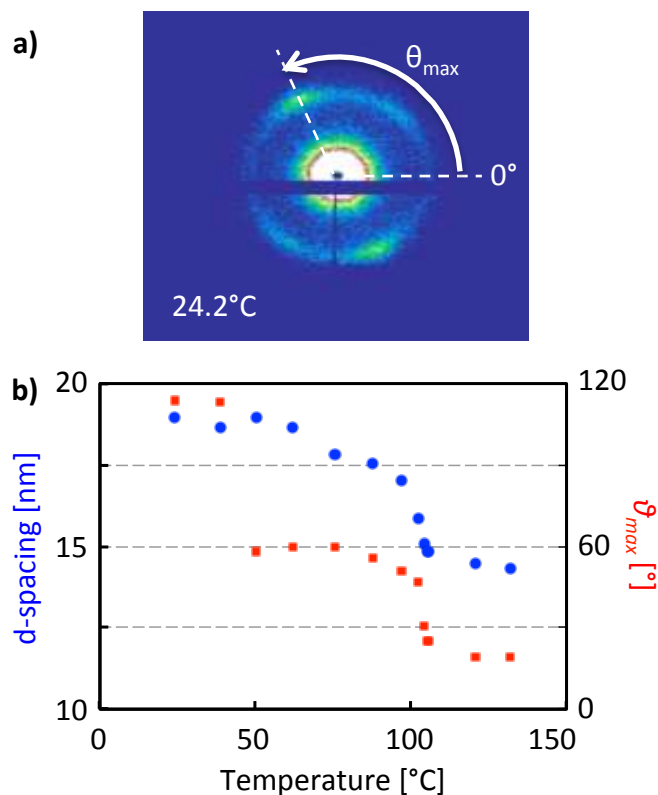
Figure 4.8. 2D SAXS pattern analysis. a) 2-D scattering pattern for R(E6)72-c-(C22)34 at 24.2°C showing the anisotropic scattering pattern and b) temperature dependence of the R(E6)72-c-(C22)34 primary peak d-spacing (blue, left) and scattering angle of the max intensity, θ_{max}, (red, right) during heating cycle.

In the melt phase at 120°C, D(E8-*b*-C12)$_{43}$ exhibits a single correlation peak corresponding to d_{corr}=7nm (Figure 4.7C). Upon cooling past the T_c, additional peaks emerge for T=86.2-76.2°C and then disappear, resulting in a single peak profile, d_{corr}=11.0nm. Further cooling shows a gradual change in *d*-spacing to d_{corr}=13.3nm by 38.0°C. Upon heating, the behavior that was observed during cooling is observed in reverse order. First, a gradual decrease in *d*-spacing is observed from 13.3nm (<30°C) to 11.6nm (74.8°C). Then, additional peaks emerge at 93.8°C, which quickly disappears. For T>93.8°C, a single correlation peak is observed with d_{corr}≈7nm.

In the melt phase at $T>T_{m,PE}$, $T_{m,PCL}$, M(E5)$_{55}$-*b*-(C37)$_{35}$ shows two which correspond to d_1=93nm and d_2≈53nm, length scales much larger than the other connectvities studied in this work (Figure 4.7D). These two peaks are observed for the full

temperature range studied in this experiment, 25<T<120°C. Upon crystallization of PE, a slight change in d_2 is observed to 52nm. For high-q (q>0.03Å), the behavior resembles H(C37) behavior. Featureless patterns are observed until T=26.4°C until a peak emerges corresponding to d_3=12.6nm. Upon heating, the peak is observed until 49.1°C.

4.4.3   *Transmission Electron Microscopy and Atomic Force Microscopy*

Microscopy images (AFM and TEM) reveal a diversity of structures and length scales (Figure 4.9). First, AFM phase image of H(C37)$_{35}$ revealed lamellar morphology with spacing of roughly 11-12 nm, consistent with SAXS results of d=13nm. R(E6)$_{72}$-*c*-(C22)$_{34}$ showed lamellar morphology with alternating stack sizes, ~11nm and ~6nm, for a total of 17nm. The sum of two stack sizes is consistent with the SAXS pattern which showed a primary peak position of d_1=19nm and reflection peaks at integer multiples of the primary peak. Height image in AFM revealed layers with 11nm step size, consistent with SAXS correlation peak with *d*=11nm. TEM images of M(E5)$_{55}$-*b*-(C37)$_{35}$ revealed unexpected results. Although SAXS and comparison to literature predicts lamellar phase, what we observed is an inverted phase – brick and mortar type. Inside the droplet domains, high degree of crystallinity can be observed. With less staining from RuO$_4$, the droplet phase is the PE phase. Surprisingly, the PE phase constitutes majority of the phase (nearly 87%) and the PCL, mortar, phase constituting the minority (nearly 13%), the opposite of the mass fraction in the sample.
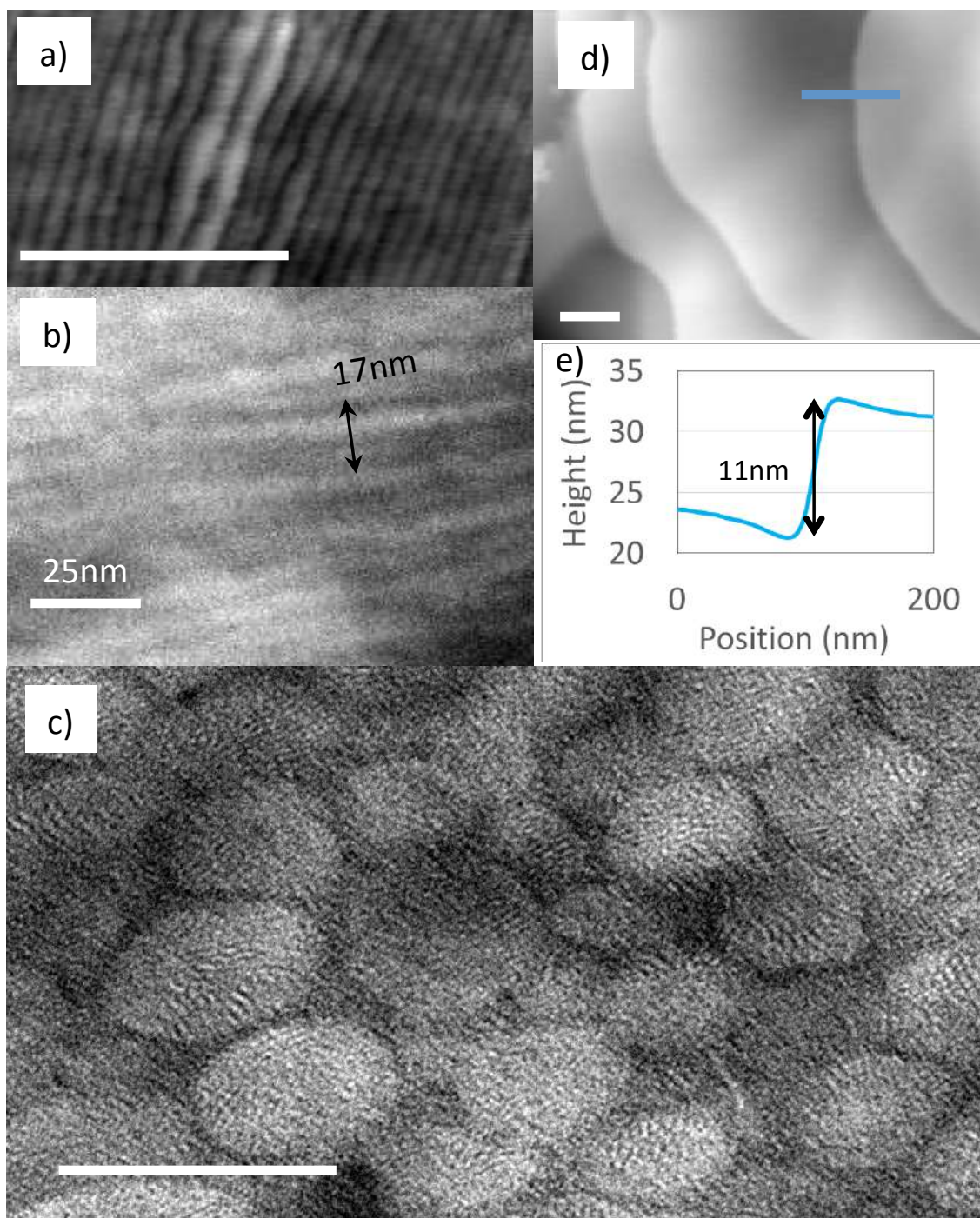
Figure 4.9. Microscopy analysis of self-Assembly and crystallization. a) AFM phase image of H(C37)35, b) TEM image of R(E6)72-c-(C22)34, c) TEM image of M(E5)55-b-(C37)35, d) AFM height image of D(E8-b-C12)197 and the corresponding e) height trace in blue. Scale bars are 150nm unless otherwise specified.

4.4.4 Variable Temperature Atomic Force Microscopy

To understand the non-expected crystallization and melting behavior of the D-Type, AFM images were taken to track the topological changes with melting (Fig. 4.10) at 10°C increments from 30-80°C. The surface area of the island feature as well as the topography along the three contours in the inset of Fig. VT-AFM (B) was tracked. What we observed were gradual changes in topography below T_m, whereas the surface area was relatively constant showing an anisotropic change in shape with temperature. As expected, a sudden jump is observed at the T_m in both quantities.
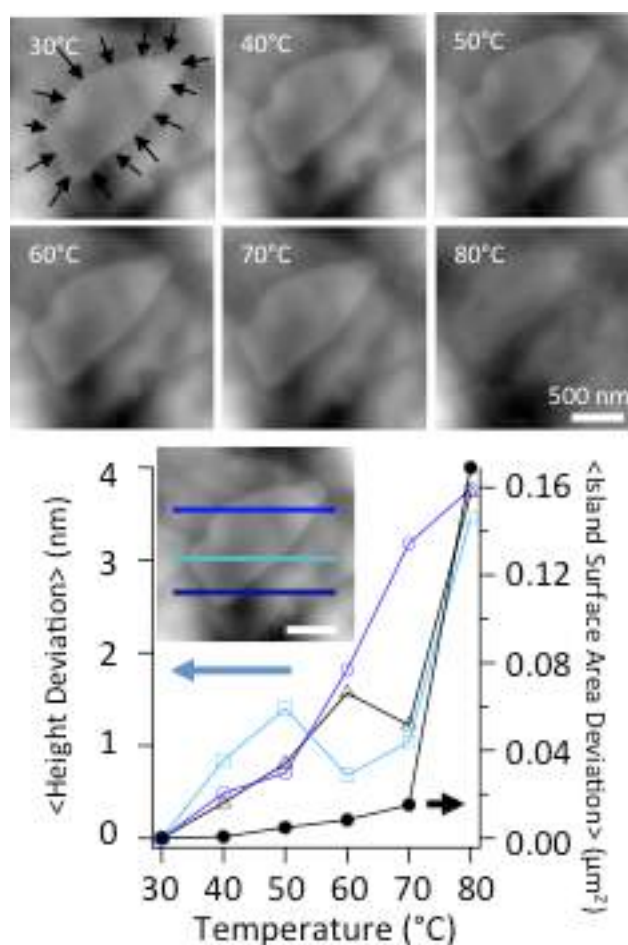
Figure 4.10.   VT-AFM D-Type topography analysis.   D(E8-b-C12)$_{197}$ height images from $30 \leq T \leq 80$°C. Deviations in the area of the island feature outlined by black arrows (black trace and right axis) and height from horizontal line scans (blue traces and left axis) are analyzed with temperature.

To gain additional insight into the broad melting observed for the PE component in R-Type, we look to the AFM phase image in Figure 4.11. AFM images were acquired during heating a sample cooled at 10°C/min from 120°C to mimic the condition used to obtain DSC endotherm. As can be seen, the phase image shows a gradual change from primarily light/gray (0.55/0.45) to predominantly dark image by 85-90°C showing no 'light' phase.

4.4.5   *Variable Temperature X-ray Diffraction*

With crystallization and phase separation as possible contributors to heat signatures in DSC, variable temperature XRD experiments showed polymer melting behavior at the peaks determined by DSC endotherms (Figure 4.12). Specifically, the origin of the broad DSC peaks, spanning up to 40°C, observed for R-Type and D-Type samples was the focus. By decomposing the XRD profiles into the amorphous and crystallization, the crystallization peak fraction, A_c/A_{tot}, can give an indication for the degree of crystallinity (Figure 4.13). The R-Type and D-Type samples show a gradual decrease in crystallinity as the sample is being heated. Thus, the broad melting observed for R-Type and D-Type samples has crystallographic origins.
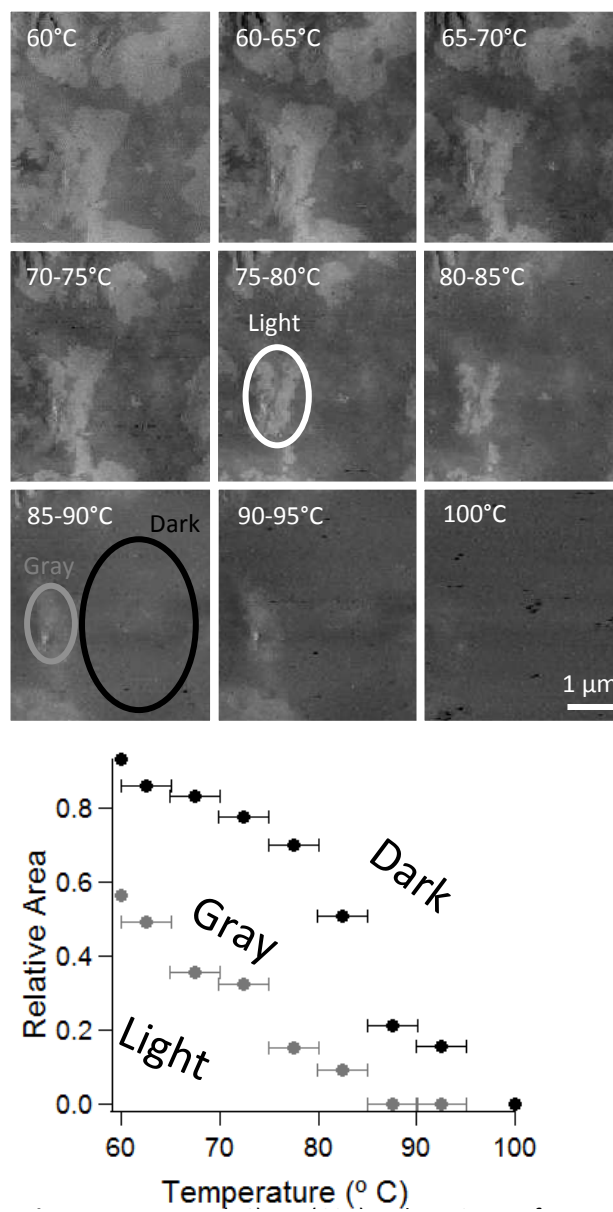
Figure 4.11. VT-AFM R-Type phase analysis. (A) AFM phase image of R(E6)$_{72}$-c-(C22)$_{34}$ during heating from 60°C to 100°C. The progression of phase transition from 'Light' to 'Dark' phase image is tracked in part (B).
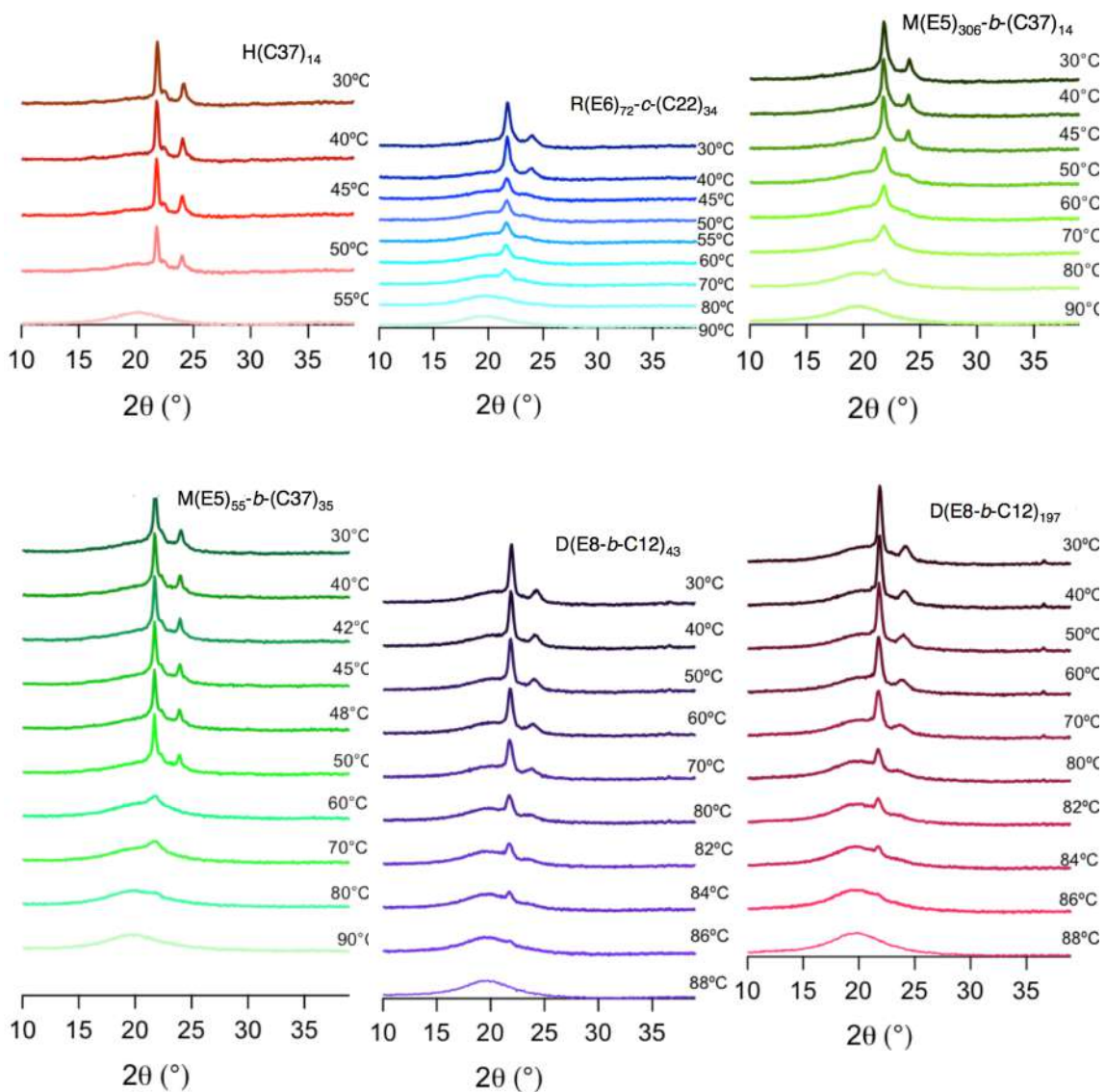
Figure 4.12. VT-XRD for bottlebrush copolymers. VT-XRD spectra for samples listed at the top for temperature range in which the samples showed melting behavior in through DSC.
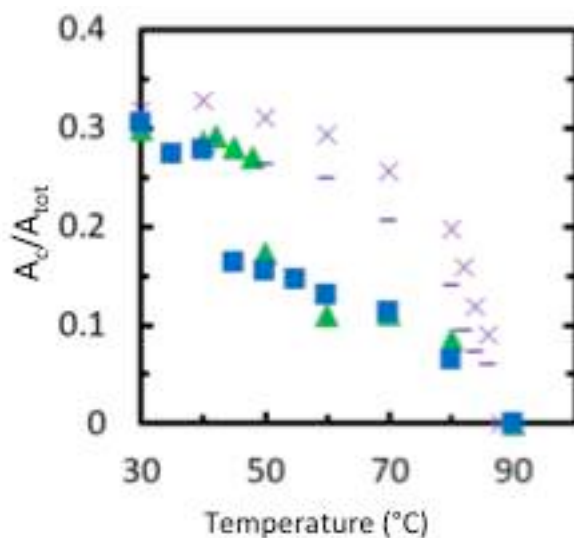
Figure 4.13. VT-XRD peak analysis. A_c/A_{tot} values from VT-XRD data for samples with broad melting features - R(E6)$_{72}$-c-(C22)$_{34}$ (blue square), D(E8-b-C12)$_{43}$ (purple X), and D(E8-b-C12)$_{197}$ (purple dash). For comparison, M(E5)$_{55}$-b-(C37)$_{35}$ (green triangle) characterized by sharp melting peaks is shown.

4.5   Discussion

With multiple crystallizable components and multiple connectivities, the combination of phases, morphologies, and variables to discuss in the respective phases can become overwhelming. To keep the analysis in focus, the following will be common focal points of all bottlebrush copolymer types: the main-chain position and orientation, crystal orientation (if any) with respect to the morphological interface (if any). Any additional key result will also be discussed.

4.5.1   Discussion – H-Type

4.5.1.1 $T > T_m$ - Melt

In the melt, no morphology is expected as f_{PNB} is very low and is completely surrounded by side-chains, preventing any organization of PNB chains (Figure 4.14), confirmed by VT-SAXS results showing featureless, and therefore homogeneous, system. The conformation of the bottlebrushes will be driven by configurational entropy. The specific single brush conformation in melts has received much attention in literature[51], and is beyond the scope of this work, so it will not be explicitly discussed.
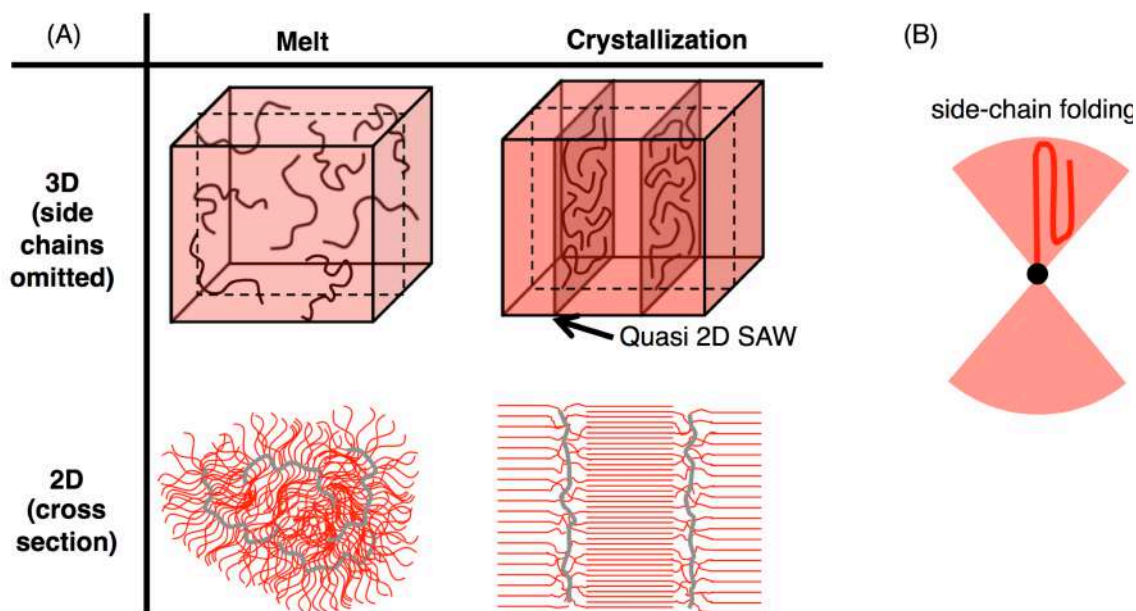
Figure 4.14 Schematic representation of H-Type. (A) 3D and 2D cross sectional schematic depicting the conformation of main-chain and side-chains in the melt and after crystallization. (B) A schematic viewing the axial direction of a main-chain showing the effect the chain-folding.

4.5.1.2 $T < T_m$ – Semicrystalline

Following side-chain crystallization, a quantitative analysis of the microscopy images show a lamellar spacing of roughly 11-13 nm. The spacing is also confirmed by the position of the peak in our SAXS data. Within the bottlebrush architecture, side-chain crystallization appears to drive a lamellar morphology, consistent with phase behavior observed in literature. The conformation of the main-chain is considered to be very elongated, without conclusive experimental evidence. Results by Xia[6] showed domain spacing to be commensurate of the fully extended contour length of the main-chain, but additional work as shown the equivalence to be from contribution of bottlebrushes from both ends as opposed to a single fully elongated bottlebrush. Here, we propose fundamental assessment of the main-chain conformation through consideration of the position of the chain stems. To form the lamellar morphology, the side-chains redistribute to opposite ends to form the crystallites, rendering the main-chain to occupy the interlamellar plane. Although restricting the main-chain position, as well as side-chain redistribution, comes at a high entropic cost, the enthalpic gain of side-chain crystallization

is more than sufficient for ordering. With the side-chain redistributed to opposite sides of the main-chain, the side-chains do not impose any resistance to bending along the direction of the interlamellar plane. Thus, we provide physical insight into the elongation of the main-chain, which will adopt a quasi-2D SAW.

Despite our observation of lamellar structure through microscopy image, the expected crystalline-lamellar reflection peaks are absent in our VT-SAXS data indicating irregularities in the lamellar stacks on long length scales. A possible cause of irregularity would be the presence of random chain folding. With the fully extended contour length of 37nm in the side-chains of $H(C37)_x$ samples, a noninteger value between 1 and 2 folds would lead to 11-13nm structures observed. The folds likely result in possible curvature as seen in (Figure 4.14B). Without external stimuli, chain folding occurs through random sampling of conformational space, likely leading to irregularities in chain tilt and overall morphology.

4.5.1.3   Reference Thermal Behavior

With short side-chains, the melting temperatures have not reached the asymptotic limit. Therefore, comparisons to literature values of asymptotically long PE and PCL T_m could result in erroneous conclusions. Instead, all comparisons of bottlebrush copolymer connectivities will be made to the H-Type and linear PE/PCL analogues.

4.5.2   R-Type

4.5.2.1 $T > T_{m,PE} > T_{m,PCL}$ - PE Melt and PCL Melt

When PE and PCL units are arranged randomly within the bottlebrush architecture, we observed unexpected stabilization of morphology, surprising crystallization behavior, and suppression of T_c and T_m of only the PE component. In the melt, the expectation was a disordered phase due to low segregation strength of the short side-chains. Surprisingly, the highest degree of ordering in R-Type was in the melt phase, showing a reflection peak at $q*$ and $2q*$, indication of lamellar morphology, with a domain spacing of 14.5nm. Alternating PE and PCL phases can be achieved through redistribution of the PE and PCL side-chains

to opposite sectors around the main-chain, in a similar fashion to H-Type (Figure 4.15). With the sum of PE and PCL length (6nm + 22nm = 28nm) being greater than the 14.5nm domain spacing, we can conclude that the side-chains are not fully extended, likely adopting a coil-like conformation in the melt phase. Now restricted to the interlamellar plane, the main-chain appears to act as an emulsifier to stabilize the formation of morphology when the segregation strength of the individual PE and PCL units were too weak, shown by the segregation strength of the hypothetical block copolymer.
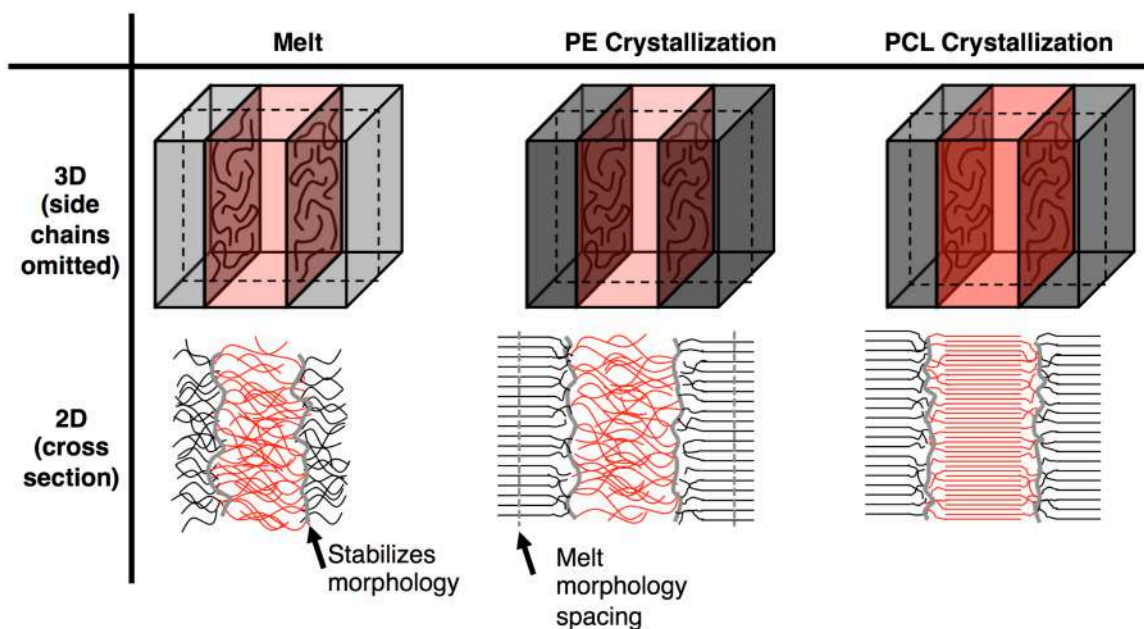
Figure 4.15. Schematic representation of R-Type. 3D and 2D cross sectional schematic depicting the conformation of main-chain and side-chains in the melt, PE crystallization, and PCL crystallization.

4.5.2.2 $T_{m,PE} > T > T_{m,PCL}$ - *PE Crystal and PCL Melt*

In the melt, we concluded random conformation of the side chains in the respective lamellar phases. As a result, significant conformational changes are expected upon crystallization of PE and, subsequently, PCL components, which requires polymer chains to be extended. In addition to the expected shift in the primary peak position to longer distances (to 17.8nm), the reflection peak had disappeared, indicating breakout PE crystallization, forming a disordered phase. The mismatch of the domain spacing to the PE crystal lattice dimension resulted in overriding of the pre-existing morphology in the melt.

Surprisingly, the shift in peak position does not occur as rapidly as expected, showing gradual transition over a >20°C range. The DSC exotherm displays a tail after crystallization. The SAXS data suggests the tail to be of morphological origin.

4.5.2.3 $T_{m,PE} > T_{m,PCL} > T$ - PE crystal and PCL Crystal

Upon PCL crystallization, PE and PCL both crystallization, an abrupt change in the peak position (to 19.0nm) is observed, signaling breakout crystallization. Our TEM image shows alternating stack of PE and PCL component of roughly 5-6nm and 11-12nm, respectively, for a domain spacing of roughly 17nm showing excellent agreement with our SAXS data. From the TEM analysis, we can conclude that chain folding is observed only in the PCL phase with a fully extended contour length of 22nm compared to the observed 11-12nm spacing for approximately 1 fold. Like H-Type, although lamellar morphology was observed in our microscopy images, SAXS reflection peaks are missing. However, when we consider the 2D-SAXS patterns, R-Type shows clear anisotropic behavior. At RT, sector averaged patterns reveal highly ordered lamellar morphology (peaks at q^*, $2q^*$, and $3q^*$) with a domain spacing of 18.2nm in the most oriented direction. In the direction orthogonal, all ordering is lost and a correlation peak corresponding to d=18nm is observed. The greatest orientation change occurs during PCL crystallization for two main factors: (1) the increase in density with crystallization and (2) chain folding. The former is observed for PE crystallization whereas the latter is not, leading us to believe chain folding to be the primary cause of 2D orientation. The anisotropic lamellar orientation suggests an increase in morphological correlation, relative to lamellar morphology for linear block copolymers, arising from the higher degree of polymer chain ordering from the bottlebrush architecture, offering internal stimuli for 2D ordering.

4.5.2.4   Kinetically driven phenomena (if any)

Even after discussing the chain conformation at each temperature regime, a glaring question still persists: why does PE exhibit a broad melting peak? VT-XRD and VT-AFM help us identify the origin. VT-XRD showed that the fraction of crystalline component does gradually decrease in the same temperature range as the broad melting peak,

confirming a crystallographic origin of the broad melting. However, VT-AFM shows a gradual phase transition in the same temperature range as the broad melting, confirming morphological origins. With high degree of morphological variation, domain spacing and orientation, the broad melting is likely due to kinetic limitations from deforming stable morphological structures on melting.

4.5.3   D-Type

4.5.3.1 $T > T_{m,PE} > T_{m,PCL}$ - PE Melt and PCL Melt

Out of all connectivities, PE and PCL units in D-Type were most affected by the connectivity. With low segregation strength, a disordered phase was expected in the melt and was confirmed by our VT-SAXS experiment. Surprisingly, the main-chain does not stabilize the formation of morphological structures as was the case in R-Type. The PCL block adds distance between the PE-PCL interactions and the main-chain preventing PNB from approaching the PE-PCL interface and immersed in the PCL side-chain (Figure 4.16). Therefore, the composition fluctuations are of PE rich and PNB/PCL rich regions. Although regular ordering is not observed, a correlation length of roughly 7nm was observed, which can impose kinetic restrictions on crystallization through limiting chain diffusion, and thermodynamic restrictions through surface effects which can increase the activation barrier for crystallization. The kinetic effects will be discussed in more detail in a later section.
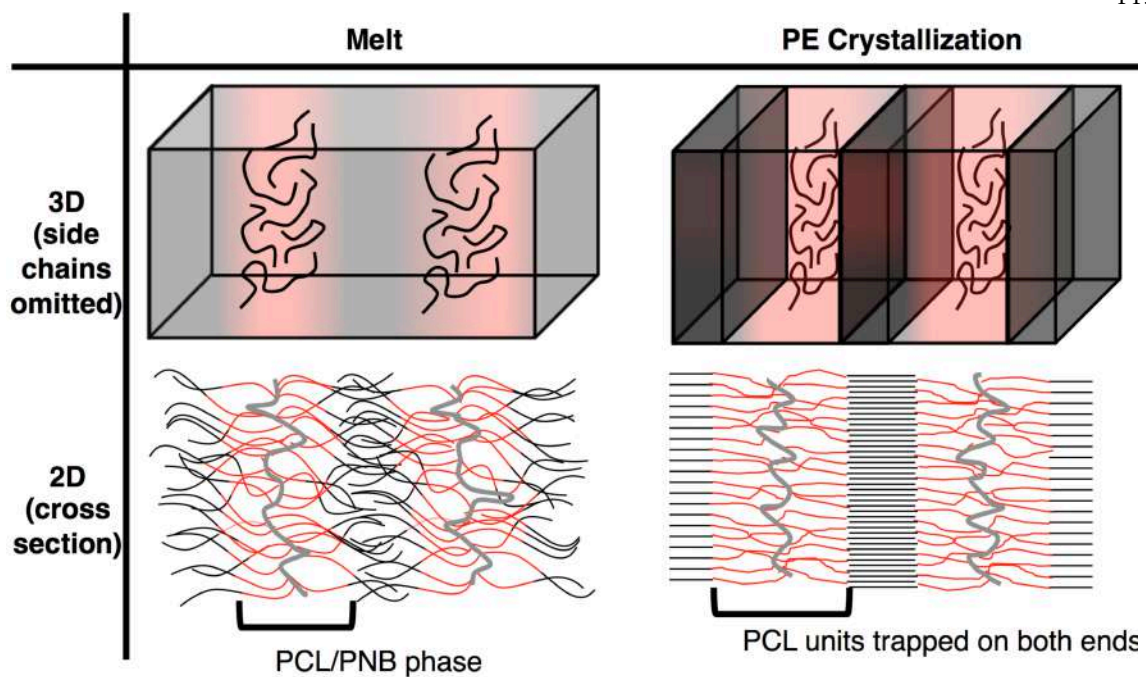
Figure 4.16. Schematic representation of D-Type. 3D and 2D cross sectional schematic depicting the conformation of main-chain and side-chains in the melt, PE crystallization.
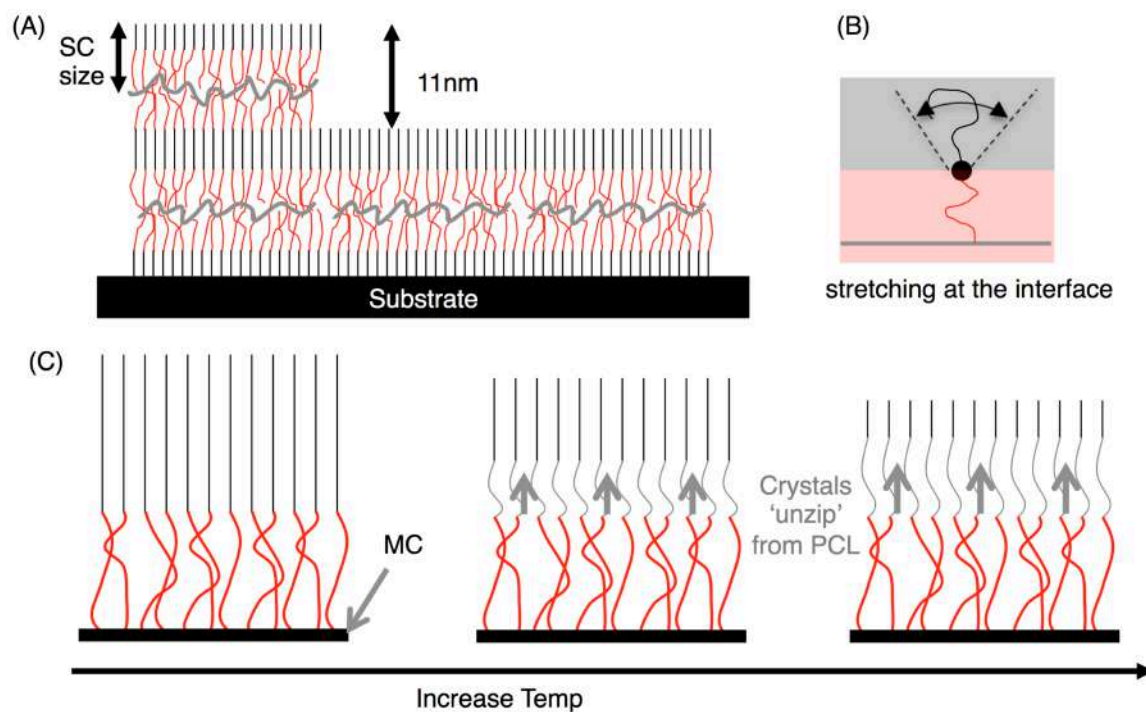
Figure 4.17. Schematic of additional D-Type Behavior. (A) Schematic representation of the topographical feature observed in AFM. (B) Schematic the 'stretching at the interface' phenomena leading to fast crystallization. (C) The 'unzipping' mechanism of PE crystal with increasing temperature.

4.5.3.2 $T_{m,PE} > T > T_{m,PCL}$ - PE crystal and PCL melt

Upon PE crystallization, island and step topographical features observed in AFM images indicate lamellar morphology of 11nm. For block copolymers, the step size correspond to a ½ or 1 domain spacing. With no phase contrast from the independent planes, the step size would correspond to a full domain length. It is tempting to also equate the step size to the size of the side-chain, but a comparison to the connectivity points to a faulty conclusion (Figure 4.17A). The domain space constitutes a PE crystal phase and a PCL phase. Contrary to H- and R-Types, the PNB main-chain does not lie in the interlamellar plane adopting a quasi-2D SAW. Instead, the PNB main-chain lies ½ the size of the PCL/PNB phase on average. Thus, the 11nm we observe would constitute the PE + PCL, but the size of the side-chain would be PE + ½PCL phase.

While PE component is driving crystallization, our SAXS results showed strong peaks which quickly disappeared, leaving a shifted correlation (13.3nm) in their wake. The crystallization is expected to drive formation of morphological structures; however, the mismatch in stem density to crystal lattice dimensions likely led to the formation of disordered morphology composed of thermally hindered PE crystals. The step size via AFM of 11nm and the SAXS peak position of 13.3nm are in good agreement, indicating a domain spacing of roughly 12nm. PE crystals would contribute roughly 7nm, almost the fully extended contour length, after allowing for some chain tilt and amorphous portions (90% of 8nm). The remainder would be the PCL and PNB amorphous phase.

4.5.3.3 $T_{m,PE} > T_{m,PCL} > T$ - PE crystal and PCL amorphous

One of the most striking results in this work was the complete suppression of PCL crystallization, even down to -60°C, where any heat signatures cannot be distinguished from the T_g. A look to the connectivity reveals that following PE crystallization, both ends of the PCL units become restricted: one end to the PE crystal and one end to the PNB main-chain (Figure 4.16). With random chain fluctuations in the melt, the PCL units are likely to be entangled and become kinetically trapped when PE crystallizes. With both ends confined and an entangled conformation, the PCL stems cannot form the lamellar

stacks required for polymer crystallization to occur. Consistent with the lack of features in the DSC for $T << T_{c,PE}$, SAXS results show no morphological changes in the same temperature regime.

4.5.3.4 Kinetic Effects

We expected the H-Type to have the 'fastest' (smallest T_m-T_c) for PE. However, we observed much faster, nearly reversible, crystallization in D-Type. Our VT-SAXS results reveal a correlation in the melt. Although an ordered morphology is not observed, the correlations would drive a conformational bias – for PE, the chains would be biased away from the PCL/PNB phase (Figure 4.17B). The biased alignment of PE chains is in a favorable conformation for crystallization, increasing the rate of crystallization.

Although the D-Type showed the 'fastest' crystallization with the smallest T_m-T_c, the melting temperature in the D-Type was the most suppressed out of all connectivities with respect to the linear analogue. This shows kinetics and thermal stability to be independent. In accord with the absence of ordered morphology after PE crystallization, the mismatch of stem density to crystal lattice spacing would reduce the thermal stability of PE crystals. Thus, portions of PE near the PE-PCL junction remain amorphous, also aided by thermal fluctuation of the PCL portion of the side-chain.

This leads to the discussion of the observation of the broad crystallization and melting peak. As the temperature is reduced, thermal fluctuations in PE and PCL units are minimized. Thus, with additional driving force for crystallization and reduced driving force for thermal fluctuation, additional PE units can continue to crystallize. The reverse behavior is expected for heating the sample from the crystallized state. This observation is confirmed by our VT-AFM analysis which shows much more significant deviations in the height of the island feature with temperature compared to the surface area of the island structure. The PE crystals are 'unzipping' (expect to change height) as opposed to stems melting away (expect to change the surface area) (Figure 4.17C).

4.5.4   M-Type

We begin our discussion of M-Type by making note of the unexpected inverted phase observed in the TEM image with PE forming the droplet phase and the PCL forming the continuous phase. Analyzing our experimental data without this knowledge would lead to erroneous conclusions since a typical linear block copolymer morphology exhibits the reverse behavior of the continuous phase made by the majority component and the droplet phase by the minority phase.
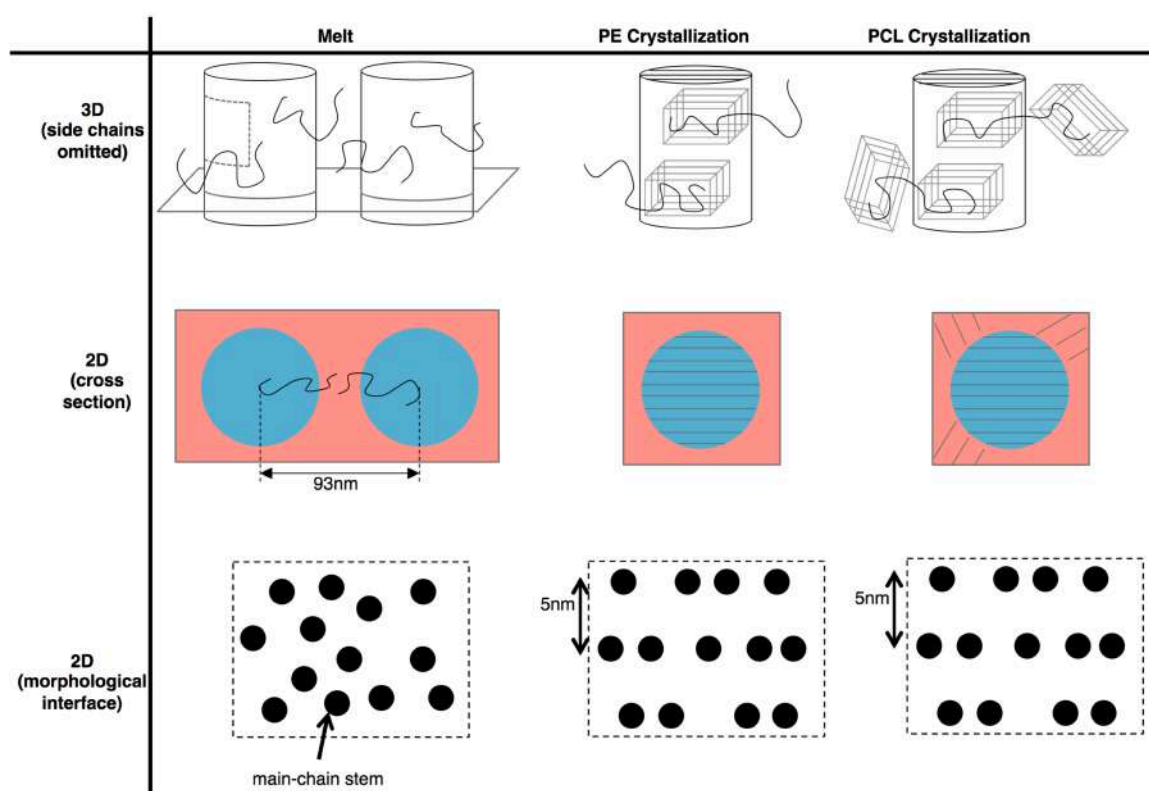
Figure 4.18. Schematic representation of M-Type. 3D and 2D cross sectional schematic depicting the conformation of main-chain and side-chains in the melt, PE crystallization, and PCL crystallization. We also show the chain-stem density at the morphological interface.

4.5.4.1 $T > T_{c,PE} > T_{c,PCL}$ - PE melt PCL melt

In the melt, we observed a strong primary peak (corresponding to length of 93nm) and a reflection peak of q* and √3q*, indicating a well-phase separated and ordered cylinders (Figure 4.18). The distinct morphology is consistent with observations literature

where the segregation strength is accumulated through the grouped side-chains driving phase separation even when the individual polymeric components lack sufficient driving force for phase separation. The domain spacing of 93nm is almost twice the fully extended contour length of the main-chain, indicating contribution from multiple bottlebrushes on the domain spacing. The main-chain is not expected to be fully extended, but would have an orientation bias perpendicular to the phase plane (Figure 4.18 row-2D cross section). The domain spacing is likely dictated by two bottlebrushes with some interdigitation – balanced by entropy and repulsion from the dense grafting.

4.5.4.2 $T_{m,PE} > T > T_{m,PCL}$ - PE crystal PCL melt

VT-SAXS results show minor morphological changes upon PE crystallization indicating confined crystallization, likely caused by the density change of crystallization and the ordering of the main-chain from crystallization. At high q, the SAXS profile does change, but no discernible features are observed. Like H-Type, the main chain of the PE sub-brush (portion of the bottlebrush in which PE side-chains are grafted) adopts a quasi-2D SAW, the ordering driven by the additional enthalpic gain from PE crystallization.

4.5.4.3 $T_{m,PE} > T_{m,PCL} > T$ - PE Crystal PCL Crystal

Our VT-SAXS results show a constant domain spacing after PCL crystallization. Due to the architectural similarity with the PE sub-brush, the identical crystallization effects on conformation are expected at a first glance. However, the PE crystals impose positional restrictions on the main-chain positions, forcing PCL crystallization to proceed in a manner unfavorable for PCL units of 37nm in length (Figure 4.18 row-2D morphological interface). Most notably, the PCL units want to crystallize at 13nm as the H-Type has shown, but the PE crystals, with 5nm fully extended contour length, formed at length scales incommensurate to the ideal for PCL units observed in the droplet phase of our TEM image.

Here, we discuss the possible origins of the inverted phase and the stabilizing mechanisms. A look at the relative lengths and number of PE vs. PCL units per main-chain

shows the mechanical difficulty in the PCL phase forming the droplet phase which f_{PCL}/f_{PE}=5.6 per stem. With this large mismatch, any curved interface would have PE in the concave side and PCL in the convex. Thus, the bottlebrush architecture plays a key role in the stabilization of the inverted phase as observed here. However, an important issue still needs to be addressed: in terms of relative volume/mass fractions, the PCL is the majority, but in the microscopy image, the PE phase occupies the majority of the area fraction, a blatant discrepancy.

A possible explanation would be that of an interconnected (perforated) lamellar morphology, similar to PL predicted by Wang et al.[80] (Figure 4.1). As shown by Bolton et al.[56], the asymmetric side-chain lengths would drive a curved morphology (favoring PE droplets) while the relative main-chain lengths drives lamellar morphology (Figure 4.19). In addition, the density increase during PE crystallization would be replenished by the amorphous PCL units. With all these factors, a perforated lamellar in the melt could be plausible. Unfortunately, additional scattering experiments would be required to say with certainty. With a perforated lamellar morphology, a cross section through the PE-rich and PCL-minor phase could explain the TEM image obtained. With large domain spacing (~100nm) with respect to the cross section thickness (50nm), a section through the PE rich phase could be isolated.
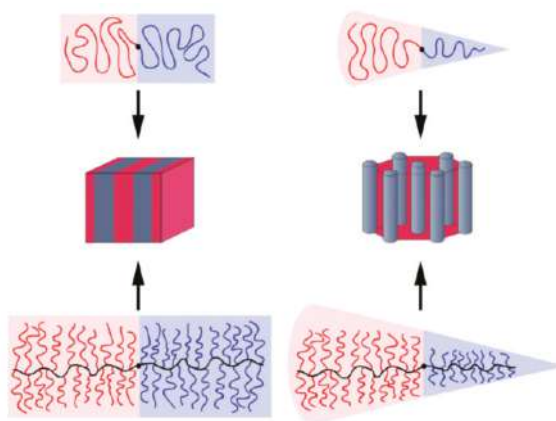
Figure 4.19. Effect of side-chain asymmetry on morphology. A schematic representation of side-chain length asymmetry in bottlebrush block copolymers (M-Type) on the morphology. [Adapted from reference 74]

4.5.4.4   Kinetic effects

A very surprising result is the delayed crystallization of PE without affecting the thermal stability, the opposite trend observed in D-Type. In the melt, the bottlebrush is free to adopt an entropically favorable conformation balanced by the orientation bias perpendicular to the morphological interface.   PE crystallization drives significant restructuring of the bottlebrush, favoring the alignment of PE sub-brush into interlamellar planes. However, the PCL sub-brush resists the ordering due to the entropic driving force for random conformation, offering kinetic delay in the propogation of PE crystals. As can be seen in Figure 4.6A, nucleation events do occur at the expected temperature.   The thermal stability remains unperturbed due to the crystal-lamellar orientation. As can be seen in Figure 4.18, the connectivity facilitates the formation of PE crystals with the crystal stem along the direction of the lamellar interface. The kinetic hindrance did not affect the lamellar thickness of the crystal structure – the factor determining the thermal stability. Although delayed, when the crystal forms, the crystal structure is identical to that observed in H-Type. This delay is absent in for PCL crystallization because the PE crystals are very rigid. Nucleation and propagation of PCL will proceed as is if grafted onto a surface.

4.6   Summary

To summarize, the bottlebrush architecture is shown to affect the morphology structure/stabilization, crystallization behavior and, independently, the melting behavior compiled in Table 4.4. Morphology stabilization was observed for R- and M-Type in the melt, but not in the D-Type. The length scales and the morphological structure do differ with R-Type showing lamellar structure with spacing dictated by the side-chain length whereas M-Type shows cylinders with domain spacing dictated by the main-chain length. Upon PE crystallization, significant breakout crystallization was observed for R- and D-Type as opposed to M-Type which only showing minor restructuring of the morphology. The R-Type showed a loss of the lamellar structure with an increase in the correlation length.   The D-Type briefly showed the formation of morphological structure but immediately disappeared, leading to a disordered but correlated structure with a longer

length scale. The increase in spacing is likely due to the extended conformation required to form crystalline lamellae. Upon PCL crystallization, R-Type shows significant breakout crystallization again, showing changes in spacing and anisotropic orientation. M-Type showed confined crystallization. For D-Type, PCL crystallization was completely suppressed.

Table 4.4. Summary of thermal and chain properties of bottlebrush copolymers.

	Polyethylene		Polycaprolactone		Orientation relative to interface	
	T_m-T_c	T_m-$T_{m,linear}$	T_m-T_c	T_m-$T_{m,linear}$	Main chain	Side chain
H-Type	6.0°C	~5°C	~24°C	~ -10°C	-	-
M-Type	~22°C	~6°C	~24°C	-10°C	Orthogonal	Parallel
R-Type	10.7°C	<1°C	~25°C	-9.7	Parallel	Orthogonal
D-Type	<2.5°C	~ -16°C	**None**	**None**	Parallel	Orthogonal

The suppression of PCL crystallization in D-Type was quite surprising, showing the level of impact the connectivity and architecture has on thermal behavior. For PE component, the stability of E crystals formed were linear>H-Type=M-Type>R-Type>D-Type. Surprisingly, the order of crystallization speed, T_m-T_c, in descending order is D-Type>H-Type=R-Type>M-Type. Surprisingly, D-Type showed the least thermally stable PE crystals, but were formed the fastest and the most thermally stable M-Type showed the slowest crystallization showing complete decoupling of thermodynamics and kinetics of crystallization. For PCL component, a much more homogenous behavior was observed with M- and R-Type showing comparable thermal behavior as H-Type. The only surprising result was the complete suppression of PCL crystallization for D-Type.

The myriad of morphological, crystal, and thermal behavior provides an expansive range of properties that can help us understand the interplay of morphology-crystallization chain stems. The results we observed could be explained by considering the orientation of the main-chain/side-chain with respect to the morphological interface. The main-chain orientation is orthorgonal, parallel, and parallel for M-Type, R-Type, and D-Type, respectively. In contrast, with side-chains extending radially from the main-chain, the side-

chains are oriented parallel, orthogonal, and orthogonal for M-Type, R-Type, and D-Type, respectively.

Chapter 5

CONCLUSION AND FUTURE WORK

5   Concluding remarks

5.1   Filling in the gaps of understanding

In Chapter 2, we were able to shed light on a controversy lasting over 2 decades – the conformation of bottlebrush polymers – through successfully obtaining the highly coveted scattering data with contrast matched side-chains. Between the two commonly ascribed models of wormlike chain/cylinder and SAW of superblobs, we showed that the wormlike chain, the more popular of the two, cannot describe the main-chain conformation, thereby correcting a big misconception in the field. Instead, the tension blob model through scaling arguments provides a better description for bottlebrush polymers in good and theta solvent (Chapter 3). On the way to our findings, we also discovered the extent to which the branches in branched structures can obscure the scattering patterns as the main-chain conformation was completely masked by the side-chains.

In addition, we identified two side-chain length regimes that helps reconcile some of the controversy that existed in literature. In addition, we offer an interpretation of the semidilute behavior that can explain the lyotropic phases observed in literature.

5.2   Self-assembly in solution

We observed the rich phase behavior (morphology and crystallization) with different polyethylene and polycaprolactone arrangement within the bottlebrush architecture (Chapter 4). Preliminary experiments of crystallization driven self assembly in 1% solution of deuterated xylene (Figure 5.1) hint at equally rich behavior in solution, in agreement with simulation results by Wang et al.
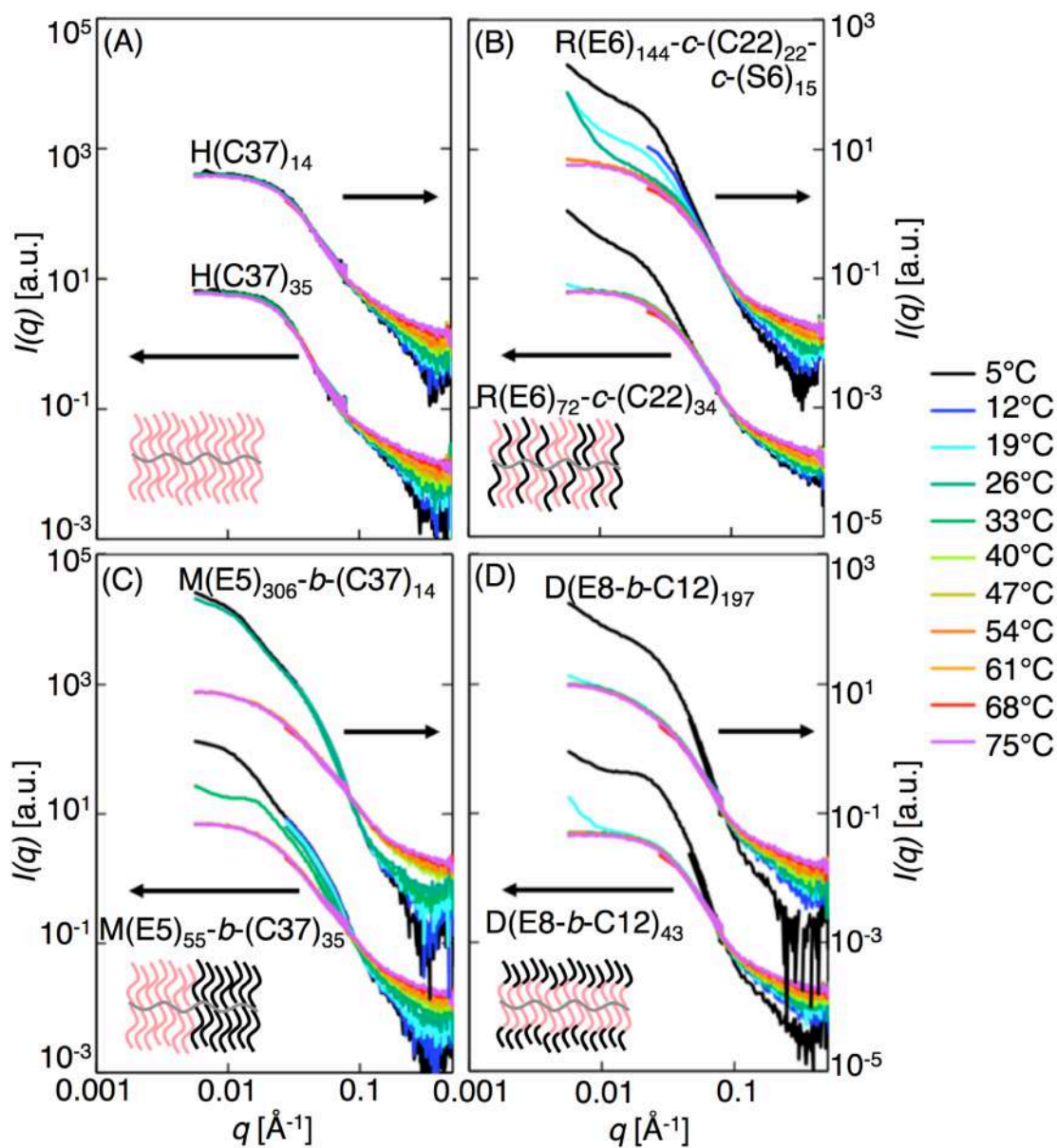
Figure 5.1. Crystallization driven self-assembly in solution of bottlebrush copolymers. SANS pattern of (A) H-Type, (B) R-Type, (C) M-Type, and (D) D-Type bottlebrush copolymers (Chapter 4) at c=1% from a temperature range of 5<T [°C]<75.

5.3   2D ordering of bottlebrush copolymer melts

The large domain spacing observed in M-Type bottlebrush copolymers (Chapter 4) led us to believe a long-range correlation of domains, a feature that can potentially removing the need for external fields to induce long range ordering of domains. Instead, surface energetics could drive 2D surfaces through large thickness without molecules

traversing through domains, stabilized by the large energetic penalty mixing through large domains.

APPENDIX

A   Polymer Physics background

Before discussing the unique behavior of the hierarchal structure of bottlebrush polymers, it is important to identify the characteristics and behavior of the individual substituents that make up bottlebrush polymers. Therefore, some basic physics of linear polymers[62] will be discussed before delving into the deviating behavior arising from the hierarchal arrangement defining bottlebrush polymers.

A.1   Polymer Conformations: Ideal Chains to Real Chains

Polymers are composed of small repeat units, monomers, connected by covalent bonds. The conformation a polymer chain undertakes is not a random assortment of points but is restricted by molecular architecture (chemical makeup, length, and topology) and environmental interactions (solvent, adjacent polymer chains, and external field), and determined by minimization of the free energy. In factors relevant to polymers, the equilibrium conformation is the conformation, which maximizes the configurational entropy and minimizing the environmental interactions. Therefore, changing solvent conditions can be used to control the chain stiffness, external fields can be applied to control direction of orientation, and incompatible materials can be covalently linked to form self-assembled structures. In an effort to describe and predict conformational behavior, numerous models have been developed. A few basic models will be discussed here.

The conformation of an ideal polymer chain composed of N monomer units with bond length b can be described by the bond vector, $\mathbf{r_i}$, directed from atom n_{i-1} to atom n_i.

With this information, we can calculate a relative length scale, the end-to-end distance, $\boldsymbol{R}_{e-e}$, which is the sum of all bond vectors

$$\boldsymbol{R}_{e-e} = \sum_{i=1}^{n} \boldsymbol{r}_i. \tag{A.1}$$

Bond vectors are expected to change with thermal motion and fluctuations leading to a distribution of $\boldsymbol{R}_{e-e}$ attainable by a given polymer chain. Therefore, it is more convenient to discuss properties regarding the ensemble average, denoted by $\langle \rangle$, than for an instantaneous conformation. Under isotropic conditions, there is no bias for a given direction and

$$\langle \boldsymbol{R}_{e-e} \rangle = 0, \tag{A.2}$$

which does not provide any useful information. However, the mean-square value is nonzero, thereby providing a more meaningful property:

$$\langle \boldsymbol{R}_{e-e}{}^2 \rangle = \langle \boldsymbol{R}_{e-e} \cdot \boldsymbol{R}_{e-e} \rangle = \left\langle \left(\sum_{i=1}^{n} \boldsymbol{r}_i \right) \cdot \left(\sum_{j=1}^{n} \boldsymbol{r}_i \right) \right\rangle = \sum_{i=1}^{n} \sum_{j=1}^{n} \langle \boldsymbol{r}_i \cdot \boldsymbol{r}_i \rangle. \tag{A.3}$$

This leads to the discussion of the freely jointed chain model shown in Figure A.1, where $|\boldsymbol{r}_i| = l$ and there are no correlations between the bond vectors, such that

$$\langle \cos\theta_{ij} \rangle = \begin{array}{l} 1 \text{ for } i = j \\ 0 \text{ for } i \neq j. \end{array} \tag{A.4}$$

Using these relationships, equation 1.3 becomes
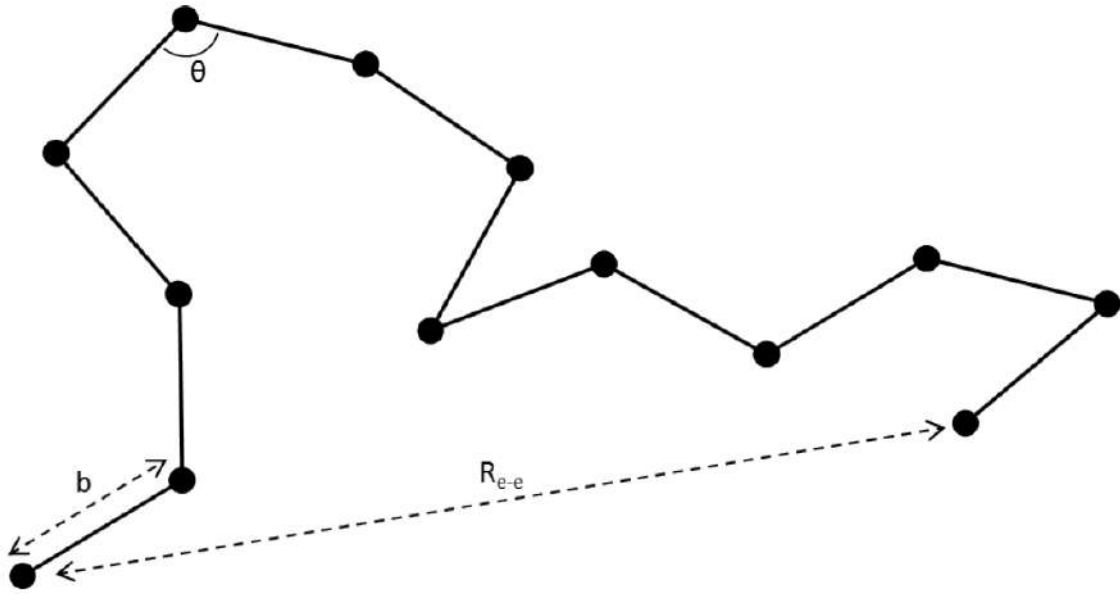
Figure A.1. Schematic of freely jointed chain. A schematic of the freely jointed chain with bond length l and bond angle $\boldsymbol{\theta}$. The end-to-end distance $\boldsymbol{R_{e-e}}$ is shown[60].

$$\langle \boldsymbol{R_{e-e}}^2 \rangle = \sum_{i=1}^{n}\sum_{j=1}^{n}\langle \boldsymbol{r}_i \cdot \boldsymbol{r}_j \rangle = l^2 \sum_{i=1}^{n}\sum_{j=1}^{n}\langle \cos\theta_{ij} \rangle = Nl^2. \qquad (A.5)$$

With this result, we have established a relationship between $\boldsymbol{R_{e-e}}$ and the architectural parameters N and l.

This is a very powerful result, but it does not capture certain characteristics that cannot be ignored for real systems. The freely rotating chain model, shown in Figure A.2, is an improved model taking into consideration fixed bond angles with equal probability in torsion angles, capturing bond angles in real systems. The correlations in bond vector are no longer zero, such that

$$\langle r_i \cdot r_j \rangle = l^2 (\cos\theta)^{|i-j|}, \qquad (A.6)$$
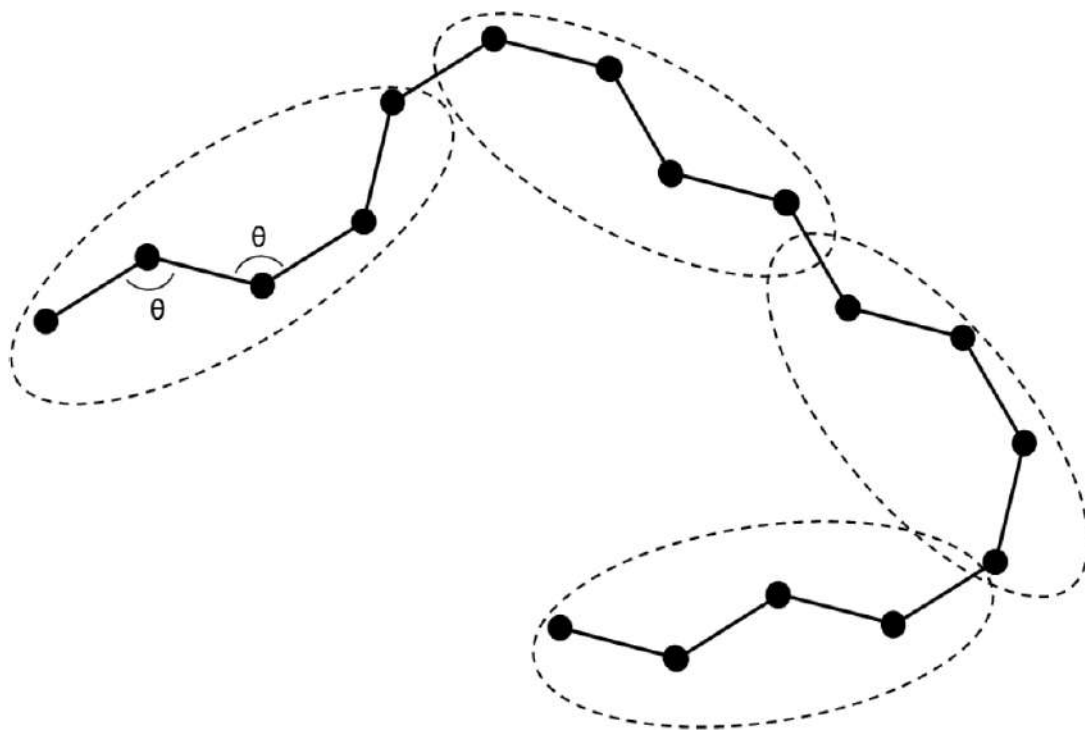
Figure A.2. Schematic of the freely rotating chain model. The bond angle θ is identical for all monomers. The dashed ovals represent a Kuhn segment where the bond correlation between segments disappears. These collection of Kuhn segments can be treated as a freely jointed chain[60].

with $(cos\theta)^{|i-j|}$ decaying rapidly with increasing distance between the monomers i and j. To quantify the scale of decay, it is helpful to express $(cos\theta)^{|i-j|}$ as an exponential

$$(cos\theta)^{|i-j|} = \exp[|i-j|ln(cos\theta)] = exp\left[-\frac{|i-j|}{s_p}\right], \qquad (A.7)$$

where s_p is the scale at which correlation between bond vectors decays. Defined as the persistence segment, s_p is the number of monomers within a segment that has not lost correlation

$$s_p = -\frac{1}{\ln(cos\theta)}. \qquad (A.8)$$

Thus, s_p is often used to define stiffness/flexibility of real polymer systems.

With the rapid decay, the result obtained from equation A.3 differs by that of a constant, C_∞, as shown below

$$\langle \boldsymbol{R}_{e-e}{}^2 \rangle = \sum_{i=1}^{n} \sum_{j=1}^{n} \langle \boldsymbol{r}_i \cdot \boldsymbol{r}_j \rangle = \frac{1 + \cos\theta}{1 - \cos\theta} Nb^2 = C_\infty N l^2. \tag{A.9}$$

C_∞ is known as Flory's characteristic ratio and can be a measure of the chain stiffness as discussed by the equivalent freely jointed chain (FJC) model. In the FJC model, the polymer chain can be grouped into segments, called Kuhn segment, N_k, with length, l_k, such that successive Kuhn segments do not correlate, $\cos\theta_{ij} = 0$. Therefore, the scaling for $\boldsymbol{R}_{e-e}$ can be written in the same was as for a freely jointed chain

$$\langle \boldsymbol{R}_{e-e}{}^2 \rangle = N_k l_k{}^2. \tag{A.10}$$

These terms can be evaluated using the contour length, $L = N_k l_k = Nl$, and using the $\boldsymbol{R}_{e-e}$ relationships. We can determine

$$l_k = C_\infty l, \tag{A.11}$$

and

$$N_k = \frac{L}{l_K}. \tag{A.12}$$

Also, we can define the persistence length, l_p, a length scale at which the correlations between bond vectors decays. For polymers with small bond angles, $\cos\theta$ can be expanded about $\theta = 0$ to show the following relationship between l_p and l_k

$$l_k = 2l_p. \tag{A.13}$$

Since N_k was designed to represent the number of units required for the bond vector correlations to cease, this value can be used as a basis to categorize the stiffness of polymers of interest. Polymers with $N < N_k$, or equivalently $b < l_k$, can be treated as stiff rods, i.e. $\langle \boldsymbol{R}_{e-e} \rangle = L$. The freely jointed model holds for polymers with $N \gg N_k$, or

equivalently $l \gg l_k$, i.e. $\langle R_{e-e}^2 \rangle = N_k l_k^2$, but polymers between these two regimes require a more detailed approach such as the wormlike chain model.

A.2   Worm-like chain (Kratky-Porod) model

Wormlike chains (WLC), also referred to as the Kratky-Porod Model, are a special case of a freely rotating chain with very small bond angles such as double-stranded DNA. When polymers are stiff, another mode of flexibility plays a key factor. Bends along the polymer chain contour, in addition to the trans-gauche bond rotation determine the flexibility of the polymer. For small bond angles

$$\cos(\theta) \cong 1 - \frac{\theta^2}{2},$$
(A.14)

and

$$\ln(\cos(\theta)) \cong -\frac{\theta^2}{2}.$$
(A.15)

Thus, the persistence segment, s_p can approximated as

$$s_p = -\frac{1}{\ln(\cos\theta)} \cong \frac{2}{\theta^2},$$
(A.16)

with the persistence length, l_p, defined as

$$l_p \equiv s_p l = \frac{2l}{\theta^2}.$$
(A.17)

Another consequence of small bond angles is a large characteristic ratio

$$C_\infty = \frac{1 + \cos\theta}{1 - \cos\theta} \cong \frac{4}{\theta^2}.$$
(A.18)

Using this relationship for the characteristic ratio, a relationship between the persistence length, l_p, and Kuhn length, b, can be derived:

$$b = \frac{lC_\infty}{\cos(\theta/2)} \cong \frac{4l}{\theta^2} = 2l_p. \tag{A.19}$$

In addition to small bond angles, $\theta \to 0$, WLC are defined for short chains with $L \ll l$ or $s \ll s_p$.

A.3   Radius of Gyration

The calculation of $\mathbf{R}_{e-e}$ is straightforward, but obtaining experimental measurements is quite difficult. In addition, this length scale is nonexistent for circular polymers and ill-defined for those with more complex architectures. These issues warrant the use of another length scale, the radius of gyration, R_g, or the average distance each monomeric unit is from the center of mass, described by

$$R_g = \left(\frac{1}{N} \sum_{i=1}^{N} (\mathbf{R}_i - \mathbf{R}_{cm})^2 \right)^{1/2}, \tag{A.20}$$

where $\mathbf{R}_i$ is the position vector for unit i and $\mathbf{R}_{cm}$ is the position vector of the center of mass of the polymer chain. The scaling behavior for R_g is identical to that in $\mathbf{R}_{e-e}$.

A.4   Solvent Quality

Experimental results showed that the derived scaling behavior was inaccurate, more specifically, real polymers scale faster than $R \sim N^{0.5}$. To explain this discrepancy, Flory suggested the idea of an excluded volume effect in which no two monomers can occupy the same space. This model became known as the self-avoiding-walk model. No analytical solution exists, but Flory derived a relationship by minimizing the free energy with respect to R and showed $R \sim N^{0.6}$, which is close to the experimental value of $R \sim N^{0.588}$. Further research showed that real polymers can exhibit the scaling relationship $R \sim N^{0.5}$ for an

ideal chain under different solvent conditions. To understand the monomer-solvent, interaction, we consider the following.

If we consider the energy to bring two monomers together, a potential similar to the Lennard-Jones potential can be constructed (Figure A.3). At small r, the Pauli exclusion (overlapping orbitals) prevents energy cost $U(r)$ of bringing two monomers from an infinite distance to r results from steric repulsion of overlapping monomers. At larger r, an attractive well is observed for the Lennard-Jones potential which considers Van der Waals interactions. Polymer samples in solution will exhibit attraction, repulsion, or no additional interaction depending on the solvent-monomer interaction. If the monomer-monomer interaction is more favorable than the solvent-monomer interaction, an attractive well for monomers is observed. This is referred to as a poor solvent (non-solvent at the limiting case). As the solvent-monomer interaction becomes more favorable than the monomer-monomer interaction, the attraction well continuously decreases until only the hard-core repulsion is observed referred to as the good solvent (athermal solvent at the limiting case). If the solvent-monomer interaction is more favorable than the monomer-monomer interactions, additional repulsion can be observed as well. The solvent condition at which the attractive well and repulsion balance is referred to as the θ solvent.

The mathematical formulation is as follows. The potential $U(r)$ can be used to calculate the relative probability of finding two monomers separated by r and at temperature T

$$B = \exp\left(\frac{U(r)}{kT}\right),$$
(A.21)

where k is the Boltzmann constant. At small r, $B=0$ indicative of the hard-core repulsion, at large r, $B=1$. A maximum can be observed depending on the magnitude of the attractive well. The Mayer-f function is defined as

$$f(r) = \exp\left(\frac{U(r)}{kT}\right) - 1 = B - 1. \qquad (A.22)$$

Using the Mayer-f function, an excluded volume parameter, v, can be calculated as follows

$$v = -\int f(r)dr^3. \qquad (A.23)$$

The excluded volume parameter quantifies the net two-body interactions between monomers. For an athermal solvent, where the solvent-monomer interaction is identical to the monomer-monomer interaction, $v>0$. As the solvent-monomer interaction becomes less favorable, v decreases and becomes $v<0$ for poor solvents until polymers precipitation is observed for nonsolvents. The transition from $v>0$ to $v<0$ is referred to as the theta temperature.

The effect of solvent-monomer interactions for different solvent conditions is schematically represented in Figure A.4. To determine the quantitative differences, we will consider the scaling for R_g with N: $R_g \sim N^v$. In good solvent conditions, the polymer-solvent interactions are more favorably than the polymer-polymer interactions. Solvent molecules surround polymer segments, leading to excluded volume interactions that result in an expanded conformation (Figure A.4 left). In poor solvent, the polymer-solvent interactions are less favorable than polymer-polymer interactions. This leads to solubility limitations, leading to precipitation of polymers. The transition between these two solvent qualities is the theta condition in which the polymer-solvent interactions are equal to that of the polymer-polymer interaction (Figure A.4 right). This condition is met at one temperature for a given solvent referred to as the theta temperature where the polymer is described by the random walk models, $v = 0.5$.
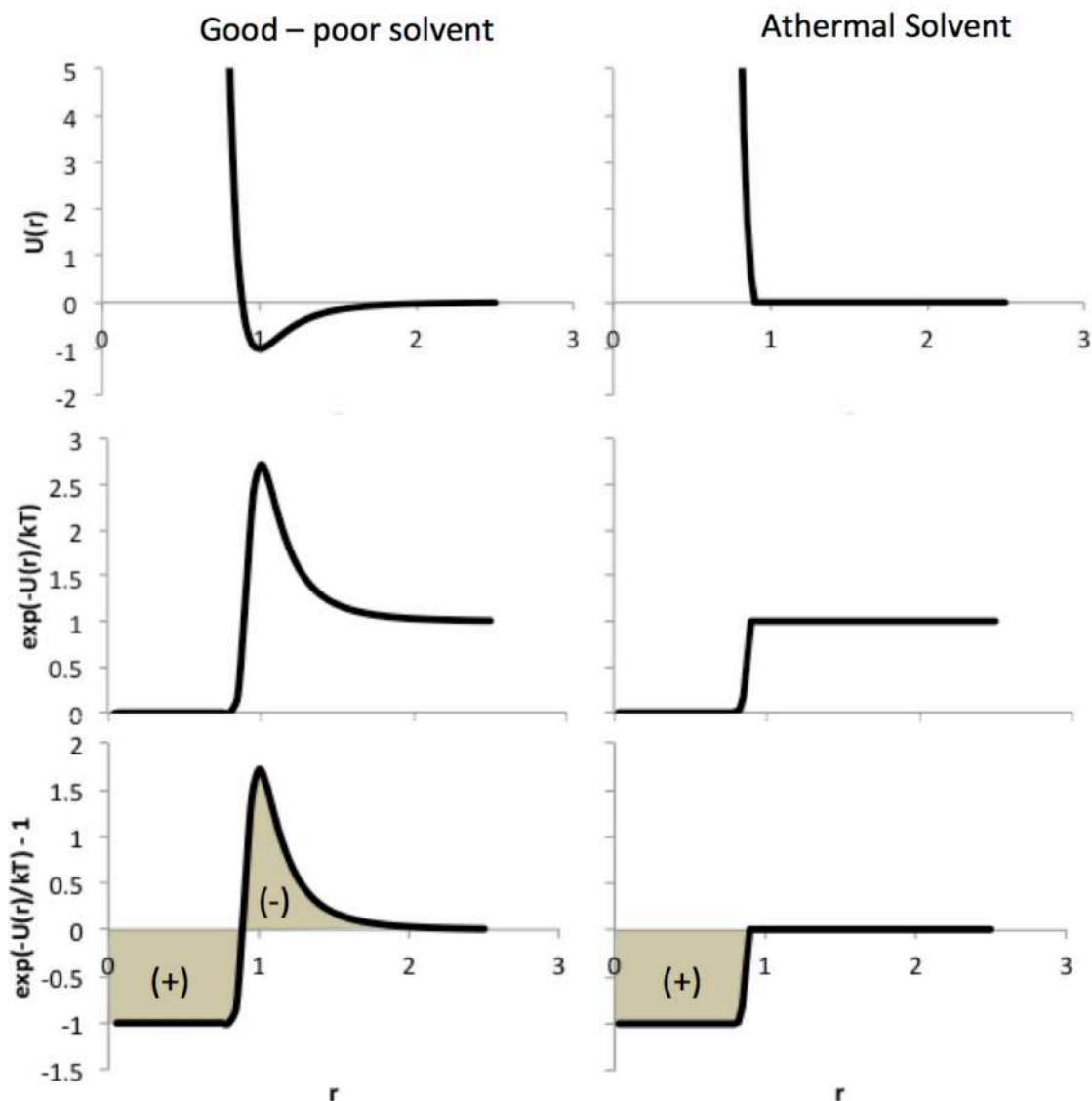
Figure A.3 Mayer-*f* function diagrams. Mayer-*f* function calculations with an attractive well for polymeric samples in poor to good solvent conditions (left) and with only the hard-core repulsion for polymeric samples in athermal solvent (right).

The derived scaling behaviors are consistent with ideal chains following Gaussian statistics, but can also be used to describe the behavior of real polymers as well. For dense melts and at the theta point, where repulsion from excluded volume is screened, the scaling behavior holds. But under good solvent conditions, the excluded volume interactions result in a faster expansion of polymers with size such that $v \approx 0.588$ instead of $v = 0.5$ for

$$R \sim N^{\nu}, \tag{A.24}$$

where R represents both R_g and R_{e-e} (this value represents the root-mean-square value). However, at small length scales, below the thermal blob size[16] ξ_T,

$$\xi_T \cong l_k \tau^{-1}, \tag{A.25}$$

for a good solvent, where $\tau = 1 - \theta/T$ describes the solvent quality, the thermal energy $\sim kT$ is much stronger than the repulsion from the excluded volume interactions and the chain behaves nearly ideal, $\nu = 0.5$.

A.5   Concentration Regimes

The discussions up to this point are valid for polymers below the overlap concentration in the dilute regime, where individual chains remain isolated. Above the overlap concentration, in the semidilute regime for good solvent, where the behavior can be described by concentration blobs[16] ξ

$$\xi \cong b\tau^{-1/4}\phi^{-3/4}, \tag{A.26}$$

where ϕ is the monomer volume fraction as shown in Figure A.5. It is important to note that ξ has a concentration dependence but ξ_T does not. At distances below the thermal blob size, the chain is nearly ideal ($\nu = 0.5$) because the excluded volume interactions are weak compared to the thermal energy. At distances above the thermal blob size but below the correlation blob size, excluded volume interactions dominate ($\nu = 0.588$). Scales larger than the correlation blob size have the excluded volume interactions screened by overlapping chains and can be described by a random-walk of correlation blobs.

Similarly, when densely grafted onto a flat surface at a grafting density of σ (chain per unit area), polymer chains overlap and screen the excluded volume interactions. In the Alexander-de Gennes brush, correlation blobs, determined by the surface grafting density, are used to describe the behavior as seen in Figure A.6. These blobs repel with energy

$\sim kT$ forcing the polymer chains to extend perpendicular to the surface. When polymers are grafted such that the neighboring chains do not interfere, they behave as surfactants, which Flory derived have the size

$$R \sim N^{3/5}b. \tag{A.27}$$

Therefore, when $\sigma \gg \left(N^{-3/5}\right)^2$, the polymers must extend perpendicular to the surface due to overlapping chains resembling the Alexander-de Gennes brush.
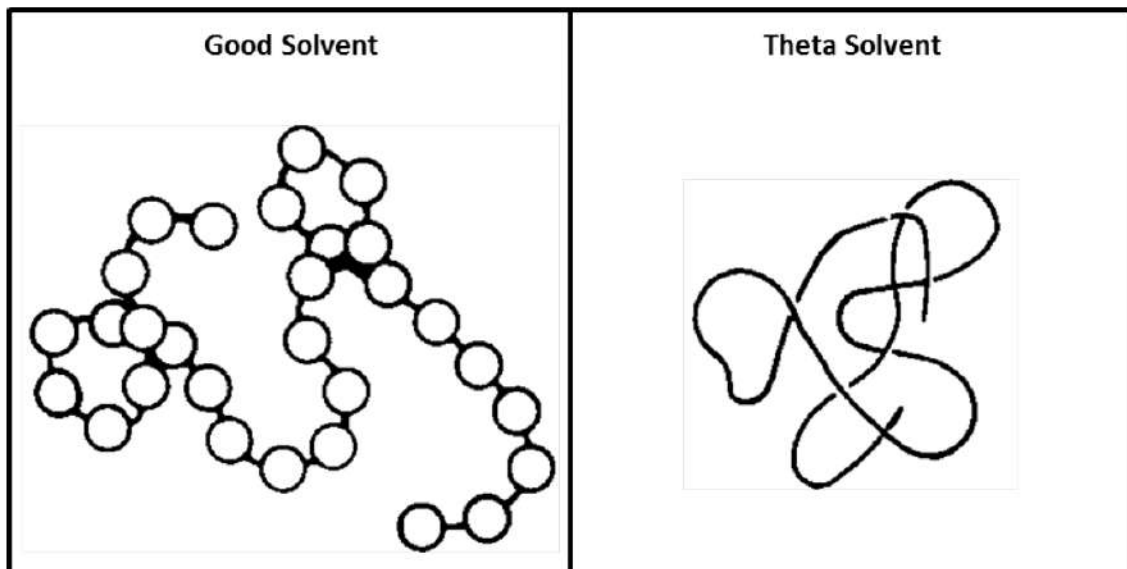
Figure A.4 Schematic of good and θ solvent. A schematic representing the excluded volume interactions present for good solvent conditions (left) but not for theta solvent conditions (right). The excluded volume interactions in the good solvent conditions require the SAW model.
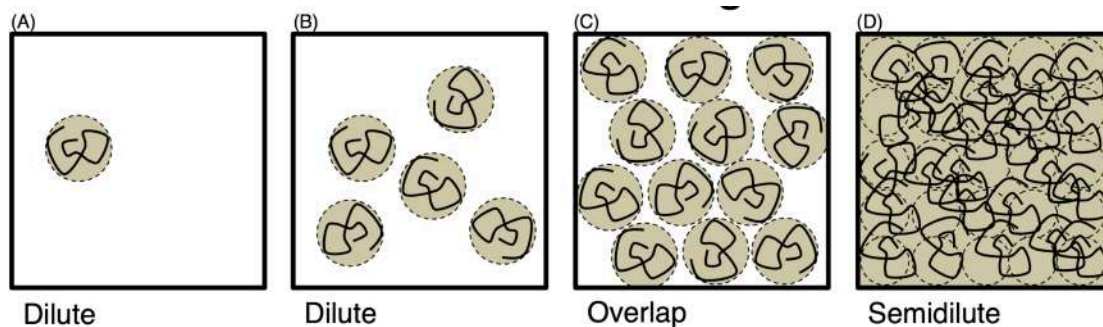
Figure A.5 Schematic of different concentration regimes: dilute regime (left) and the semi-dilute regime (right). The crossover between these two regimes occurs at the overlap concentration (middle). The dashed circles represent the pervaded volume of a polymer which scales as $V \sim R^3$ where R can be represented by the RMS end-to-end distance or the radius of gyration. There is an absence of dashed circles in the semi-dilute regime because the length scales are not well-defined in this regime.

A.6   Polymer Crystallization

Each monomer in the polymer can serve as a stereocenter, allowing for the numerous combinations of possible stereoisomers defining the conformation of the polymer chain. The free sampling of rotation at each stereocenter is typically a characteristic of an amorphous polymer. However, specific conditions (Temp, chemical interaction, etc.) can reduce the sampling space by driving spontaneous ordering into parallel/helically aligned structures. These structures have 3-D order resembling the crystalline state of monomeric systems. However, in nearly all scenarios, only portions of the polymers form the 3-D ordered structures, which are interspersed in an amorphous phase, and thus polymers that can crystallize are known to as semi-crystalline polymers. A more in-depth discussion on polymer crystallization will be discussed Chapter 4.

(A) R_X R_Y Not Brush $R_x < \sigma^1$

(B) Not Brush $R_x \approx \sigma^1$

(C) $\xi \sim \sigma^1$ H "Brush" $R_x > \sigma^1$

(D) $\xi \sim \sigma^1$ Brush $R_x \gg \sigma^1$
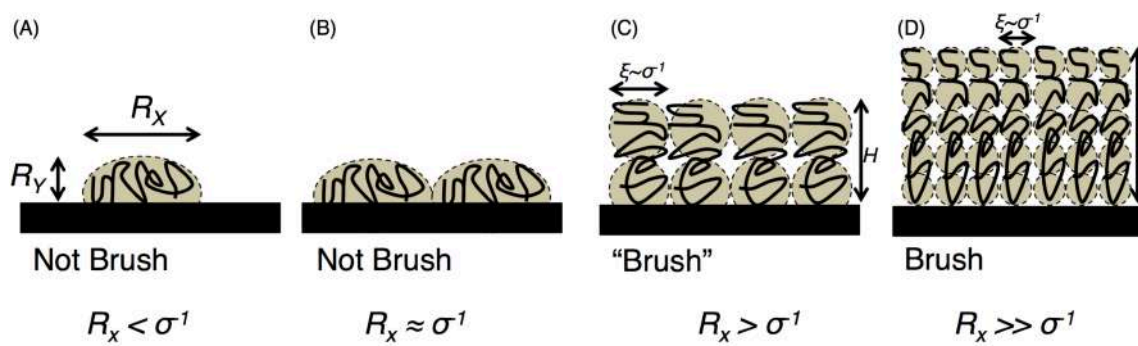
Figure A.6 Schematic of polymer brushes. A schematic representation of the Alexander-de Gennes model for polymer brushes with grafting density σ, correlation blob size ξ, and brush height H.

B   Literature Overview

B.1   Theory - SAW of Super Blobs

Initially, Birshtein et al.[18] considered the equilibrium structure through free energy minimization to obtain the scaling behavior of the asymptotic behavior of bottlebrush polymers. The linear chains in consideration had persistent segment, a, on the same order as the thickness, d, such that $p \sim a/d \sim O(1)$. To consider the asymptotic behavior, they used the condition $K >> n >> m$, where K is the number of units on the MC, n is the number of units on the SC, and m is the number of units in the main-chain between the side-chains.

On a large scale, they argued bottlebrush polymers appear to be a uniform filament with thickness, D, contour length, L', and Kuhn step of l. To obtain the equilibrium scaling behaviors, they minimized the elastic free energy and the free energy from the excluded volume interactions. They argued that when the main-chain bends, the side-chains can redistribute from the concave to the convex portion of the main-chain bend with no free energy cost. Thus, the apparent persistence length, $l_{p,app}$, induced from the side-chain repulsion, and the thickness of the bottlebrush are on the same length scale, $l_{p,app}/D \sim O(1)$. They dubbed the length scale of the apparent persistence segment to be a 'super-blob'. With a high density of monomers (main-chain monomers and side-chain monomers) in a super-blob (relative to linear), excluded volume interactions are present in both good and theta solvents. Thus, they concluded bottlebrush polymers behave as a SAW of super-blobs with scaling exponent of $\nu \approx 3/5$.

B.2   Theory - Worm-like chain (WLC)

In contrast to the SAW of super blobs model, Fredrickson had predicted BBPs to behave as a worm-like chain/cylinder (WLC). Fredrickson[19] considered a flexible chain being stiffened by adsorption of surfactant chains motivated by experimental work by Cao and Smith[21] on polyaniline complexed with camphosulfonic acid. At the high coverage limit when the surfactants begin to overlap, $\sigma >> M^{3/5}$, where σ is the number of chains per main-chain unit, M is number of units of surfactant chain, the polymer-surfactant complex

resembles a bottlebrush polymer. Similar to Birshtein, Fredrickson considers the asymptotic region given by the condition $N_{MC} \gg N_{SC} \gg 1$, where N_{MC} is the number of units in the MC, and N_{SC} is the number of units in the surfactants with σ side-chains per backbone unit evenly distributed.

Fredrickson considered the free energy cost of bending the polymer-surfactant complex (wormlike chain) with curvature, ρ, and calculated the change in free energy per unit length from that of the undeformed structure. He employed the Daoud-Cotton scaling approach (for a star-polymer) modified for a torus, a shape representation of bottlebrush polymers with curvature. The redistribution of side-chains from inner- to outer-bend of the torus was considered in the excluded volume interactions, explicitly considering the assumption made by Birshtein. Invoking the wormlike chain scaling relationship for free energy[20], the conclusion was that $l_{p,app}/D \sim \sigma^{15/8} N_{SC}^{9/8}$ which greatly exceeded unity, contrary to the results of Birshtein in which $l_{p,app}/D \sim O(1)$. Thus, the local structure appears to be rodlike on length scales shorter than $l_{p,app}$, but coil-like on much larger scales, given long contour length, key features of the WLC model. Therefore, Fredrickson concluded that the bottlebrush conformation could be approximated as a wormlike cylinder - a cylinder with a smooth contour and a large persistence length, much stiffer than the cross-sectional dimension, $l_{p,app}/D \gg 1$.

With experimental work by Cao and Smith[21] showing lyotropic behavior, Fredrickson argued that a large $l_{p,app}/D$ is crucial for onset of lyotropic behavior. Theoretical work by Onsager[22] requires $L/D \gg 1$ for a rod for a lyotropic phase. Later, it was shown that the relationship by Onsager can be applied to polymers by replacing L with persistence segment provided that the aspect ratio, $l_{p,app}/D$, is large, supporting WLC predictions by Fredrickson and contrary to SAW of super blobs predictions by Birshtein.

In further support for WLC model by Fredrickson, later works by Subbotin et. al, Nakamura et al., and Denesyuk also predicted a WLC depiction of BBPs. First, Subbotin et al.[23] considered the bending elasticity of a cylindrical brush through a self-consistent field approach. Like Fredrickson, they employed the free energy-curvature scaling

relationship of a wormlike chain to define the free-energy and persistence length. Their predictions were in better agreement with predictions by Fredrickson than Birshtein with $l_{p,app} \sim N_{SC}^2$ and $l_{p,app}/D \sim N_{SC}^{5/4}$, concluding bottlebrush polymers could be approximated as a wormlike chain, *i.e.*, $l_{p,app}/D \gg 1$.

Nakamura et al.[24] had a similar approach, in defining the free energy of bending to that of a wormlike chain, but incorporated side-chain contributions by including binary and ternary interactions through a first-order perturbation expansion in the free energy. Their calculations were in better agreement with predictions by Fredrickson than Birshtein with $l_{p,app} \sim N_{SC}^2$, however, they did not explicitly resolve the $l_{p,app}/D$ ratio. Therefore, we apply the limiting dimension of the side-chain by $R_{SC} \sim N_{SC}^1$ to conclude that Nakamura predicts $l_{p,app}/D > N_{SC}$, consistent with Fredrickson and the wormlike chain approximation of a bottlebrush. We want to note that they defined $l_{p,app} = l_{p,bare} + l_p$, where $l_{p,bare}$ is the persistence length associated with the bending of the main-chain and l_p contains all other contributions including interactions between the main-chain and side-chains near the main-chain.

Finally, Denesyuk[25] used general and renormalized perturbation theory to study the conformational changes with side-chain length and main-chain length in good solvent conditions. Their bottlebrushes were modeled by a system of star polymers of varying number of arms grafted onto a flexible main-chain at regular intervals. Most notably, three regimes are predicted at varying main-chain lengths: (1) for $N_{MC} < N_{SC}$, star-like behavior is observed in which side-chains are extended in all directions as predicted by the Daoud-Cotton model, (2) for $N_{MC} \sim N_{SC}$, the side-chains extend perpendicular to the main-chain axis adopting a 2D SAW ($\nu=3/4$), and (3) for $N_{MC} \gg N_{SC}$, coil-like structures are expected with $l_{p,app}/D$ with side-chain length dependence. During their derivation, they assumed a wormlike treatment of the overall dimension: (1) a rodlike scaling relationship of subchains as well as (2) relationships of total length and persistence length to architectural parameters. The calculations predict $l_{p,app}/D \sim N_{SC}^{1/2}$, consistent with Fredrickson, and strong side-chain length dependence on the apparent persistence length, $l_{p,app} \sim N_{SC}^{5/4}$.

Many simulation, numerical calculation, and experimental efforts aimed to corroborate either the SAW of super blobs model or the WLC chain model. However, instead of bringing clarity to the conformation behavior, the controversy had deepened as the reported results were consistent with both mutually exclusive models for the identical architectural parameter trends.

B.3   Simulation/Calculations – side-chain length dependence approaching WLC at asymptotic limit

First, simulation and numerical calculations by Feuz et al. predicted BBP conformation approaches a WLC behavior with increasing side-chain length. Feuz et al.[36] used the Scheutjens-Fleer self-consistent field approach to analyze the average conformation of side-chains and the resulting expanded conformation of the main-chain of bottlebrushes with varying side-chain length. Like Nakamura et al., Feuz defined a dual contribution to the apparent persistence length, $l_{p,app}= l_{p,bare}+l_p$. For a stiff main-chain such that $l_{p,bare}>>h$, where h is the distance between grafted chains, the contribution of bending rigidity adds on to the $l_{p,bare}$. For flexible main-chain, $l_{p,bare}<h$, the main-chain can adopt conformations dictated by thermal fluctuations on length scales $<h$, but on larger length scales, $\geq D$, bottlebrushes retain cylindrical symmetry. Their calculations showed in good solvent, $l_{p,app}\sim N_{SC}^{1.82}$. Normalized by the thickness, they showed $l_{p,app}/D$ had side-chain size dependence of $l_{p,app}/D\sim N_{sc}^{1.11}$. For short to moderate side-chains, $l_{p,app}/D\sim O(1)$, but showed $l_{p,app}/D$ approached 10 for long side-chains approaching $N_{SC}=10^3$.

B.4   Simulation – SAW of super blobs

Contrary to findings by Feuz, simulation work by Gauger et al., Saariaho et al., and Hsu et al. showed behavior approaching SAW of superblobs at the asymptotic limit. Gauger et al.[38] applied the cooperative motion algorithm to a bottlebrush architecture system and showed the reverse behavior where the behavior approaches that of a SAW of super blob and not a WLC. The main-chain length was held constant at 20 beads with varying grafting density $0.25<\sigma<2$ (2 side-chains per monomer) and length of side-chains,

$1<N_{SC}<50$. They studied various cases such as 2D and 3D melts and solution behavior. In melts, they showed random chain statistics with the excluded volume interactions being screened in the melt. In solutions, the conformations stretch from the side-chain repulsion. With increasing N_{SC} for $\sigma \leq 1$ (similar to experimental systems), the persistence length plateaus at $N_{SC}=20$ but the R_{SC} continuously increases. Although not discussed in the text, their results show that $l_{p,app}/D$ decreases with increasing N_{SC} for long N_{SC}.

Saariaho et al.[37] employed Monte Carlo simulations to investigate the differing theoretical predictions regarding $l_{p,app}/D$ ratio by the SAW superblob model by Birshtein and WLC model by Fredrickson. The simulation consisted of backbones of 100 beads of diameter 1 and 50 grafted side-chains, 4-20 beads in length. The diameter of the side-chain beads were varied as well. Their results showed $l_{p,app}/D$ was independent of the side-chain length for chains of 4-20 beads, which are relatively short. This result was in agreement with predictions made by Birshtein. However, with additional excluded volume interaction of the side-chains through increasing the side-chain bead size, $l_{p,app}/D$ increased drastically from $l_{p,app}/D\sim2$ to $l_{p,app}/D\sim4$ when the bead size was tripled. This result suggests that with long enough side-chains, the excluded volume interactions can affect $l_{p,app}/D$ and approach a value of $l_{p,app}/D>>1$, both consistent with predictions made by Fredrickson.

The simulated molecules of Monte Carlo simulations by Hsu et al.[33–35,44,45] ranged from $N_{MC}=131-1027$ units and the side-chain lengths ranged from $N_{SC}=6-24$. Their results showed that BBPs never displayed a behavior consistent with Kratky-Porod (WLC), but showed behavior consistent with the SAW of superblobs as predicted by Birshtein at the asymptotic limit. Although not discussed in their work, the results suggest main-chain lengths of ~100 superblobs are required to reach the asymptotic behavior. In addition, the local persistence length profile is consistent with the behavior stipulated by theorists – less stiff near the ends and most stiff in the middle. They showed that the profile could be fitted by the following profile $l_p(k) \approx \alpha l_b [k(N_b - k)/N_b]^{2\nu-1}$, where k is the monomer index on the main-chain, the prefactor alpha is a measure of the intrinsic stiffness of the chain, and ν is the solvent quality exponent for $0.3<k/N_{MC}<0.7$.

In addition, they provided $S(q)$ results that could be compared to SAXS/SANS experiments. They provided structure factor calculations of the overall brush as well as the main-chain, allowing analysis of the main-chain conformation without signal contributions from the side-chains. Also, they provided a local persistence length was defined allowing an analysis of the persistence length at each position in the main-chain allowing for the development of a more complete understanding rather than limited by scaling laws.

B.5   Experiment – Wormlike Chains/Cylinders

Like simulation results, which corroborated both models, experimental efforts did not provide compelling evidence to discriminate between the two mutually exclusive models either. Rathgeber et al.[39] analyzed bottlebrush polymers in good solvent through scattering techniques consisting of stitched SLS and SANS profiles with scattering contributions from the overall molecule and showed that with increasing side-chain length, the behavior transitions from a WLC to a behavior consistent with SAW of super blobs. Their PAMA-PnBA bottlebrushes were synthesized via the grafting-from route with >95% grafting density. With systematic variation in architectural parameters, N_{SC} and N_{MC}, and stitching of SLS and SANS to obtain a full scattering profile, the structure-dimension correlation could be assessed. To analyze the experimental data, they treated the bottlebrush polymers to be accurately approximated by a semi-flexible wormlike cylinder. With $L>>D$ for the cylinder, they approximated the overall form factor to be the product of two contributions – the form factor of a infinitely thin worm-like chain, $P_{wlc}(q)$, and cross-sectional form factor, $P_{cs}(q)$, such that $P_{overall}(q)=P_{wlc}(q)P_{cs}(q)$. However, this product can only approximate scattering on length scales larger than the cross-sectional radius. Therefore, at high-q, internal density fluctuations of the side-chains were explicitly considered as well.

The fits of the form factors to the SLS/SANS scattering profiles showed that for N_{SC}=22-98, a side-chain length independent persistence length of about 70nm, about 46 time larger than the bare persistence length. They demonstrated that with a fixed persistence length, their chosen form factors could fit the experimental data precisely.

Other experiments[16,26–29,31,32] have found similar results of persistence lengths of 1-2 orders of magnitude (up to[16] $l_{p,app}$~208nm) higher than that of the bare main-chain as well as $l_{p,app}/D$>5 (up to[16] $l_{p,app}/D$~40) through fitting to the worm-like chain model. Zhang et al.[31] applied a multifaceted approach to obtain $l_{p,app}/D$>O(1), but incorporated wormlike/rodlike assumptions. First, form factor models applied to fit the SLS/SANS scattering profiles were that of wormlike/rodlike form factors with excluded volume corrections. In addition, they applied work by Holtzer, who postulated the existence of a plateau (Holtzer plateau) for an infinitely thin rods at high-q in a Holtzer plot, qI/c vs. q at a value of πL to obtain the contour length of the wormlike cylinder. Therefore, most experimental results seem to qualitatively agree with predictions by Fredrickson, although quantitatively, they may differ. Recently, with very long side-chains of PS115 side-chains, Sugiyama et al.[29] showed quantitative agreement with Fredrickson, a quadratic dependence on the side-chain length of the persistence length.

Although the magnitude of their persistence length is large, Rathgeber showed an inverse correlation of $l_{p,app}/D$ with N_{SC} with a scaling relationship of $l_{p,app}/D$~$N_{SC}^{-0.57}$. With long enough side-chains, $l_{p,app}/D$ could reach order of 1 as predicted by Birshtein. The only other work predicting a decreasing $l_{p,app}/D$ relationship with N_{SC} was Monte Carlo simulation work by Gauger[38], who showed this behavior at very long side-chain lengths as previously discussed.

The experimental results that are in agreement with predictions by Fredrickson are highly controversial, with their analysis assuming a worm-like chain treatment to some degree – fitting WLC form factor models to scattering profiles or fitting WLC scaling to R_g results. Rathgeber showed that quality fits to scattering patterns can be obtained even for a fixed persistence calling into question the validity of the fitted parameters. In addition, Hokajo et al.[28] showed $l_{p,app}$~N_{SC}^1 through $l_{p,app}$ obtained from fitting R_g vs. L data as predicted by the WLC for N_{SC} of 15, 33, and 65. The group continued the work[29] and later showed that with an additional side-chain length of N_{SC}=113, the $l_{p,app}$ from the R_g vs. L WLC fit showed $l_{p,app}$~N_{SC}^2. The extreme sensitivity in the fitted parameters calls into

question the validity of the model/methodology used in characterizing the conformation of bottlebrush polymers. Our work aims to put the worm-like chain assumption to the test to validate the wormlike chain assumption.

In addition to the controversial results, experimental efforts showed that resolving the controversy is more complex than seems at the surface level, showing significant changes in conformation with variations architectural parameters.

B.6   Experiment – Main-chain length for minimizing end effects of side-chains

Terao et al.[30] considered the end effects on the contour length of the brush of the side-chains which may arise when side-chains near the ends of the bottlebrush are oriented in the direction of the main-chain contour. The net effect would be a longer contour than is offered by the main-chain alone. Thus, the total contour length should be the sum of two contributions: the main-chain and the side-chains. For N_{MC}=33, they showed the end effects only contribute 7nm^2 to the overall R_g^2, only a 5% contribution of the shortest bottlebrush considered in their work, N_{MC}=224. Thus, they concluded that end-effects may be ignored for N_{MC}/N_{SC}>6.7 and possibly smaller since they did not report a lower bound.

B.7   Experiment - Coil to zig-zag/helical conformation of the main-chain

Wataoka et al.[41] showed that for PS-PMA brushes, at short main-chain length (N_{MC}<9), oblate ellipsoid and elliptical cylinder profiles could fit the SAXS profiles. With increase in main-chain length, only the elliptical cylinder fit the observed SAXS profile. For all samples with N_{MC}>9, the cross-section had a semi-axis ratio of about 1.8, predicting an extended conformation of the main-chain in either helices or a zigzag conformation. At low N_{MC}(<9), a comparison to molecular modeling showed Gaussian conformations for both side-chains and main-chains. The next lowest N_{MC} considered was 30, which showed an elliptical cylinder fit. The side-chain lengths used was N_{SC}=54. Therefore, the transition between oblate ellipsoid to elliptical cylinder (and Gaussian conformation to extended conformation) occurred at roughly N_{MC}/N_{SC}=1.8, close to unity.

B.8   Experiment – Star to bottlebrush transition

Recently, Pesek et al.[42] showed a sphere-cylinder transition occurring at roughly main-chain DP of N_{MC}=120 for PNB-PS system. For bottlebrushes with N_{SC}=14-54 and N_{MC}=11-264, with no systematic variation, they fit SANS scattering profiles to the Guinier-Porod model, obtaining two parameters – radius of gyration and the dimension parameter, *s*, which reflects the shape of the molecule ranging from a sphere (*s*=0) to a rodlike structure (*s*=1). For bottlebrushes with N_{MC}<120, the dimension parameter remained at approximately *s*=0.1 predicting a sphere-like structure, independent of the side-chain length. With increasing N_{MC} from 120 to 250, the dimension parameter increased from 0.1 to 0.7, indicating an elongated structure, such as a cylinder with the transition occur at N_{MC}=120.

In addition, they demonstrated that both rigid and flexible cylinder models could fit the overall scattering pattern well as well as the Guinier-Porod model. Due to the nondiscriminatory nature of the fitting method, no behavioral models can be eliminated, and, therefore, no behavioral models can be conclusively confirmed as well. For the same polymer, the Kuhn length ranged from the intrinsic Kuhn length of 7nm for PNB in the Guinier-Porod model, to 113.3nm from fitting to a flexible cylinder model to 443.0nm from fitting to a rigid cylinder, spanning almost 2 orders of magnitude. The researchers do use the fit parameter of 443.0nm as the stiffness, but only an estimate of the contour length; however, the quality of the fit of the rigid model to the overall scattering data cannot be ignored.

B.9   Concentration Dependence

So far, the discussion has been of the controversy of BBP conformation in dilute solutions. The behavior becomes increasingly complex in the semidilute regime with contradictory results in literature. Early theoretical work by Borisov et al.[47] predicted four different concentration regimes per solvent quality. By minimizing the free energy contribution from concentration of monomers, stretching of the side-chain, and stretching of the main-chains, they predicted significant conformational transitions with

concentration. As the concentration is increased from dilute solution (region I) to the semidilute solution (region II), the bottlebruhses begin to overlap without any affect on the local structure (of the side-chains and main-chain). Instead, the overall size, R_x, decreases with increasing concentration with a scaling relationship $R_{IIx} \sim c^{-1/8}$. As the concentration is increased into semidilute (region III), a dense packing of bottblebrushes is predicted. In an analogous concentration regime for star polymers[82], the stars were impermeable repelling neighboring stars through scaling arguments. Only when the side-chains reached Gaussian dimension did arms begin to penetrate. In accord with the behavior for stars, they predict a decreasing cross sectional (side-chain) length scale, D, and overall size with concentration with behavior $D_{III} \sim c^{-11/28}$ and $R_{IIIx} \sim c^{-17/56}$, respectively. At the highest concentration, the solution becomes a densely packed system of blobs. They predict the main-chain is no longer affected by the presence of the side-chains and the main-chain behaves as a linear polymer in the respectively solvent quality in the semidilute regime with scaling prediction $R_{IVx} \sim c^{-1/8}$ identical to the concentration dependence to in semidilute region II.

Rathgeber[40] studied PAMA-PnBA system and concluded that bottlebrushes could be modeled as a flexible cylinder with density fluctuations from the side-chains adopting a 3D-SAW. They inferred that the main-chain adopts a stretched conformation with $l_{p,app} \approx 35$nm through fitting to SLS/SANS profiles. At low concentrations, they showed that the system formed an isotropic solution. With increasing concentration, the solution entered an ordered hexagonal phase ($\phi = 16.6\%$) indicating a large $l_{p,app}/D$ ratio. In dilute solutions, $2R_{CS} = 10.2$nm, $l_{p,app}/D = l_{p,app}/2R_{CS} = 3.5$, just above the $l_{p,app}/D > 3.34$ cutoff predicted by Onsager. With further increase in concentration, the solution showed a reentry into an isotropic phase ($\phi = 30\%$). When the inter-particle spacing becomes smaller than the radial dimension of the bottlebrush, significant interpenetration of side-chains begins to screen the excluded volume effects responsible for the large persistence length, the criteria for lyotropic ordering.

Works by Bolisetty et. al[49,50] showed significant softening reduction in persistence length with concentration in a similar fashion as polyelectrolyte systems. Although the polymer system used was a PHEMA-PtBA system (N_{MC}=1600, N_{SC}=61) in which the main-chain has two backbone carbons for a monomer lengthm of l_{mon}=0.25nm, the grafting density was 0.49 with statistically alternating repeat units with side-chains and without side-chains for a average graft spacing of 0.5nm, very similar to PNB main-chain systems (graft spacing=0.6nm). They observed extremely low overlap concentration with non-negligible interactions beginning below their lowest measured concentration of c=0.2%. Between c=0.2-4.0%, they showed a reduction in $l_{p,app}$ from 17.5nm to 5nm predicted by Borisov et al. Like Rathgeber et. al, they corrected the high-q scattering contribution from density fluctuations from the side-chains prior to analyzing the SLS/SANS patterns. They used a self-consistent field integral equation that incorporated a concentration-dependent persistence length

$$G\left[l_p(\phi), l_p(0)\right] =$$

$$\int_0^\infty dq\, q^2 \frac{W(q,\phi)}{kT} \int_0^L ds_1 \int_0^L ds_2\, (s_1 - s_2)^2 \exp\left(-\frac{q^2 a(s_1 - s_2, \phi)}{6}\right), \tag{B.1}$$

where

$$a(s,\phi) = 2l_p(\phi)|s| - 2l_p(\phi)^2 \left(1 - \exp\left(-\frac{|s|}{l_p(\phi)}\right)\right), \tag{B.2}$$

which provided excellent fits to the SANS/SLS scattering profiles to obtain concentration dependence on l_p.

Recently, Paturej used a theoretical approach minimizing the free energy for stretching the main-chain and side-chains arising from the excluded volume interactions. In contrast to earlier work, when calculating the stretching of the main-chain, they focused on smaller subsegments rather than the conventional focus on the overall main-chain. They used MD simulations to corroborate their theoretical analysis. With increasing

concentration, they showed five different concentration regimes with varying degrees of screening of excluded volume interactions that favor a SAW. Increasing the concentration from dilute to $c_1<c<c_2$, the macromolecules start to overlap and the excluded volume is screened on length scales comparable to the extended main-chain. Therefore, the SAW of persistence steps becomes a RW of persistence steps with the screened excluded volume interactions. With a slight increase in concentration to $c_2<c<c_3$, the individual persistence segments begin to overlap, screening the excluded volume interactions on persistence step length scales. Therefore, the main-chain monomers within a persistent segment transitions from a SAW to RW. At higher concentrations $c_3<c<c_4$, side-chains from different bottlebrush polymers begin to interact, screening the excluded volume interactions of side-chains to adopt a RW from a SAW. At the highest concentration $c>c_4$, side-chains from the same bottlebrush begin to screen each other. The conceptual picture presented by Paturej is contradictory to that of Borisov, who predicts that side-chains adopt a RW from a SAW due to repulsion of side-chains from the neighboring bottlebrushes.

B.10   *Melt Behavior and Tension blob model*

Recent simulations in the melt by Paturej et al.[51] provided great insight into the behavior of BBPs, which, we believe, can be extended to solution behavior with slight modifications. In the melt, they show significant screening of the excluded volume interactions. For $z=2$ side-chains per main-chain monomer, they show local flexibility, on length scales smaller than the thermal blob and the persistence length. They showed an initial fast decay in the main-chain bond correlation regardless of the system, matching that of their linear control. Their $qS(q)$ for the main-chain showed a maximum in the Holtzer plot, consistent with their assessment of local flexibility of the main-chain. It is important to note that the local flexibility observed for $z=2$ is more flexible than compared to that of a rod ($z=4$), but not as flexible as the linear control, demonstrating some local stiffening. Surprisingly, when the grafting density is doubled to $z=4$, the local flexibility disappears and the main-chain form factor could be approximated as a rod, even with the screening of excluded volume interactions from the melt.

Paturej defined the bottlebrush regime to be the scenario in which the main-chain has to extend to accommodate the SC interpenetration. Using a scaling analysis, they proposed that at local length scales the effects of tension become apparent at longer length scales. To understand their approach, it is useful to consider a specific scenario. In the melt, Gaussian statistics are expected for polymers; therefore a side-chain has an unperturbed Gaussian size of $R_{SC} \approx (blN_{SC})^{1/2}$ (pre-exponential factors have been dropped) and pervaded volume, $V_{perv} = R_{SC}^3 = (blN_{SC})^{3/2}$. The total number of side-chains that can be within this pervaded volume without perturbing Gaussian statistics is $V_{perv}/V_{SC} = (bl)^{3/2}N_{SC}^{1/2}/v$, where $V_{SC} = vN_{SC}$. Within this pervaded volume, the MC running through the length of R_{SC} is also N_{SC}, since all polymer units are Gaussian statistics. Therefore, if $zN_{SC} > V_{perv}/V_{SC}$, where z is the number of side-chains per main-chain monomer, then an extended conformation is required. If $N_{SC} < V_{perv}/V_{SC}$, then the MC can freely adopt a Gaussian conformation.

For the scaling analysis, an arbitrary length scale, r, is used instead of a fixed length scale, R_{SC}. For small length scales, the thermal fluctuations dominate favoring Gaussian chain statistics in the melt. The pervaded volume occupied by r is $V_{perv}(r) \sim r^3$. Within this arbitrary sphere, the number of MC units, m, can be obtained using a Gaussian relationship $r \approx (blm)^{1/2}$. With z side-chains, each contributing m monomers to the sphere and $V_{SC}(r) = vm$, on each main-chain monomer, the total number of monomers in the sphere is zm^2. Therefore, we can conclude a scaling relationship $r \sim zm^2$. The quadratic dependence of m reveals that at an certain value of r, which we define as ξ, $zm = V_{perv}(\xi)/V_{SC}(\xi)$. For $r < \xi$, the chain can remain as a Gaussian since the side-chains do not fully occupy the pervaded volume. For $r > \xi$, the chains need to be extended. Therefore ξ is referred to as the tension blob. Inside $\xi \approx (blg)^{1/2}$ are g monomers which can be obtained from the condition that the pervaded volume ξ^3 is fully occupied by monomoners from gz sidechains of size g $\xi^3/vg = gz$. The tension blob size is $\xi = (lb)^2/vz$. However, the extension cannot be extended to $r \rightarrow \infty$ since the size of the side-chain is finite. Until $r \sim R_{SC}$, the main-chain remains extended as an extended array of tension blobs size ξ. For $r > R_{SC}$, the chain begins to be a Gaussian of steps sizes of these extended array of tension blobs on size R_{CS}.

To summarize, three length scale regimes have been identified. For $r<\xi$, thermal fluctuations dominate. For $\xi<r<R_{SC}$, the main-chain can be visualized as an extended array of tension blobs which remains extended until $\sim R_{SC}$. For $r>R_{SC}$, the main-chain can be visualized as a Gaussian steps the extended array of tension blobs, size R_{SC}.

B.11 Additive Treatment of persistence lengths

A common theme across literature was the cumulative treatment of the intrinsic persistence length of the main-chain unperturbed by the side-chain excluded volume interactions, $l_{p,o}$, with the additional contribution from the side-chain[23,24,31,36] $l_{p,b}$

$$l_p = l_{p,0} + l_{p,b}$$

(B.3)

Although majority of the focus in literature has been devoted to determining the stiffening due to side-chain repulsion, usually characterized by $l_{p,b}$, there is disagreement in the definition of $l_{p,o}$. Feuz et al.[36] and Subbotin et al.[23] treated the $l_{p,o}$ to be equal to the persistence length of the bare main-chain, whereas Nakamura et al.[24] theorized $l_{p,o}$ to contain short-range interactions from the side-chains and, therefore, to be different than that of the bare main-chain. Zhang et al.[31] confirmed this hypothesis, showing roughly $l_{p,o}$ >2.5nm in both good and theta solvent for PMMA ($l_{p,PMMA}$=1nm). To add to the issue, the additive treatment as a methodology has not been experimentally verified.

C   Experimental techniques

C.1   Scattering Techniques

Scattering techniques provide a quantitative method to measure the size, structure, and shape of various systems to understand the relationship between the physical properties and the structure. Different types of radiation sources (e.g., light, neutrons, and X-rays) interact differently with experimental particles/structures (e.g., polymers, colloids, etc.) thereby offering unique scattering patterns.

C.1.1   Static Light Scattering / Multi-Angle Light Scattering

Light is an electromagnetic field which can induce a dipole moment in polarizable particles. The induced dipole moments radiate light in all directions. The strength of the dipole moment is proportional to the electromagnetic field where the proportionality constant is known as polarizability, α_p

$$\alpha_p = \frac{n_o cV}{2\pi nN}\frac{dn_o}{dc},\qquad(\text{C.1})$$

where n_o is the refractive index, c is the concentration, V is volume, N is Avogadro's number, and dn_o/dc is the concentration dependence on the refractive index. If the $dn_o/dc=0$, *i.e.*, the refractive indices of the particles and solvent are identical, $\alpha_p=0$ and no scattering is observed.

Two light scattering techniques were used in these studies: Multi Angle Laser Light Scattering (MALLS) and Static Light Scattering (SLS). In both techniques, scattered light intensity is measured at different angles (simultaneous measurement for MALLS and sequential measurement for SLS) to obtain parameters such as the molecular weight, MW, and radius of gyration, Rg. The basic relationship is given by the equation

$$\frac{R_\theta}{Kc} = M_w P(\theta) - 2A_2 M_w{}^2 P^2(\theta)c + \cdots,\qquad(\text{C.2})$$

where R_θ is the Rayleigh ratio, which is directly proportional to the ratio of the incident intensity to the scattered intensity at an angle θ, K is the optical constant only dependent on the solvent properties and the wavelength λ, c is the concentration, M_w is the weight-

averaged molar mass, and $P(\theta)$ is the particle form factor. For large wavelengths or small particles, the $P(\theta)$ can be approximated by

$$P(\theta) = 1 - \left(\frac{16\pi^2}{3\lambda^2}\right) R_g \sin^2\left(\frac{\theta}{2}\right), \tag{C.3}$$

and after substitution equation B.2 becomes

$$\frac{R_\theta}{Kc} = M_w \left(1 - \left(\frac{16\pi^2}{3\lambda^2}\right) R_g \sin^2\left(\frac{\theta}{2}\right)\right). \tag{C.4}$$

No assumptions regarding shape and intramolecular conformations were made to obtain this relationship. Therefore, B.4 is applicable to all systems in which the wavelength is much larger than the scattering species ($qR_g \ll 1$). Defining a scattering vector q

$$|q| = q = \frac{4\pi}{\lambda} \sin\left(\frac{\theta}{2}\right), \tag{C.5}$$

and keeping the second order term to account for nonideal solution conditions results in the Zimm equation

$$\frac{Kc}{\Delta R(\theta,c)} = \frac{1}{M_w}\left(1 + \frac{q^2 R_g^2}{3} + O(q^4)\right) + 2A_2 c + O(c^2), \tag{C.6}$$

where A_2 is the second virial coefficient. To obtain desired parameters, R_g, M_w, and A_2, a Zimm plot is constructed by plotting $Kc/R(\theta,c)$ vs. $q^2 + kc$ where k is a constant to spread the plot to give equal weights to each variable. In deriving the Zimm equation, $qR_g \ll 1$ was assumed. For polymer samples particles may be very large and this assumption may not be valid. For large particles, light will scatter from different parts of the particle leading to different path lengths to the detector. The difference in path lengths can lead to destructive interference. A simple solution would be to measure at $\theta = 0$ which guarantees the path lengths to be equal. However, at $\theta = 0$, most of the intensity is transmitted light which provides no useful information. To overcome this limitation, measurements are made at multiple q values and extrapolated to $q \rightarrow 0$ to obtain the $\theta = 0$ scattering intensity. The slope and intercept associated with this line are $R_g^2/3M_w$ and M_w^{-1}. Nonidealities in polymer solutions are very common. To correct for nonidealities, measurements are taken at multiple concentrations to extrapolate $c \rightarrow 0$. The concentration measurements must be

taken in dilute conditions in which the scattered intensity has linear dependence on concentration. The slope and intercept associated with this line are $2A_2$ and M_w^{-1}.

Zimm plots are often used to measure R_g, M_w, and A_2. The A_2 is a determining factor for the solvent quality of a polymer. Good solvent has excluded volume interactions, thus the $A_2 > 0$. Poor solvent has a net attraction with $A_2 < 0$. At the transition, where $A_2 = 0$ corresponds to the theta solvent. The temperature associated is referred to as the theta temperature of that solvent-polymer combination.

C.1.2   *Small angle neutron scattering*

The wavelength of light spans approximately $400nm < \lambda < 800nm$, much larger than the overall structure of polymeric systems. Thus, light radiation is not an ideal choice for understanding the intramolecular conformation of polymeric systems which has length scales on the order of 1-10nm. Neutrons are an excellent radiation source to measure the intramolecular conformations with wavelengths $\lambda \sim 0.4nm$. Light scatters from contrast in refractive index (or polarizability) between the scattering species and the solvent, but neutrons scattering from contrast in differences in nuclei, or scattering length, *b*. A significant advantage results from the neutrons scattering from the nuclei – hydrogen and deuterium have significantly different nuclear density. Therefore, replacing hydrogen with deuterium in polymeric systems allows selective scattering from selected components with only minor effects on the system (Figure C.1).
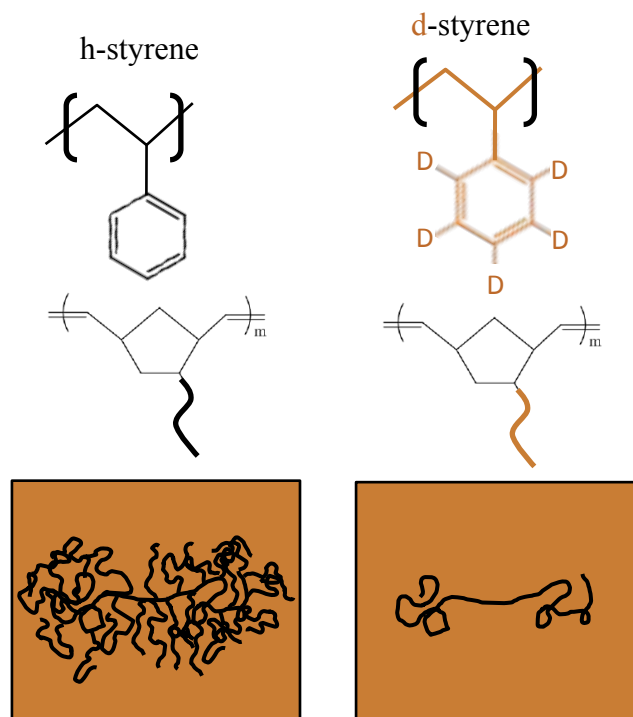
Figure C.1. Effects of deuterium labeling in SANS experiments. Utilizing hydrogenous main-chain and deuterated side-chains in deuterated solvent enables selective scattering from the main-chain only.

Typically, neutron experiments are measured as a function of the scattering vector, q, as opposed to the scattering angle, as is the case for static light scattering, which has the following relationship

$$|q| = q = \frac{4\pi}{\lambda}\sin\left(\frac{\theta}{2}\right), \tag{C.7}$$

where λ is the neutron wavelength and theta is the scattering angle between the scattering source and the position of the detector. The scattering wavevector has an inverse relationship to length scale

$$q = \frac{2\pi}{d}. \tag{C.8}$$

For elastic scattering, the scattered intensity can be calculated

$$I(q) = \sum_{i=1}^{N}\sum_{j=1}^{N} b_i b_j e^{iq\cdot(r_i - r_j)}, \tag{C.9}$$

where b_i and b_j are the scattering length density of components i and j respectively, r_i and r_j are the position vectors for components i and j, respectively. The scattering intensity is a product of the intermolecular structure, structure factor $S(q)$, and the intramolecular structure, $P(q)$ as follows

$$I(q) = P(q)S(q).$$ (C.10)

For dilute solutions, where individuals molecules are spaced far apart, $S(q)$=1. Thus for dilute conditions, $I(q)$=$P(q)$.

Linear polymers exhibit scattering patterns with two primary features on log-log scale – the Guinier plateau and the Porod region. At high-q, the Porod region is marked by slopes of m=-2 for theta solvent and m=-1.7 for good solvent, showing an inverse relationship with the fractal dimension, v=0.5 and v=0.588 for θ and good solvent, respectively. Thus, SANS is a method to directly measurement of the scaling relationship. At low-q, the scattering becomes independent of the internal chain structure and begins to scatter from the whole polymer chain. The intensity value can be used to extract the MW of the polymer chain. The d-spacing of the q-value corresponding to the Guinier-Porod transition can be used to extract the length scale of the polymer chain.

C.1.3 Dynamic light scattering

Scattering techniques are not limited to measurement of static properties of polymers, but can provide important information about the dynamic properties as well. The intensity discussed previously in section C.1.2 was the static scattering intensity $I(q)$, which is the instantaneous scattering intensity $I(q,t)$ averaged over a long period of time. The static scattering intensity depends on the spatial arrangement of the scattering units (conformation of the polymers). As the conformation of the polymers moves and changes shape, the instantaneous scattering intensity captures the fluctuations with time. In dilute systems, the diffusion coefficient, D, can be directly measured from dynamic light scattering. Using the diffusion coefficient, thy hydrodynamic radius, R_h, can be obtained through the Stokes-Einstein equation

$$R_h = \frac{kT}{6\pi\eta_s D},$$

(C.11)

where T is the temperature, k is the Boltzman constant, and ns is the solvent viscosity.

The ratio R_g/R_h provides a method of understanding the shape anisotropy. For a hard sphere of radius, R, the hydrodynamic radius is equal to R whereas the R_g is slightly smaller with $R_g/R_h = 0.77$ for a sphere. For linear, monodisperse polymers, $R_g/R_h = 1.5$ and 1.3 for good solvent and θ solvent, respectively. With topological complexity, changes in R_g/R_h is observed. For example, for a 3-arm star has an $R_g/R_h=1.3$, but as the number of arms are increased, the R_g/R_h value continues to decrease.

C.2   *Differential scanning calorimetry*

DSC is a thermal analysis technique that measures heat flow, q, difference to a known amount of experimental sample to a reference sample as a function of temperature. As a result DSC can be used to measure the temperature dependence of the heat capacity as well as detection of phase transitions including melting/crystallization and glass transition temperatures in polymer systems. Including identification of the phase transition temperature, the heat of fusion as well as the phase kinetics can also be measured.

The heat capacity, C_p, is the ratio of heat flow, q/t, to the heating rate, $\Delta T/t$

$$\frac{q/t}{\Delta T/t} = \frac{q}{\Delta T} = C_p.$$

(C.12)

Glass transition are marked by sharp change in the heat capacity. As polymers are heated from below to above the glass transition temperature, T_g, the polymer transitions from a glassy state to a rubbery state in which the polymers chains gain additional mobility. This additional degree of freedom enables higher storage of thermal energy thus a sharp increase in heat capacity is observed in the DSC.

In contrast to the glass transition, crystallization and melting transitions can be identified via sharp peaks – endothermal peak for melting and exothermal peak for crystallization. For Heat flow vs. T, the heat of fusion is the ratio of the peak area to the heating rate. If Heat flow vs. t, the heat of fusion is simply the peak area.

C.3   Atomic force microscopy

Atomic force microscopy is a specific type of scanning probe microscopy with resolution on the nanometer length scale. Images and force measurements can be obtained via precise movements of a mechanical probe controlled by piezoelectronics. For polymers, topographical and phase images can help identify morphology in various copolymer and blend systems. A topographical image is obtained by a change in amplitude of the oscillation mechanical probe from contact with the polymer surface. The phase image can be obtained from the phase change with respect to the driving oscillator associated with the contact of the mechanical probe the polymer surface. Polymers with different mechanical properties results in distinct phase measurements allowing the imaging of morphologies.

C.4   Transmission electron microscopy

Transmission electron microscopy is a microscopy technique in which an image is obtained by measuring the number of electrons that were transmitted through different parts of the irradiated sample. Typically, samples are super thin films of thickness <100 nm or microtomed sections of similar thickness placed onto an appropriate grid. TEM offers incredible spatial resolution even being able to differentiate single atoms.

For copolymer morphology analysis, special sample preparation is required to guarantee enough contrast for morphological identification and noninvasive sectioning. The electron absorption contrast between distinct polymers is negligible due to the similarity in the electron density of elements that compose organic molecules – carbon, oxygen, and nitrogen. To increase contrast between distinct polymers, a staining agent must be used, commonly OsO_4 or RuO_4. The staining agent reacts preferentially to one of the components significantly reducing the transmitted electrons resulting in a darkened portion of the image.

To obtain ultrathin films, polymer samples are cut using a microtome. During the cutting, the polymer sample is susceptible to deformation, which can alter the microstructure prior to imaging. To circumvent the deformation, the sample must be brought below the glass transition temperature of the lowest T_g component to its glassy

state, typically via LN$_2$, called cryo-microtome. Below the T_g, the morphology and polymer chains have restricted movement, which allows for precise scission during sectioning.

D   Chemical structure of bottlebrush polymers used in Chapters 2 and 3

The chemical structure of the bottlebrush polymers used for conformational studies in Chapters 2 and 3 (Figure D.1) consists of a poly-norbornene (PNB) main-chain and polystyrene (PS) or d8-polystyrene (dPS) side-chains. The linker and terminal groups are also shown. The synthetic details are outline by Pirogovsky[60].
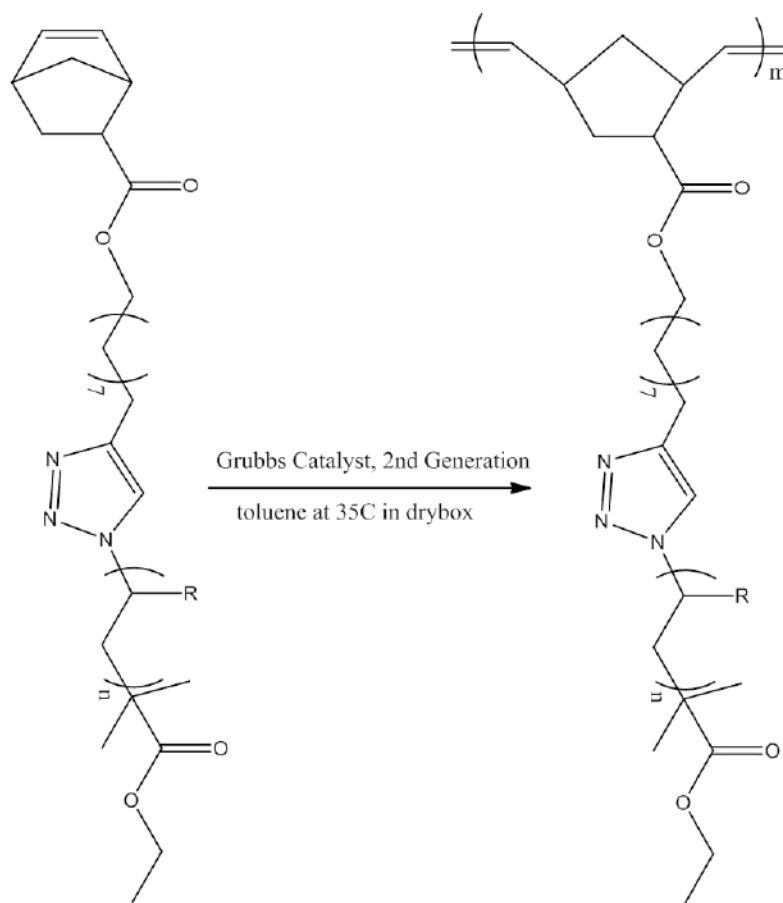
Figure D.1. Chemical structure of bottlebrush polymers used in Chapters 2 and 3.

REFERENCE

(1)   Morse, M. A. Craniology and the Adoption of the Three-Age System in Britain. *Proc. Prehist. Soc.* **1999**, *65*, 1–16. https://doi.org/10.1017/S0079497X00001924.

(2)   Stone Age, Iron Age, Polymer Age. 1.

(3)   Pakula, T.; Zhang, Y.; Matyjaszewski, K.; Lee, H.; Boerner, H.; Qin, S.; Berry, G. C. Molecular Brushes as Super-Soft Elastomers. *Polymer* **2006**, *47* (20), 7198–7206. https://doi.org/10.1016/j.polymer.2006.05.064.

(4)   Daniel, W. F. M.; Burdyńska, J.; Vatankhah-Varnoosfaderani, M.; Matyjaszewski, K.; Paturej, J.; Rubinstein, M.; Dobrynin, A. V.; Sheiko, S. S. Solvent-Free, Supersoft and Superelastic Bottlebrush Melts and Networks. *Nat. Mater.* **2016**, *15* (2), 183–189. https://doi.org/10.1038/nmat4508.

(5)   Johnson, J. A.; Lu, Y. Y.; Burts, A. O.; Lim, Y.-H.; Finn, M. G.; Koberstein, J. T.; Turro, N. J.; Tirrell, D. A.; Grubbs, R. H. Core-Clickable PEG- *Branch* -Azide Bivalent-Bottle-Brush Polymers by ROMP: Grafting-Through and Clicking-To. *J. Am. Chem. Soc.* **2011**, *133* (3), 559–566. https://doi.org/10.1021/ja108441d.

(6)   Xia, Y.; Olsen, B. D.; Kornfield, J. A.; Grubbs, R. H. Efficient Synthesis of Narrowly Dispersed Brush Copolymers and Study of Their Assemblies: The Importance of Side Chain Arrangement. *J. Am. Chem. Soc.* **2009**, *131* (51), 18525–18532. https://doi.org/10.1021/ja908379q.

(7)   Chang, A. B.; Bates, C. M.; Lee, B.; Garland, C. M.; Jones, S. C.; Spencer, R. K. W.; Matsen, M. W.; Grubbs, R. H. Manipulating the ABCs of Self-Assembly via Low-χ Block Polymer Design. *Proc. Natl. Acad. Sci.* **2017**, *114* (25), 6462–6467. https://doi.org/10.1073/pnas.1701386114.

(8)   Dalsin, S. J.; Rions-Maehren, T. G.; Beam, M. D.; Bates, F. S.; Hillmyer, M. A.; Matsen, M. W. Bottlebrush Block Polymers: Quantitative Theory and Experiments. *ACS Nano* **2015**, *9* (12), 12233–12245. https://doi.org/10.1021/acsnano.5b05473.

(9)   Faivre, J.; Shrestha, B. R.; Burdynska, J.; Xie, G.; Moldovan, F.; Delair, T.; Benayoun, S.; David, L.; Matyjaszewski, K.; Banquy, X. Wear Protection without Surface Modification Using a Synergistic Mixture of Molecular Brushes and Linear Polymers. *ACS Nano* **2017**, *11* (2), 1762–1769. https://doi.org/10.1021/acsnano.6b07678.

(10)   Sveinbjornsson, B. R.; Weitekamp, R. A.; Miyake, G. M.; Xia, Y.; Atwater, H. A.; Grubbs, R. H. Rapid Self-Assembly of Brush Block Copolymers to Photonic Crystals. *Proc. Natl. Acad. Sci.* **2012**, *109* (36), 14332–14336. https://doi.org/10.1073/pnas.1213055109.

(11)   Banquy, X.; Burdyńska, J.; Lee, D. W.; Matyjaszewski, K.; Israelachvili, J. Bioinspired Bottle-Brush Polymer Exhibits Low Friction and Amontons-like Behavior. *J. Am. Chem. Soc.* **2014**, *136* (17), 6199–6202. https://doi.org/10.1021/ja501770y.

(12)   Xie, G.; Krys, P.; Tilton, R. D.; Matyjaszewski, K. Heterografted Molecular Brushes as Stabilizers for Water-in-Oil Emulsions. *Macromolecules* **2017**, *50* (7), 2942–2950. https://doi.org/10.1021/acs.macromol.7b00006.

(13)   Bates, C. M.; Chang, A. B.; Momčilović, N.; Jones, S. C.; Grubbs, R. H. ABA Triblock Brush Polymers: Synthesis, Self-Assembly, Conductivity, and Rheological Properties. *Macromolecules* **2015**, *48* (14), 4967–4973. https://doi.org/10.1021/acs.macromol.5b00880.

(14) Rose, M. C.; Voynow, J. A. Respiratory Tract Mucin Genes and Mucin Glycoproteins in Health and Disease. *Physiol. Rev.* **2006**, *86* (1), 245–278. https://doi.org/10.1152/physrev.00010.2005.

(15) Klein, J. Repair or Replacement - A Joint Perspective. *Science* **2009**, *323* (5910), 47–48.

(16) Wintermantel, M.; Gerle, M.; Fischer, K.; Schmidt, M.; Wataoka, I.; Urakawa, H.; Kajiwara, K.; Tsukahara, Y. Molecular Bottlebrushes [†]. *Macromolecules* **1996**, *29* (3), 978–983. https://doi.org/10.1021/ma950227s.

(17) Panyukov, S.; Zhulina, E. B.; Sheiko, S. S.; Randall, G. C.; Brock, J.; Rubinstein, M. Tension Amplification in Molecular Brushes in Solutions and on Substrates [†]. *J. Phys. Chem. B* **2009**, *113* (12), 3750–3768. https://doi.org/10.1021/jp807671b.

(18) Birshtein, T. M.; Borisov, O. V.; Zhulina, Y. B.; Khokhlov, A. R.; Yurasova, T. A. Conformations of Comb-like Macromolecules. *Polym. Sci. USSR* **1987**, *29* (6), 1293–1300. https://doi.org/10.1016/0032-3950(87)90374-1.

(19) Fredrickson, G. H. Surfactant-Induced Lyotropic Behavior of Flexible Polymer Solutions. *Macromolecules* **1993**, *26* (11), 2825–2831. https://doi.org/10.1021/ma00063a029.

(20) Asgari, M. A Molecular Model for the Free Energy, Bending Elasticity, and Persistence Length of Wormlike Micelles. *Eur. Phys. J. E* **2015**, *38* (9). https://doi.org/10.1140/epje/i2015-15098-y.

(21) Cao, Y.; Smith, P. Liquid-Crystalline Solutions of Electrically Conducting Polyaniline. *Polymer* **1993**, *34* (15), 3139–3143. https://doi.org/10.1016/0032-3861(93)90381-J.

(22) Onsager, L. The Effects of Shape on the Interaction of Colloidal Particles. *Ann. N. Y. Acad. Sci.* **1949**, *51*, 627.

(23) Subbotin, A.; Saariaho, M.; Ikkala, O.; ten Brinke, G. Elasticity of Comb Copolymer Cylindrical Brushes. *Macromolecules* **2000**, *33* (9), 3447–3452. https://doi.org/10.1021/ma991031l.

(24) Nakamura, Y.; Norisuye, T. Backbone Stiffness of Comb-Branched Polymers. *Polym. J.* **2001**, *33* (11), 874–878. https://doi.org/10.1295/polymj.33.874.

(25) Denesyuk, N. A. Conformational Properties of Bottle-Brush Polymers. *Phys. Rev. E* **2003**, *67* (5). https://doi.org/10.1103/PhysRevE.67.051803.

(26) Terao, K.; Nakamura, Y.; Norisuye, T. Solution Properties of Polymacromonomers Consisting of Polystyrene. 2. Chain Dimensions and Stiffness in Cyclohexane and Toluene. *Macromolecules* **1999**, *32* (3), 711–716. https://doi.org/10.1021/ma9816517.

(27) Terao, K.; Hokajo, T.; Nakamura, Y.; Norisuye, T. Solution Properties of Polymacromonomers Consisting of Polystyrene. 3. Viscosity Behavior in Cyclohexane and Toluene. *Macromolecules* **1999**, *32* (11), 3690–3694. https://doi.org/10.1021/ma990091o.

(28) Hokajo, T.; Terao, K.; Nakamura, Y.; Norisuye, T. Solution Properties of Polymacromonomers Consisting of Polystyrene V. Effect of Side Chain Length on Chain Stiffness. *Polym. J.* **2001**, *33* (6), 481–485.

(29) Sugiyama, M.; Nakamura, Y.; Norisuye, T. Dilute-Solution Properties of Polystyrene Polymacromonomer Having Side Chains of over 100 Monomeric Units. *Polym. J.* **2008**, *40* (2), 109–115. https://doi.org/10.1295/polymj.PJ2007157.

(30) Terao, K.; Takeo, Y.; Tazaki, M.; Nakamura, Y.; Norisuye, T. Polymacromonomer Consisting of Polystyrene. Light Scattering Characterization in Cyclohexane. *Polym. J.* **1999**, *31* (2), 193–198.

(31) Zhang, B.; Gröhn, F.; Pedersen, J. S.; Fischer, K.; Schmidt, M. Conformation of Cylindrical Brushes in Solution: Effect of Side Chain Length. *Macromolecules* **2006**, *39* (24), 8440–8450. https://doi.org/10.1021/ma0613178.

(32) Gerle, M.; Fischer, K.; Roos, S.; Müller, A. H. E.; Schmidt, M.; Sheiko, S. S.; Prokhorova, S.; Möller, M. Main Chain Conformation and Anomalous Elution Behavior of Cylindrical Brushes As Revealed by GPC/MALLS, Light Scattering, and SFM [‡]. *Macromolecules* **1999**, *32* (8), 2629–2637. https://doi.org/10.1021/ma9816463.

(33) Hsu, H.-P.; Paul, W.; Binder, K. Standard Definitions of Persistence Length Do Not Describe the Local "Intrinsic" Stiffness of Real Polymer Chains. *Macromolecules* **2010**, *43* (6), 3094–3102. https://doi.org/10.1021/ma902715e.

(34) Hsu, H.-P.; Paul, W.; Rathgeber, S.; Binder, K. Characteristic Length Scales and Radial Monomer Density Profiles of Molecular Bottle-Brushes: Simulation and Experiment. *Macromolecules* **2010**, *43* (3), 1592–1601. https://doi.org/10.1021/ma902101n.

(35) Hsu, H.-P.; Paul, W.; Binder, K. Understanding the Multiple Length Scales Describing the Structure of Bottle-Brush Polymers by Monte Carlo Simulation Methods. *Macromol. Theory Simul.* **2011**, *20* (7), 510–525. https://doi.org/10.1002/mats.201000092.

(36) Feuz, L.; Leermakers, F. A. M.; Textor, M.; Borisov, O. Bending Rigidity and Induced Persistence Length of Molecular Bottle Brushes: A Self-Consistent-Field Theory. *Macromolecules* **2005**, *38* (21), 8891–8901. https://doi.org/10.1021/ma050871z.

(37) Saariaho, M.; Szleifer, I.; Ikkala, O.; ten Brinke, G. Extended Conformations of Isolated Molecular Bottle-Brushes: Influence of Side-Chain Topology. *Macromol. Theory Simul.* **1998**, *7* (2), 211–216. https://doi.org/10.1002/(SICI)1521-3919(19980301)7:2<211::AID-MATS211>3.0.CO;2-A.

(38) Gauger, A.; Pakula, T. Static Properties of Noninteracting Comb Polymers in Dense and Dilute Media. A Monte Carlo Study. *Macromolecules* **1995**, *28* (1), 190–196. https://doi.org/10.1021/ma00105a025.

(39) Rathgeber, S.; Pakula, T.; Wilk, A.; Matyjaszewski, K.; Beers, K. L. On the Shape of Bottle-Brush Macromolecules: Systematic Variation of Architectural Parameters. *J. Chem. Phys.* **2005**, *122* (12), 124904. https://doi.org/10.1063/1.1860531.

(40) Rathgeber, S.; Pakula, T.; Wilk, A.; Matyjaszewski, K.; Lee, H.; Beers, K. L. Bottle-Brush Macromolecules in Solution: Comparison between Results Obtained from Scattering Experiments and Computer Simulations. *Polymer* **2006**, *47* (20), 7318–7327. https://doi.org/10.1016/j.polymer.2006.06.010.

(41) Wataoka, I.; Urakawa, H.; Kajiwara, K.; Schmidt, M.; Wintermantel, M. Structural Characterization of Polymacromonomer in Solution by Small-Angle x-Ray Scattering. *Polym. Int.* **1997**, *44* (3), 365–370. https://doi.org/10.1002/(SICI)1097-0126(199711)44:3<365::AID-PI871>3.0.CO;2-X.

(42) Pesek, S. L.; Li, X.; Hammouda, B.; Hong, K.; Verduzco, R. Small-Angle Neutron Scattering Analysis of Bottlebrush Polymers Prepared via Grafting-Through Polymerization. *Macromolecules* **2013**, *46* (17), 6998–7005. https://doi.org/10.1021/ma401246b.

(43) Pedersen, J. S.; Schurtenberger, P. Scattering Functions of Semiflexible Polymers with and without Excluded Volume Effects. *Macromolecules* **1996**, *29* (23), 7602–7612. https://doi.org/10.1021/ma9607630.

(44) Hsu, H.-P.; Paul, W.; Binder, K. Estimation of Persistence Lengths of Semiflexible Polymers: Insight from Simulations. **2013**, 18.

(45) Hsu, H.-P.; Paul, W.; Binder, K. Polymer Chain Stiffness vs. Excluded Volume: A Monte Carlo Study of the Crossover towards the Worm-like Chain Model. *EPL Europhys. Lett.* **2010**, *92* (2), 28003. https://doi.org/10.1209/0295-5075/92/28003.

(46) Dutta, S.; Wade, M. A.; Walsh, D. J.; Guironnet, D.; Rogers, S. A.; Sing, C. E. Dilute Solution Structure of Bottlebrush Polymers. *Soft Matter* **2019**. https://doi.org/10.1039/C9SM00033J.

(47) Borisov, O. V.; Birshtein, T. M.; Zhulina, Y. B. The Temperature-Concentration Diagram of State for Solutions of Comb-like Macromolecules. *Polym. Sci. USSR* **1987**, *29* (7), 1552–1559. https://doi.org/10.1016/0032-3950(87)90416-3.

(48) Paturej, J.; Kreer, T. Hierarchical Excluded Volume Screening in Solutions of Bottlebrush Polymers. *Soft Matter* **2017**, *13* (45), 8534–8541. https://doi.org/10.1039/C7SM01968H.

(49) Bolisetty, S.; Airaud, C.; Xu, Y.; Müller, A. H. E.; Harnau, L.; Rosenfeldt, S.; Lindner, P.; Ballauff, M. Softening of the Stiffness of Bottle-Brush Polymers by Mutual Interaction. *Phys. Rev. E* **2007**, *75* (4). https://doi.org/10.1103/PhysRevE.75.040803.

(50) Bolisetty, S.; Rosenfeldt, S.; Rochette, C. N.; Harnau, L.; Lindner, P.; Xu, Y.; Müller, A. H. E.; Ballauff, M. Interaction of Cylindrical Polymer Brushes in Dilute and Semi-Dilute Solution. *Colloid Polym. Sci.* **2009**, *287* (2), 129–138. https://doi.org/10.1007/s00396-008-1962-3.

(51) Paturej, J.; Sheiko, S. S.; Panyukov, S.; Rubinstein, M. Molecular Structure of Bottlebrush Polymers in Melts. *Sci. Adv.* **2016**, *2* (11), e1601478. https://doi.org/10.1126/sciadv.1601478.

(52) Bates, F. S.; Fredrickson, G. H. Block Copolymers—Designer Soft Materials. *Phys. Today* **1999**, *52* (2), 32–38. https://doi.org/10.1063/1.882522.

(53) He, W.-N.; Xu, J.-T. Crystallization Assisted Self-Assembly of Semicrystalline Block Copolymers. *Prog. Polym. Sci.* **2012**, *37* (10), 1350–1400. https://doi.org/10.1016/j.progpolymsci.2012.05.002.

(54) Kawamoto, K.; Zhong, M.; Gadelrab, K. R.; Cheng, L.-C.; Ross, C. A.; Alexander-Katz, A.; Johnson, J. A. Graft-through Synthesis and Assembly of Janus Bottlebrush Polymers from A- *Branch* -B Diblock Macromonomers. *J. Am. Chem. Soc.* **2016**, *138* (36), 11501–11504. https://doi.org/10.1021/jacs.6b07670.

(55) Gai, Y.; Song, D.-P.; Yavitt, B. M.; Watkins, J. J. Polystyrene- *Block* -Poly(Ethylene Oxide) Bottlebrush Block Copolymer Morphology Transitions: Influence of Side Chain Length and Volume Fraction. *Macromolecules* **2017**, *50* (4), 1503–1511. https://doi.org/10.1021/acs.macromol.6b01415.

(56) Bolton, J.; Bailey, T. S.; Rzayev, J. Large Pore Size Nanoporous Materials from the Self-Assembly of Asymmetric Bottlebrush Block Copolymers. *Nano Lett.* **2011**, *11* (3), 998–1001. https://doi.org/10.1021/nl103747m.

(57) Wintermantel, M.; Fischer, K.; Gerle, M.; Ries, R.; Schmidt, M.; Kajiwara, K.; Urakawa, H.; Wataoka, I. Lyotropic Phases Formed by"Molecular Bottlebrushes." *Angew. Chem. Int. Ed. Engl.* **1995**, *34* (1314), 1472–1474. https://doi.org/10.1002/anie.199514721.

(58) Tsukahara, Y.; Miyata, M.; Senoo, K.; Yoshimoto, N.; Kaeriyama, K. Mesomorphic Phase Formation of Poly (Macromonomer)s of Polystyrene Macromonomers. *Polym. Adv. Technol.* **2000**, *11* (5), 210–218. https://doi.org/10.1002/1099-1581(200005)11:5<210::AID-PAT957>3.0.CO;2-7.

(59) Nakamura, Y.; Koori, M.; Li, Y.; Norisuye, T. Lyotropic Liquid Crystal Formation of Polystyrene Polymacromonomers in Dichloromethane. *Polymer* **2008**, *49* (22), 4877–4881. https://doi.org/10.1016/j.polymer.2008.08.049.

(60) Pirogovsky, P. Intramolecular Conflict: Conformation and Self-Assembly of Architecturally Complex Macromolecules in Solution, California Institute of Technology, 2013.

(61) Higgins, J. S.; Henry, B. C. *Polymers and Neutron Scattering*; Clarendon Press Oxford., 1994.

(62) Rubinstein, M.; Colby, R. H. *Polymer Physics*; Oxford University Press, 2003.

(63)   Dobrynin, A.; Rubinstein, M. Theory of Polyelectrolytes in Solutions and at Surfaces. *Prog. Polym. Sci.* **2005**, *30* (11), 1049–1118. https://doi.org/10.1016/j.progpolymsci.2005.07.006.

(64)   Dozier, W. D.; Huang, J. S.; Fetters, L. J. Colloidal Nature of Star Polymer Dilute and Semidilute Solutions. *Macromolecules* **1991**, *24* (10), 2810–2814. https://doi.org/10.1021/ma00010a026.

(65)   Terao, K.; Hokajo, T.; Nakamura, Y.; Norisuye, T. Solution Properties of Polymacromonomers Consisting of Polystyrene. 3. Viscosity Behavior in Cyclohexane and Toluene. *Macromolecules* **1999**, *32* (11), 3690–3694. https://doi.org/10.1021/ma990091o.

(66)   Rangarajan, P.; Register, R. A.; Fetters, L. J.; Bras, W.; Naylor, S.; Ryan, A. J. Crystallization of a Weakly Segregated Polyolefin Diblock Copolymer. *Macromolecules* **1995**, *28* (14), 4932–4938. https://doi.org/10.1021/ma00118a022.

(67)   Rangarajan, P.; Register, R. A.; Adamson, D. H.; Fetters, L. J.; Bras, W.; Naylor, S.; Ryan, A. J. Dynamics of Structure Formation in Crystallizable Block Copolymers. *Macromolecules* **1995**, *28* (5), 1422–1428. https://doi.org/10.1021/ma00109a013.

(68)   Zhu, L.; Chen, Y.; Zhang, A.; Calhoun, B. H.; Chun, M.; Quirk, R. P.; Cheng, S. Z. D.; Hsiao, B. S.; Yeh, F.; Hashimoto, T. Phase Structures and Morphologies Determined by Competitions among Self-Organization, Crystallization, and Vitrification in a Disordered Poly(Ethylene Oxide)- *b* -Polystyrene Diblock Copolymer. *Phys. Rev. B* **1999**, *60* (14), 10022–10031. https://doi.org/10.1103/PhysRevB.60.10022.

(69)   Douzinas, K. C.; Cohen, R. E. Chain Folding in EBEE Semicrystalline Diblock Copolymers. **1992**, *25* (19), 6.

(70)   Ryan, A. J.; Hamley, I. W.; Bras, W.; Bates, F. S. Structure Development in Semicrystalline Diblock Copolymers Crystallizing from the Ordered Melt. *Macromolecules* **1995**, *28* (11), 3860–3868. https://doi.org/10.1021/ma00115a016.

(71)   Hamley, I. W.; Fairclough, J. P. A.; Terrill, N. J.; Ryan, A. J.; Lipic, P. M.; Bates, F. S.; Towns-Andrews, E. Crystallization in Oriented Semicrystalline Diblock Copolymers. *Macromolecules* **1996**, *29* (27), 8835–8843. https://doi.org/10.1021/ma960343a.

(72)   Mai, S.-M.; Fairclough, J. P. A.; Viras, K.; Gorry, P. A.; Hamley, I. W.; Ryan, A. J.; Booth, C. Chain Folding in Semicrystalline Oxyethylene/Oxybutylene Diblock Copolymers. *Macromolecules* **1997**, *30* (26), 8392–8400. https://doi.org/10.1021/ma971158f.

(73)   Zhu, L.; Cheng, S. Z. D.; Calhoun, B. H.; Ge, Q.; Quirk, R. P.; Thomas, E. L.; Hsiao, B. S.; Yeh, F.; Lotz, B. Crystallization Temperature-Dependent Crystal Orientations within Nanoscale Confined Lamellae of a Self-Assembled Crystalline−Amorphous Diblock Copolymer. *J. Am. Chem. Soc.* **2000**, *122* (25), 5957–5967. https://doi.org/10.1021/ja000275e.

(74)   Loo, Y.-L.; Register, R. A.; Adamson, D. H. Polyethylene Crystal Orientation Induced by Block Copolymer Cylinders. *Macromolecules* **2000**, *33* (22), 8361–8366. https://doi.org/10.1021/ma000962q.

(75)   Hong, S.; Yang, L.; MacKnight, W. J.; Gido, S. P. Morphology of a Crystalline/Amorphous Diblock Copolymer: Poly((Ethylene Oxide)- *b* -Butadiene). *Macromolecules* **2001**, *34* (20), 7009–7016. https://doi.org/10.1021/ma0100596.

(76)   Loo, Y.-L.; Register, R. A.; Ryan, A. J.; Dee, G. T. Polymer Crystallization Confined in One, Two, or Three Dimensions. *Macromolecules* **2001**, *34* (26), 8968–8977. https://doi.org/10.1021/ma011521p.

(77)   Shiomi, T.; Takeshita, H.; Kawaguchi, H.; Nagai, M.; Takenaka, K.; Miya, M. Crystallization and Structure Formation of Block Copolymers Containing a Rubbery

Amorphous Component. *Macromolecules* **2002**, *35* (21), 8056–8065. https://doi.org/10.1021/ma0200118.

(78) Loo, Y.-L.; Register, R. A.; Ryan, A. J. Modes of Crystallization in Block Copolymer Microdomains: Breakout, Templated, and Confined. *Macromolecules* **2002**, *35* (6), 2365–2374. https://doi.org/10.1021/ma011824j.

(79) Nojima, S.; Akutsu, Y.; Washino, A.; Tanimoto, S. Morphology of Melt-Quenched Poly(ε-Caprolactone)-Block-Polyethylene Copolymers. *Polymer* **2004**, *45* (21), 7317–7324. https://doi.org/10.1016/j.polymer.2004.08.044.

(80) Wang, Z.; Wang, X.; Ji, Y.; Qiang, X.; He, L.; Li, S. Bottlebrush Block Polymers in Solutions: Self-Assembled Microstructures and Interactions with Lipid Membranes. *Polymer* **2018**, *140*, 304–314. https://doi.org/10.1016/j.polymer.2018.02.053.

(81) Zhang, H.; Zhang, Z.; Gnanou, Y.; Hadjichristidis, N. Well-Defined Polyethylene-Based Random, Block, and Bilayered Molecular Cobrushes. *Macromolecules* **2015**, *48* (11), 3556–3562. https://doi.org/10.1021/acs.macromol.5b00713.

(82) Birshtein, T. .; Zhulina, E. .; Borisov, O. . Temperature-Concentration Diagram for a Solution of Star-Branched Macromolecules. *Polymer* **1986**, *27* (7), 1078–1086. https://doi.org/10.1016/0032-3861(86)90076-5.